On the feasibility of MEMS Micro-mirrors for Adaptive Alignment in Free-Space Optical Interconnects

James D. B. Prentice

Photonic Systems Group
Department of Electrical and Computer Engineering
McGill University
Montreal, QC, Canada
November 2003

A thesis submitted to the Faculty of Graduate Studies and Research in partial fulfillment of the requirements of the degree of Master of Engineering

Your file Votre référence
ISBN: 0-612-98558-X
Our file Notre référence
ISBN: 0-612-98558-X

ABSTRACT

This thesis is an investigation in the feasibility of the use of MEMS micro-mirror devices for adaptive alignment applications in free-space optical interconnects. In this scheme, dynamic beam steering is used as the mechanism to improve minimum system tolerances. Based on the parameters of a previously implemented interconnect, an optimized integrated design is presented. Two sets of micro-mirror designs were prototyped using the MUMPs foundry service. Numerical modeling of the integrated system indicated significant improvement in lateral and angular tilt misalignment tolerances using the MEMS beam steering system. The effect of mirror surface curvature on the integrated system was also investigated, indicating a high dependency of system performance on micro-mirror surface sag. Testing and characterization of the mirror prototypes indicated significant deviation from theoretical predictions. Nevertheless, future work in optimizing mirror designs will allow for improved performance.

SOMMAIRE

Cette thèse est une recherche sur l'utilisation des micro-miroirs de MEMS pour l'alignement adaptatives dans l'interconnexion optiques en espace libre. Dans ce système, la direction dynamique du faisceau est employée comme le mécanisme pour améliorer les tolérances minimum. Basée sur les paramètres d'une système d'interconnexion précédemment mise en application, une nouvelle conception intégrée et optimisée est présentée. Deux types de micro-miroirs ont été fabriqué en utilisant le service de fonderie MUMPs. Un model numérique du système intégré a indiqué un amélioration significative des tolérances latérales et angulaires d'alignement lors de l'utilisation des micro-miroirs. L'effet de la courbure de la surface du miroir sur le système intégré a été également étudié, indiquant une dépendance du functionnement sur le fléchissement de la surface du micro-miroir. L'examination et la caractérisation des prototypes des micro-miroirs ont indiqué une déviation significative des prédiction théoriques. Néanmoins, les futurs recherches dans l'optimisation des miroirs permettront des améliorations du functionment du system d'interconnexion.

ACKNOWLEDGEMENTS

This work would not have been possible without the support and encouragement of many people.

First and foremost, I would especially like to thank my supervisor, Dr. Andrew Kirk, for his incessant patience, advice, and guidance throughout the course of my degree.

Additionally, many thanks goes out to the many members of the McGill University Photonic Systems Group, both past and present, who have helped me with this work. In particular these include: Xuyen Hoa for his work in the design and testing of the micro-mirrors and help with the French translation of the abstract; Marc Châteauneuf for his expertise with the Demo 1.5 FSOI; Michaël Ménard and Frédéric Thomas-Dupuis for their help with the Code V software package; Cibby Pulikkaseril for his proficiency with *Matlab*; Ali Soleymani for his outstanding geometry skills; Colin Alleyne for his optics expertise, Marc Simard, Jean-Phillipe Thibodeau, Roberto Rotili, and Julien Faucher and many others, too many to name, for their endless support and moral encouragement.

Finally, I would like to thank my family, my mother, Catherine Prentice, father, David Prentice, brothers, Blair and Robert Prentice, and my girlfriend, Terri Preston, for their patience, encouragement, and unwavering support.

Financial aid for this work was provided by the Canadian Microelectronics Corporation (CMC), the Canadian Institute for Telecommunications Research (CITR) and the Canadian Institute for Photonic Innovations (CIPI).

TABLE OF CONTENTS

LIST OF FIGURES

LIST OF TABLES

1.0 Introduction

The following section describes the motivation and goal of this research, and finishes with an overview of the contents of this thesis.

1.1 Motivation

In recent years, considerable work has been documented on approaches to alleviating the bottleneck present in short-distance communications in distributed digital systems. In classical digital system design, electrical interconnects provided the necessary chip-to-chip and board-to-board connections. However, the low data-rates inherent in standard electrical interconnections have led researchers to pursue alternative avenues to facilitate these connections. Recent advances in the area of CMOS optoelectronic device integration, the ability to densely integrate light emitters and detectors and operate these devices at high data-rates, has brought the idea of bi-directional parallel optical communication to the forefront. In the past 15 years, a number of POI designs have been implemented, for the most part targeting applications with the following characteristics:

1) Communication distances ranging from 4cm to 1.35m
2) Channel counts varying from 16 to 512 channels
3) Channel densities in upwards of 1250 channels/cm^2
4) Data rates up to 1Gbps/channel. [1]

Research has focused on two principle approaches - waveguide and free-space optics based systems.

Waveguide-based interconnects typically consist of both one and two-dimensional arrays of optical fibers. Two classifications have been documented – ordered fiber arrays (OFAs) and fiber image guides (FIGs).

OFAs employ moderately sized arrays of glass or polymer optical fibers, in which each fiber serves as a single optical channel. Also known as fiber ribbon cables, both one and two-dimensional configurations have been investigated. One-dimensional fiber ribbon-based optical interconnects are commercially available, however, they do not scale well with large numbers of channels. Two-dimensional OFAs with arrays of 8x8 and greater fibers have been documented [2], but they suffer from reliability issues.

FIGs consist of similar tightly packed two-dimensional arrays of polymer or glass optical fibers, however the light from each source is not confined to a single fiber in the array. As each channel propagates over several fibers, this implementation does not suffer from channel losses due to fiber loss inherent in OFAs. Several implementations have been documented with data rates in upwards of 1Gbps over 30 or more channels [3], [4].

Although OFAs and FIGs offer a flexible alternative for the higher end of the communications range outlined in the above list (1-1.5m), both techniques suffer from high levels of attenuation inherent in optical fibers, device coupling losses, cost, and channel limitations. Work continues on providing solutions to these challenging problems.

The alternative approach, and the focus of this thesis, employs free-space optical components as the interconnection medium between large arrays of photonic devices. Known as two-dimensional free-space optical interconnects (2D-FSOIs), they offer a more scalable approach to achieving high data-rate, large bandwidth, low-power, and low-noise connections between chips or boards in systems with multiple packaging layers [1]. As illustrated in Figure 1 below, this includes connections between integrated circuits on a board [Figure 1(a)], boards in a backplane [Figure 1(b)], and boards in a rack configuration [Figure 1(c)].

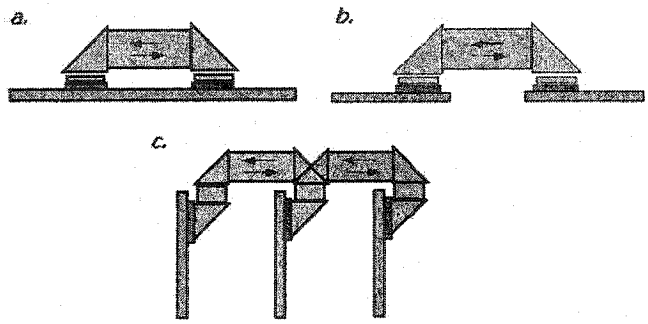

Figure 1 - Applications of Free-Space Optical Interconnects
a. Chip to Chip on a Board, b. Board to Board in a Backplane, c. Board to Board in a Rack

Integrated two-dimensional arrays of optoelectronic-VLSI based devices, such as GaAs-based vertical-cavity surface-emitting lasers (VCSELs) and photodetectors (PDs), imaged by the appropriate optics, including both bulk macro and micro-optical components, and assembled using customized optomechanical packaging, facilitate the parallel interconnection [1]. Driven by this technology, these optical links focus on interconnection distances on the order of centimeters, and data rates ranging from hundreds of megahertz to 1Gbps/channel, representative of typical distances and bus speeds in commercially available distributed digital systems [1], [5].

The design and implementation of free-space optical interconnects faces several issues, the most important of which are system flexibility and cost. Both are interrelated. As one would expect, a flexible system typically demands a large number of optical components. Correspondingly, the cost of the system increases.

The basis for both of these factors can traced to the challenge of maintaining end-to-end alignment in interconnects. Poor source-receiver alignment significantly degrades system performance and therefore flexibility. Free-space optical interconnects have been shown to operate within minimum tolerances, however, expensive precision manufacturing and costly mechanical alignment techniques are required to minimize component misalignment during the system assembly and packaging processes.

Consequently, in order to maximize flexibility and minimize the cost, the end-to-end alignment must remain optimized. However, operating conditions constantly fluctuate,

and therefore, for optimal alignment, both static and adaptive, or real-time alignment must be available. Various schemes for misalignment detection and correction in free-space optical interconnects have been investigated [5]-[10]. This thesis focuses on a potential solution to this challenging problem.

1.2 Objective

This thesis is a study in the feasibility of applying microelectromechanical systems (MEMS) technology for adaptive misalignment correction in free-space optical interconnects. Specifically, it describes the integration of MEMS micro-mirror arrays into a previously developed two-dimensional free-space optical link, and evaluates the performance of the micro-mirrors as real-time beam steering components.

To this end, the objectives of this thesis are two-fold. First, based on extensive prior MEMS research, design, characterize, and test appropriate MEMS micro-mirror designs for integration with the existing test platform. Second, using CAD and software tools, numerically model the performance of the integrated system, thereby evaluating the improvement in misalignment tolerances offered by the use of the MEMS micro-mirrors.

These establishment of these objectives ensured that all avenues were considered in examining the practicability of this project.

1.3 Overview

The structure of this document follows a similar structure to the aforementioned objectives. Chapter 2 examines the basics of free-space optical interconnects, specifically the test platform under investigation, documents techniques for achieving alignment in FSOIs, and provides relevant background information pertaining to MEMS micro-mirror technology. Chapter 3 describes the modified interconnect design, detailing the incorporation of MEMS micro-mirror arrays into existing free-space optical link. Chapter 4 details the numerical modeling of the integrated system, investigating various

performance and misalignment criterion. Chapter 5 describes the test and characterization of the MEMS micro-mirror prototypes. Lastly, chapter 6 concludes this document with an evaluation of the feasibility of the use of MEMS micro-mirrors for real-time beam steering applications in free-space optical interconnects.

2.0 Background

This chapter serves as an introduction to the topic of misalignment correction and detection in free-space optical interconnects. First, a brief introduction to free-space optical interconnects is given, highlighting the basic FSOI topologies. This is followed by a detailed explanation of the test platform under investigation. Subsequently, the necessary background information on relevant work done in the areas of misalignment correction and detection in FSOIs is presented. Lastly, this chapter concludes with a discussion on MEMS micro-mirror technology.

2.1 Two-dimensional FSOIs – Basic Designs

As outlined in chapter 1, free-space optical interconnects, for the most part, adhere to a generic system topology - densely packed two-dimensional arrays of optoelectronic-VLSI emitters and detectors in CMOS technology imaged by appropriate optics and assembled using custom optomechanic packaging. It is in the design of the interconnect optics, also known as the relay optics, where the major differences in implementations arise. The three major optical relay schemes include macrooptical, microoptical, and clustered or hybrid-lens optical systems [1].

Macrooptical systems are based on conventional macrooptical elements, otherwise known as off-the-shelf components. Consequently, a number of different macrooptical relay optics designs have been used to facilitate the required emitter-to-detector interconnection. The simplest examples is 4-f telecentric optical relay made of a single pair of telecentric lenses [1] [Figure 2(a)], and an optical relay based on a double Petzval lens design [11], shown in Figure 2(b). Both of these designs employ a single aperture to image the entire system.

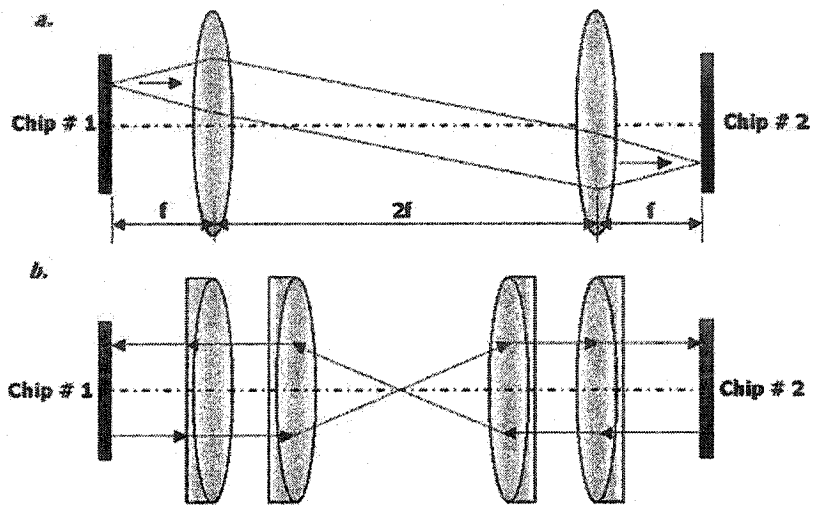

Figure 2 - Macrooptical Systems
a. 4-f Telecentric Optical Relay, b. Double Petzval lens design

Advantages of such designs include long optical throw, and design, construction, and analysis simplicity, inherent in the use of readily available bulk optical components [1], [5], [12]. Nevertheless, macrooptical designs have several important disadvantages. They require lenses with low aberrations, exhibit a lack of scalability in terms of field-of-view, and do not represent practical implementations due to the bulky nature of the macrolens components [1], [13].

Microoptics-based optical relays present a potential solution to the drawbacks of macrooptical designs. As shown in Figure 3, in this implementation, each optical channel is serviced by a pair of microlenses, and is referred to as a microchannel.

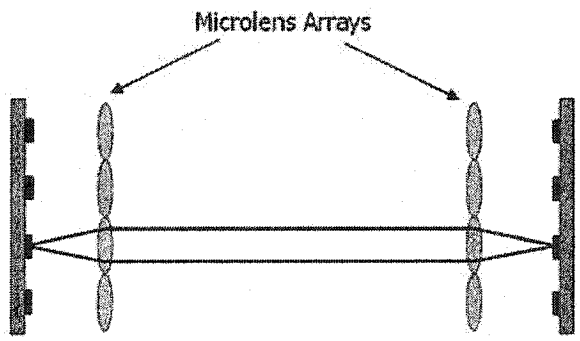

Figure 3 - Microoptics-based Relay

Improved scalability is achieved simply by increasing the number of microchannels, overall interconnect size is decreased as the system is inherently compact, and the strict lens characteristics observed in macrolens systems are slightly loosened. However, such a system is diffraction limited, thereby significantly reducing the maximum achievable optical throw (<10mm), and owing to its small channel spacing, is highly intolerant to component misalignment. Several such systems have been documented [1], [14].

The third major FSOI design employs a clustered or hybrid-lens optical relay scheme. In this system, the transmitter and receiver image planes are divided into clusters of elements, and telecentric pairs of minilens arrays are used to image between them [5]. This system combines the majority of the strengths of the previously described systems, with few of the weaknesses. Similar to macrooptic systems it allows for a long optical throw and reasonable tolerance to component misalignment, and additionally, it provides the scalability offered by microoptic systems [1].

The FSOI under investigation in this thesis employed the latter approach, and is described in-depth in the following section.

2.1.1 Test-Platform - Demo 1.5 System

The test-platform for this project is a 512-channel bi-directional vertical-cavity surface-emitting laser based free-space optical link developed by the McGill Photonic Systems Group (PSG) in 2000 [5]. Operating at a wavelength of 850nm, it interconnects two printed-circuit boards (PCBs) with a center-to-center separation of 83mm. The system was developed as a precursor to a rack-based system, as the specified 83mm optical throw is equivalent to a 1-inch board-to-board separation in a bookshelf configuration [Figure 1(c)]. Figure 4 shows a schematic of the free-space optical link.

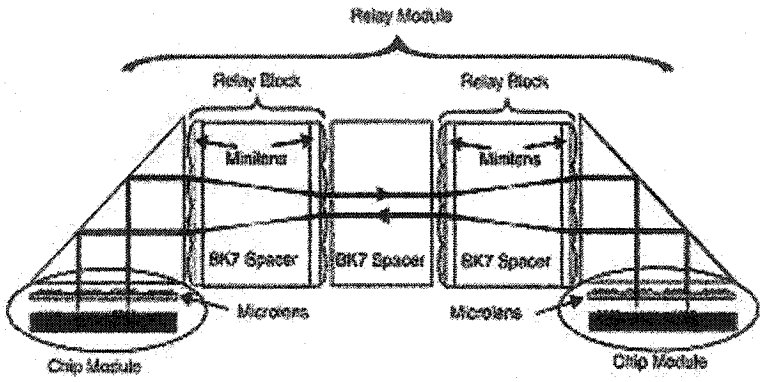

Figure 4 - Schematic of Test-platform

The following sections describe the key components of the FSOI including the VLSI-chip, the relay optics, as well as the system performance and tolerances to misalignment. Despite the improvement in misalignment tolerances exhibited by the hybrid-lens-based design, it will become evident that component misalignment remains a critical performance issue for two-dimensional FSOIs.

2.1.1.1 VLSI Optoelectronic (OE) Chip – Clustered System

The VLSI-OE chip consisted of 256 VCSELs and 256 photodiodes created using hybrid Si-GaAs technology. As the system topology employed a clustered design, the OE chip was sectioned into 4x8 clusters of 4x4 active devices. Figure 5 is a photograph of the layout of the VLSI-OE chip.

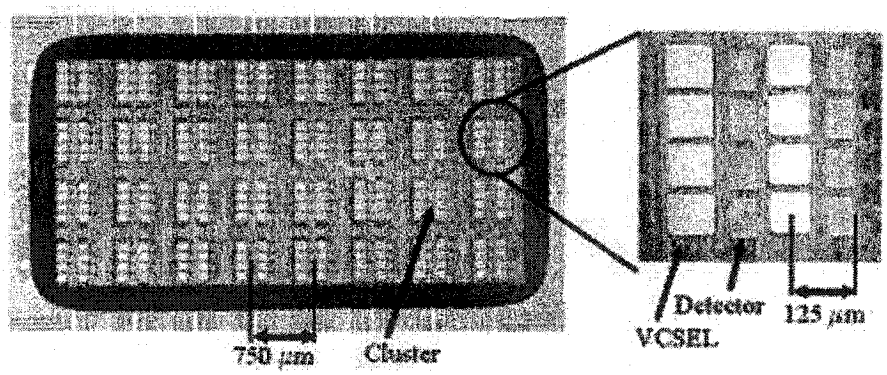

Figure 5 - Photograph of Layout of VLSI-OE chip

As shown in Figure 5, the OE devices were separated by a pitch of 125μm, resulting in a total cluster size of 375μm. Cluster-to-cluster spacing was specified as 750μm. These values were selected in such a way as to maximize the fraction of the GaAs die used. The

VCSELs used were multimode with a mode-field diameter of 6μm and a full-divergence angle of 20°, while the photodiodes were square with a side-length of 50μm.

2.1.1.2 Optical Relay Design

As shown in Figure 4, the relay optics was divided into two modules: 1) the chip module, and 2) the relay module.

The chip module consisted of the VLSI-OE chip integrated with arrays of refractive microlenses. The microlenses were designed to collimate the highly divergent beams emitted by the VCSELs. Correspondingly, a single microlens was assigned to image each individual device on the chip, resulting in a circular aperture of diameter equivalent to the device pitch on the chip. The focal length was determined by the divergence of the VCSEL beams. The resulting f/2 refractive microlenses had a circular diameter of 125μm and a focal length of 250μm in air. Similar to the devices on the VLSI chip, they were grouped in an array of 4x8 clusters of 4x4 microlenses. Figure 6 shows a photograph of the microlens array.

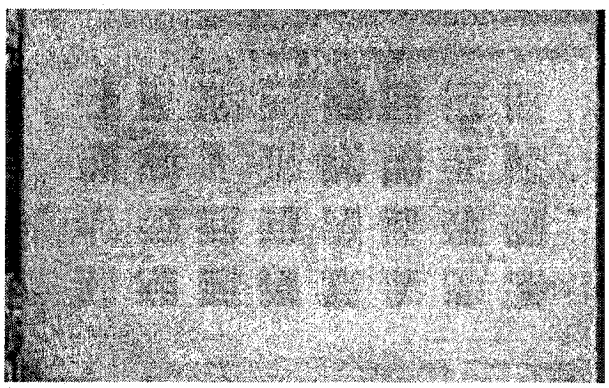

Figure 6 - Photograph of Collimating Microlens Array

With the aim of reducing spherical aberrations, the microlens arrays were fabricated on a 300μm thick fused-silica substrate, such that the convex side of the microlenses was facing away from the VCSELs. The VLSI chip was then positioned, using a six-degree of freedom micropositioning stage at a distance of 44μm from the microlens array. This allowed for proper beam collimation, as it placed the devices at exactly the focal plane of the microlenses.

As shown in Figure 4, the relay module consisted of two pairs of telecentric minilenses separated by BK7 glass spacers. Adhering to the clustered mini-channel configuration, each device cluster was imaged by a single minilens, resulting in an array of 4x8 750μm-square diffractive minilens, equivalent to the cluster pitch on the VLSI chip. Thus, 512 beams from the devices within a chip area of 5.625mm x 2.625mm were therefore propagated within a rectangular optical window with dimensions 6mm x 3mm, resulting in an interconnect channel density of 2844 channels/cm^2. Figure 7(a) shows a photograph of the diffractive minilens array.

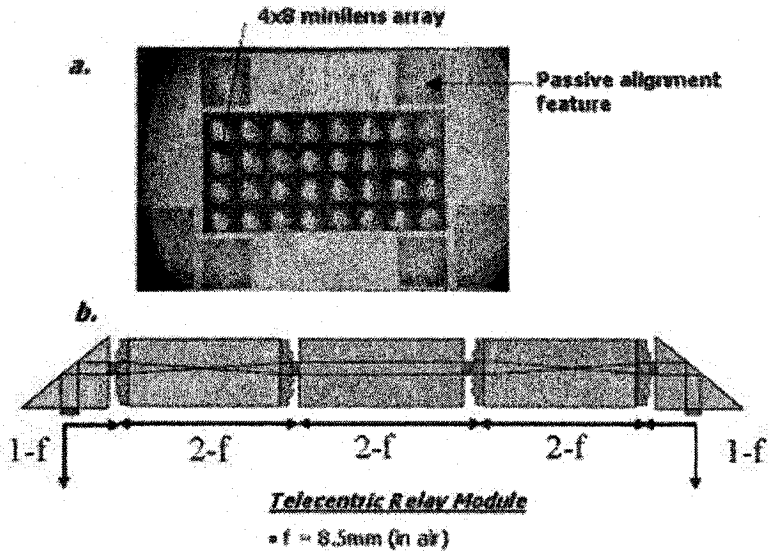

Figure 7 - Demo 1.5 Optical Relay
a. Photograph of Diffractive Minilens Array, b. Schematic of 8-f Telecentric Relay Module

The f/8 diffractive minilens arrays were fabricated with 256-level on a 1mm thick fused-silica substrate, to allow for uniform and high diffraction efficiency. In order to facilitate the insertion of alignment features, the substrate was diced to overall dimensions of 20mm x 6mm. Crosstalk in adjacent channels was minimized, thereby maximizing system throughput, by selecting the focal length of the minilenses to be 8.5mm in air. However, in order to achieve the total optical throw of 83mm, specified by the chip-to-chip separation, three polished BK7 glass spacers of length 23.59mm, each equivalent to a telecentric system of focal length 8.5mm in air, were inserted between two telecentric minilens arrays. As shown in Figure 7(b), the completed relay module, therefore, consisted of an 8-f telecentric system.

Referring to Figure 4 the final components of the optical design were the BK7 glass right-angle prisms inserted at either end of the relay module, allowing for communication between two in-plane PCBs. The prisms had a face length of 6mm and were positioned at a distance of 0.8mm from the relay module and 3.74mm from the microlenses, thereby giving a total optical path length from the minilens to microlens arrays of 8.5mm – the required distance for the telecentric configuration shown in Figure 7(b).

Figure 8 shows a schematic of the assembled system.

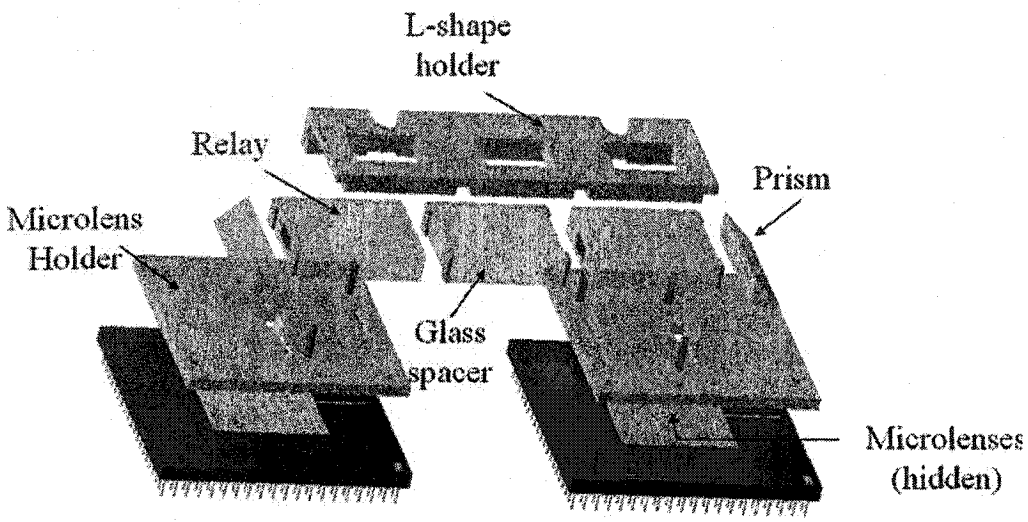

Figure 8 - Schematic of Assembled Demo 1.5 System

2.1.1.3 Misalignment Analysis

Given the high channel density and large number of optical components in the Demo 1.5 system, assessing component tolerances to misalignment was critical for determining the level of precision required to correctly assemble the link. Misalignment analysis for this system was performed by displacing components both individually and grouped in modules. The system throughput was then calculated using customized ray tracing simulations, neglecting such losses as Fresnel reflections, diffraction efficiencies, and absorption. It was estimated that these losses would reduce the system throughput to approximately 50% to 65%. Tolerances were determined by limiting worst-case system throughput to 95% of the maximum. Table 1(a) and (b) below summarize the relevant system tolerances for both individual and modular component misalignments.

Table 1 - Demo 1.5 Component Misalignment Tolerances
a. Individual Components, b. Modular misalignment

a.

Misaligned Components	>95% Tolerance
VCSEL (in x)	± 2.5 μm
Microlens (in x)	± 2.5 μm
VCSEL (in z)	± 15 μm
First VCSEL-microlens (in z)	± 2.0 mm
Relay (in x)	± 12.5 μm
Relay θx, θy	± 0.05 degrees

b.

Modular Misalignment	>95% Tolerance
VCSEL-microlens (in x)	± 25 μm
Two Relays (in x)	± 90 μm

As is shown in Table 1(b), misalignment tolerances were improved by grouping individual components into larger modules. By grouping the VCSEL and microlens arrays, the lateral misalignment tolerance was increased from ±2.5μm, shown in Table 1(a), to ±25μm. Similar effects were observed for the relay modules. In all cases of modularization, it was assumed that the individual components within the module were precision-aligned using specialized optomechanics.

2.1.1.4 System Performance

Following component assembly, the system performance was characterized using such metrics as the total system throughput, the optical efficiency of the link, the level of crosstalk between adjacent channels, and data transfer rate.

The overall system throughput was measured by activating all of the VCSELs on one chip, and measuring the resulting power after microlenses positioned at the opposite end of the link. The average throughput was found to be approximately 31%.

The optical link efficiency was determined by activating a single VCSEL and calculating the ratio between the power at the VCSEL and that incident on the corresponding detector, represented by a pinhole power meter. The ratio of average power measured was 34.3%. The total efficiency was then calculated as the product of this value with the average system throughput stated above. Total optical link efficiency was therefore found to be approximately 9%.

In both cases, the experimental values were considerably lower than the 50-65% predicted from misalignment simulations. Excessive losses were attributed to a 1-dB power leak at the prisms, beam clipping at the relays, as well as the possibility of longitudinal misalignment between the VLSI-OE chip and the microlens array

2.1.1.5 Analysis – Performance vs. Misalignment

The tight constraints imposed by the simulated misalignment tolerances meant that a high degree of precision was necessary during the assembly of the optical link.

Similar trends exist for the majority of other prior interconnect designs. Mechanical alignment techniques and fabrication processes have been documented to provide fine feature and component alignment to within several micrometers. However, this is a costly and tedious process as customized optomechanical components are required. It is for this reason that various precision alignment techniques for free-space optical interconnects have been investigated. The following section describes and evaluates several such approaches.

2.2 FSOIs – Misalignment Detection and Correction

In recent years, several techniques for detecting and correcting for misalignment have been investigated. These may be classified into three distinct categories: 1) Passive, 2) Active and 3) Adaptive or real-time alignment techniques.

For the most part, the first two cases employ a pre-assembly alignment philosophy. In other words, alignment is accomplished prior to permanently attaching the system components. Once assembled, components are fixed and the degree of alignment cannot be altered. Passive alignment approaches use external system features to measure the degree of misalignment. Conversely, active alignment techniques employ existing system components, such as sources and detectors, to actively determine the state of alignment. Typically, in both cases, customized optomechanic components are used to correct for misalignment.

An offspring of active alignment techniques, adaptive alignment involves the use of devices or features that evaluate the system alignment criterion in real-time and make the appropriate corrections. Ultimately, adaptive approaches strive to allow for systems to be assembled using rudimentary 'coarse' alignment methods. In doing so, post-assembly alignment is accomplished using the specialized system features or components.

The following sections describe the above approaches.

2.2.1 Passive & Active Alignment Techniques

Passive alignment approaches generally fall under two distinct categories: 1) Passive mechanical alignment, and 2) Passive alignment targets.

Passive mechanical alignment typically refers to the use of specialized configurations of customized optomechanic components to achieve optimal mechanical alignment. Kinematic packaging techniques are examples of this approach, in which components and specialized optomechanics are designed in such a way that only a single position or placement will allow for accurate component alignment. Components are therefore inserted manually, without the need for further readjustment. Ultimately, the level of alignment is pre-determined by the tolerances and design of optomechanics. One such implementation is documented in [15].

The second classification, passive alignment targets, employs additional optical features and external dedicated alignment sources to detect the degree of misalignment. Realignment is accomplished using mechanical translation stages. One such an example, documented in [16], proposed and demonstrated the use of an interferometric alignment technique for measuring the degree of transverse, longitudinal, and rotational misalignment in a microchannel-based free-space optical interconnect. In this approach, pairs of dedicated diffractive lenslets were used to create an *in situ* interferometer to measure misalignment between two lens arrays spaced at a moderate distance. Figure 9 shows a schematic of the interferometric setup.

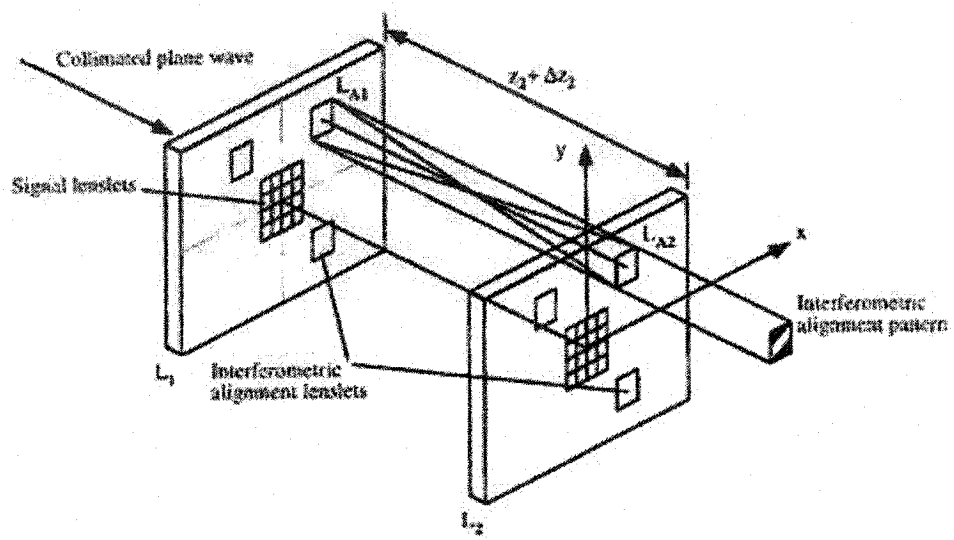

From: Robertson et al., *In situ* interferometric alignment systems for the assembly of microchannel relay systems. App. Opt. 36, 1997, pp. 9253-9260.

Figure 9 - *In situ* Interferometric Alignment Setup

As shown above, three pairs of low-efficiency diffractive lenses are positioned around the outside of the signal lens array. Collimated beams incident on the first alignment lens, diffract, based on the laws of diffraction, into *m* wavefronts, given by different diffraction orders of light. These wavefronts, propagating from lens array 1, are incident on the second diffractive alignment lens, creating an interference pattern characterized by a series of light and dark fringes. The fringes represent points of constructive and destructive interference between the interacting wavefronts. If either a lateral (in *x*-axis) or longitudinal (along the optical axis, *z*), or angular tilt misalignment is introduced, changes in the fringes patterns are observed. Variations in the number of fringes in the

interference pattern were shown to be directly related to the magnitude of longitudinal or lateral misalignment. In a similar fashion, changes in the periodicity of the fringe patterns were indicative of angular tilt misalignments of the lenslet arrays. Experimentally, accurate lateral (±1μm), longitudinal (±50μm), and rotational alignment were demonstrated.

Instead of using external alignment targets or optomechanic features, active alignment exploits existing components to actively determine the state of alignment. One simple example of this approach is aligning components until the system throughput is maximized. Used to align a laser source to an optical fiber, this method involves operating the source under normal conditions and measuring the resulting transmitted power in the fiber. In a similar fashion to passive alignment techniques, throughput is increased by mechanically realigning using customized optomechanics. Once the throughput is maximized, the system is assembled permanently.

Although both passive and active alignment techniques allow for accurate alignment in the completed system, the drawbacks are clear. As previously discussed, mechanical alignment techniques are tedious, time consuming, and require costly optomechanics. Secondly, once assembled, components are fixed, and the state of alignment post-assembly cannot be changed. As operating conditions constantly evolve, these techniques do not lend themselves well to commercial applications.

Adaptive alignment techniques, on the other hand, allow for real-time alignment correction, post-assembly, and therefore offer potential solutions to the shortcomings of passive and active alignment schemes in FSOIs.

2.2.2 Adaptive Alignment Techniques

Adaptive alignment techniques may be classified into three distinct categories: 1) Real-time alignment using Aperture Steering, 2) Adaptive Alignment via Spatial Redundancy, and 3) Real-time alignment via Beam Steering.

2.2.2.1 Aperture Steering

Real-time alignment via aperture steering uses either existing or external active components, such as sources and detectors, to measure and diagnose the *in situ* state of alignment of a system. Based on signals from these devices, the lateral position and angular tilt of the components in the *image* or receiver plane is changed in such a way that misalignment is minimized.

On such an example, documented by Boisset et al. in [9], employed specialized detectors to generate analog electrical signals proportional to the degree of lateral misalignment in a two-stage optical backplane interconnect. Figure 10(a) shows a schematic of the experimental setup.

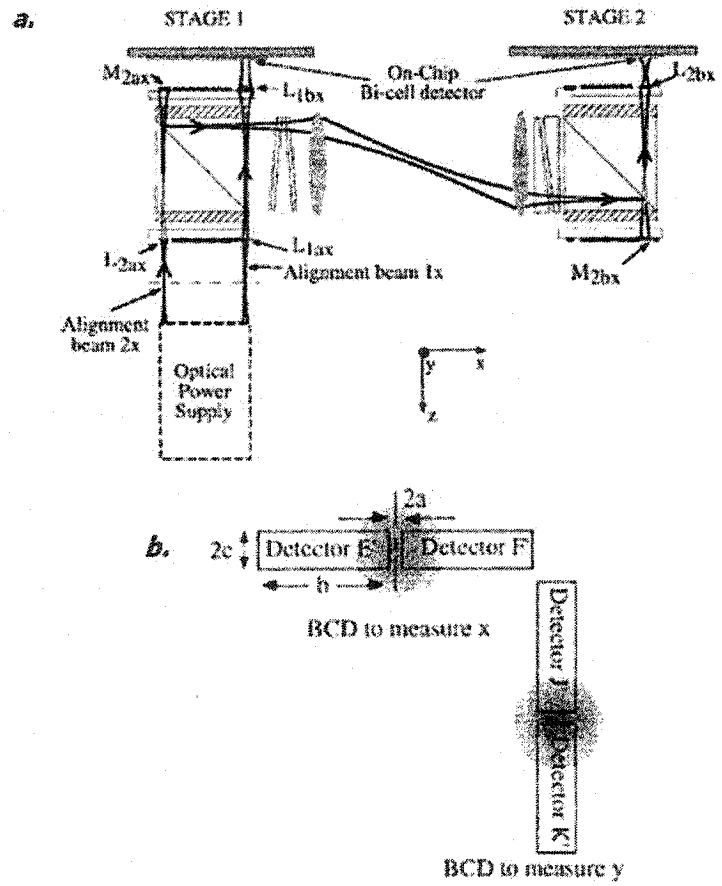

From: Boisset et al., *In situ* measurement of misalignment errors in free-space optical interconnects. Journ. Light. Tech. 16, 1998, pp. 847-858.

Figure 10 – *In situ* Misalignment Measurement System
a. Schematic of Two-Stage Optical Backplane Interconnect, b. Schematic of Bicell Detectors (BCDs)

As shown above, two sets of alignment beams were used to measure the degree of lateral misalignment in both the x and y axes for the two stages. The alignment beams were relayed using the appropriate optics, including beam splitters, quarter-wave plates, pixellated mirrors, and bulk macrooptic lenses, before being directed onto specialized detectors. The bicell detectors (BCDs), consisting of two side-by-side detectors located at the edges of the smart pixel chips in stages 1 and 2, were the backbone of the misalignment detection system. As shown in Figure 10(b), using two sets of BCDs, positioned in both horizontal and vertical configurations, lateral misalignment in both x and y-axes, respectively, was determined by measuring the differential power obtained from the beam incident on a BCD. Using this technique, *in situ* misalignment measurement was shown for ranges ±25μm and ±40μm.

Adaptive alignment via aperture steering suffers one major drawback. Typically, realignment of the components in the detector plane is accomplished using customized mechanical translation stages and the requisite electronic equipment to control the lateral and angular displacements. Although accurate and readily available, these additional control components are bulky and costly, thereby making this approach cumbersome and impractical for commercial applications.

2.2.2.2 Spatial Redundancy

A second approach to achieving adaptive alignment exploits the idea of using redundant optical components to achieve adaptive alignment in FSOIs. In typical interconnect designs, a single transmitter and receiver, along with the requisite optics, are used to encode each individual channel. An alternative approach, however, uses arrays of emitters and detectors to represent a single optical channel. Active alignment is then achieved by using spatial redundancy to actively select the most efficient channel in the FSOI.

One such implementation, documented in [6], used 3x3 arrays of VCSELs and PDs to provide adaptive alignment in a double bi-directional free-space optical interconnect. The redundant optical design was accompanied by an optimized optical link designed to

provide maximum power coupling efficiency between emitters and detectors under all cases of lateral and angular misalignment. Each optical link design consisted of a planar microlens (PML) array to collimate the VCSEL beams, an achromatic macrolens optical relay, and a receiver lens to direct the beams onto the PDs. As shown in Figure 11, a 2x2 array of these links made up the interconnect.

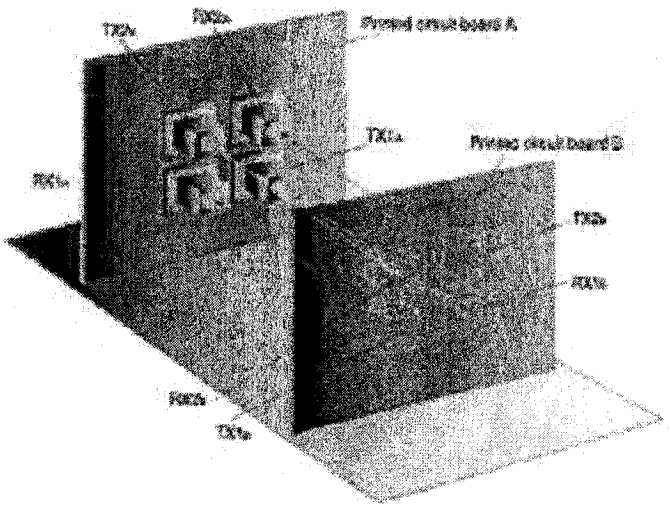

From: Bisaillon et al., Free-space optical link with spatial redundancy for misalignment. IEEE Phot. Tech. Lett. 14, 2002, pp. 242-244.

Figure 11 - FSOI with Spatial Redundancy for Active Misalignment Compensation

Theoretical results indicated that for both ±1mm lateral and ±1° angular misalignments, at least a single VCSEL-PD pair existed that minimized the coupling losses between the chips. Active alignment was therefore accomplished by using the most efficient optical link. Experimental measurements verified these results, indicating that for a 20cm PCB separation, the system could actively compensate for magnitudes of lateral and angular misalignment of 1.2mm and 1.1°, respectively.

Although, the use of spatial redundancy represents a novel implementation of an adaptively aligned free-space optical interconnect, the main disadvantage of this approach derives from the use of redundant components. Multiple VCSELs and detectors are required to implement a single channel, therefore increasing the power consumption and the space required to implement the free-space link. As a result, this approach does not

scale well for large channel counts, and is therefore impractical for high-density, highly parallel FSOI configurations.

2.2.2.3 Beam Steering

Real-time alignment via beam steering offers potential solutions to both of the above adaptive alignment techniques. In this approach, existing components are used to redirect beams appropriately to compensate for misalignment. As these are components are integrated into the FSOI design, real-time, post-assembly realignment is possible, thereby avoiding unnecessary changes to the channel make-up of the FSOI, as well as cumbersome mechanical alignment stages.

Microelectromechanical (MEMS) systems are devices with dimensions on the orders of micrometers created using standard surface micromachining technology. MEMS devices lend themselves well to the above approach as they are considered active devices and, owing to recent advances in surface micromachining technology, have been extensively designed for photonic applications.

One such a system, documented in [17], employed MEMS-controllable microlens arrays as beam-steering components for precision, active misalignment compensation in a FSOI. In this system, polymer microlenses of focal length 52.5μm and circular diameter 30μm were fabricated on a 4x4 array of square 80μm MEMS X-Y movable plates using multi-user MEMS processes (MUMPs). Figure 12 shows scanning electron microscope image of the MEMS-microlens structure.

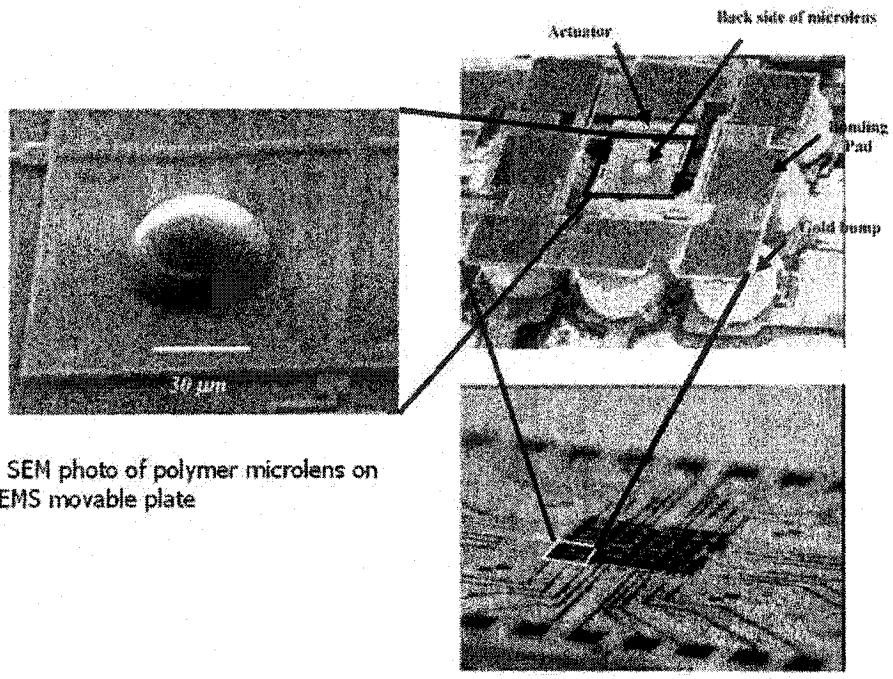

b. SEM photo of polymer microlens on MEMS movable plate

a. SEM photo of 4x4 MEMS-controllable microlens array

From: Tuantranont et al., "MEMS-Controllable Microlens Array for Beam Steering and Precision Alignment in Optical Interconnect System," Proceedings of the 2000 Solid-State Sensor and Actuator Workshop, Hilton Head Island, SC, pp. 101-104, June 4-8, 2000.

Figure 12 - SEM Photos of MEMS-controllable Microlens Array
a. MEMS X-Y movable plate with polymer microlens, b. Polymer microlens.

A two-dimensional array of VCSELs was positioned at the focal length of the MEMS-microlens array in order to collimate the divergent VCSEL beams. Using electro-thermal actuators, beam steering was accomplished by translating the MEMS-microlens structure in x or y-axes.

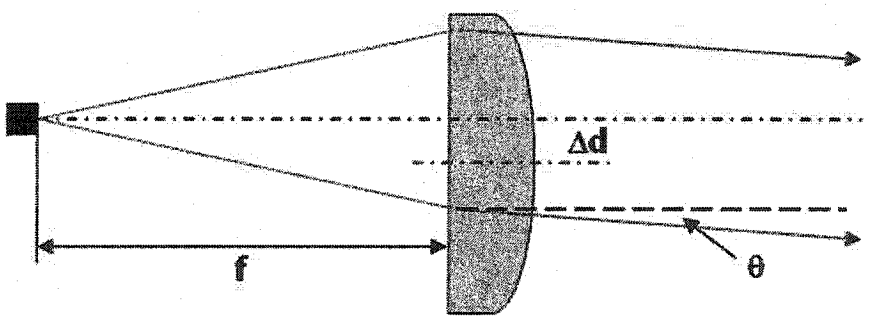

Figure 13 - Decentered Microlens Beam Steering

As shown in Figure 13, if the microlens is decentered laterally by a distance, Δd, the incident VCSEL beam is collimated, but is also refracted at an angle, θ, given by the expression,

$$\theta = \arctan\left(\frac{\Delta d}{f}\right) \tag{1}$$

where f is the focal length of the microlens. Large beam steering angles can be achieved by maximizing the ratio between the focal length and the lateral displacement of the MEMS movable plates. In the experimental setup, the MEMS-controllable microlens array was actively aligned with the VCSEL array, and a Keplerian telescope lens setup was used to achieve collimated beam steering. Experimental results indicated a maximum beam steering of 70 mrad ($\sim 4^{\circ}$), an adequate level of angular deflection for correcting for component misalignment in a typical FSOI.

The above adaptive alignment implementation demonstrates that MEMS devices have promising applications for real-time alignment in FSOIs. They are robust, and using commercially available standard foundry processes are highly customizable and integrate well with existing electronics.

It is for these reasons that a new approach for achieving adaptive alignment via beam steering was developed – employing MEMS micro-mirror arrays as the beam steering components. The following section describes the basic designs and operating principles of MEMS micro-mirrors, therefore highlighting the motivating factors for the use of micro-mirrors for real-time misalignment compensation in FSOIs.

2.3 MEMS Micro-mirrors

Extensive prior work has been done in the McGill Photonic Systems Group designing, characterizing, and integrating MEMS devices for photonic applications. In particular, numerous MEMS micro-mirror designs have been investigated, including thermally actuated micro-mirrors, scratch-drive rotor actuated micro-mirrors, and two-axis rotational micro-mirrors. All designs were fabricated using the standard multi-user

MEMS processes (MUMPs) offered by CMC Microelectronics. Based on the work done by Julianna Lin, documented in [18] and [19], two-axis rotational micro-mirrors were determined to be best suited for this application, for reasons which will become apparent at the conclusion of this chapter. The following section briefly describes the MUMPs process as well as the characteristics of two-axis rotational micro-mirrors.

2.3.1 Multi-User MEMS Processes – MUMPs

The MUMPs process is a three-layer polysilicon surface micromachining process that uses polysilicon as the structural material, and a deposited oxide of phosphosilicate glass (PSG) as the sacrificial layer [20]. Figure 14 is a cross-section of the 7 layers in the process – poly0, poly1, and poly2 refer to the three structural polysilicon layers.

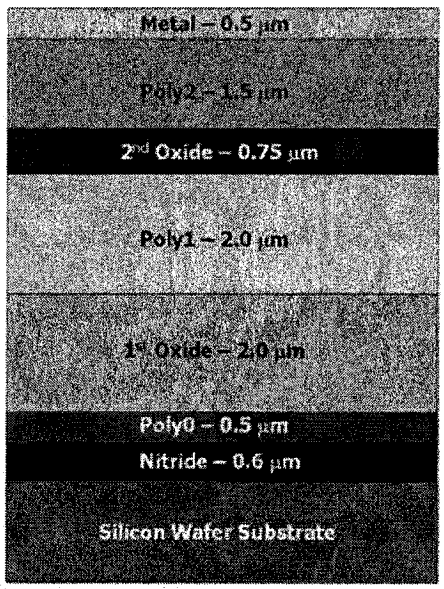

Figure 14 - Layer Cross-section of CMC MUMPs process

In micro-mirror design, both poly1 and poly2 can be used to create the suspended mirror surface. This is accomplished by specifying areas of these layers to be released in the lithographic mask design. The poly0 layer is fixed to the silicon wafer substrate and is therefore used to design the address electrodes required for mirror actuation. As polysilicon has a relatively low reflectivity, an optional layer of metal allows for the fabrication of highly reflective mirror surfaces. A total of twelve lithographic masks are used to create the required MEMS device, with the designer specifying the structural

details through the polysilicon layer mask designs. The following section details two-axis rotational micro-mirror designs fabricated using the MUMPs process

2.3.2 Two-axis Rotational Micro-mirrors

2.3.2.1 Basic Design

Figure 15 shows an SEM photo of a basic design of a two-axis rotational micro-mirror.

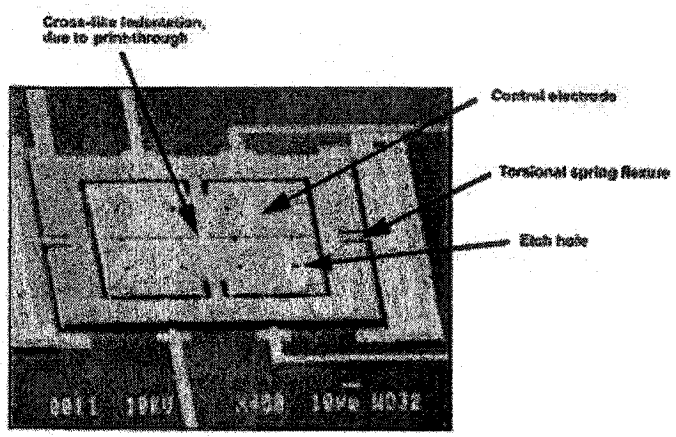

From: Lin et al., J. Microlith., Microfab., Microsyst. 1 (2002), pp. 70-78.

Figure 15 - SEM Photo of Two-axis Rotational Micro-mirror

The reflective mirror surface, consisting of either metal coated or uncoated poly1 or poly2 material, is suspended above the substrate by two anchor structures on either side of the mirror surface. An array of control electrodes, constructed using the poly0 material, is positioned beneath the mirror surface on the substrate. The resulting gap between the mirror surface and the electrodes is characterized by layer thicknesses in the MUMPs process (Figure 14). Mirror deflection in two-dimensions is accomplished by designing springs, in the form of flexure beams, connecting the mirror surface to the anchor structures. These springs can be designed in a variety of ways, depending on the mirror surface area and application. In the above example, the mirror is suspended using a structure known as a gimbal, created by two pairs of flexure beams, that act like torsion springs, allowing the mirror to rotate along two orthogonal axes [18], [21].

2.3.2.2 Operation

Fundamentally, two-axis rotational micro-mirrors operate based on the principles of a parallel plate capacitor. In this case, the upper and lower plates refer to the polysilicon mirror surface and the control electrodes, respectively, and are separated by a gap, *d*, as shown in Figure 16 below.

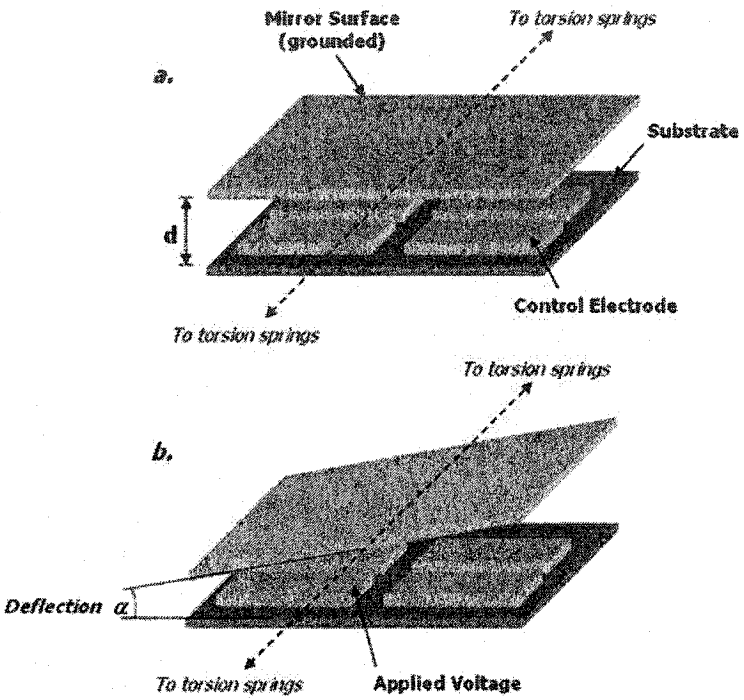

Figure 16 - Basic Operation of Two-Axis Rotational Micro-mirror
a. Mirror at Rest, b. Applied Voltage – Deflection, α

A ground electrode is connected to the anchor structure, thereby grounding the mirror surface. If a voltage is applied to a pair of control electrodes, a potential difference forms between the mirror surface and the substrate. An electrostatic attraction, in the form of an electrostatic torque, is, in turn, created between mirror and substrate, causing the portion of the mirror surface suspended above the control electrodes to be pulled towards the substrate. At the same time, the torsion springs exert a mechanical torque that resists this attraction. The mirror surface will stop when the mechanical torque is equal to the electrostatic torque generated by the control electrodes. At its final position, the mirror surface is rotated at an angle, α, about the axis of the flexure beams [Figure 16(b)].

Evidently, the larger the magnitude of the voltage applied, the larger the electrostatic torque on the mirror surface, resulting in increased angular deflection of the micro-mirror surface. However, mirror deflection is not without limit. The maximum mirror surface deflection occurs at a condition known as 'pull-in', when the electrostatic torque overcomes the maximum sustainable mechanical torque exerted by the torsion springs. At this point, the mirror surface is pulled into contact with the substrate, creating a short circuit between the control electrode and ground. The deflection angle of the mirror just before pull-in condition is known as the critical angle.

2.3.2.3 Design Considerations

As these MEMS devices are used to deflect beams of light, the most important criterion for characterizing their performance include the maximum mirror deflection and the required pull-in voltage, surface quality, and reflectivity of the mirror surface. Four major aspects of the mirror design that must be considered in producing a mirror that optimizes all three of the above characteristics include the mirror surface size, torsion spring design, electrode designs, and surface coating.

a) Surface Quality

The larger the mirror surface dimensions, the larger the degree of surface sag, thereby creating a concave mirror surface. Support structures, such as tethers may be used to keep the surface from adhering to the substrate during layer releasing in the MUMPs process. However, the torsion spring designs and mirror surface thickness have the greatest effect reducing the surface sag. The stronger the mirror hinge structure, the more resistant the mirror structure is to surface sag. At the same time, increasing the strength of the torsion springs has the effect of increasing pull-in voltages, as well as causing non-uniform deformation of the mirror surface during actuation. Additionally, increasing the thickness of the mirror surface causes a corresponding increase in the stiffness of the surface. However, as the thickness increases, so does the weight, and therefore, for a large surface area, increased weight causes surface sag. Thus, there exist fine balances between surface sag and the stiffness of the micro-mirror surface, and between surface size and surface quality.

b) Electrode Design

Additionally, electrode design also has a two-fold effect on the mirror surface quality. First, due to the lack of planarization steps in the MUMPs process, the mirror surface conforms to the topography of the lower layers [18]. This condition, known as print-through, increases beam scattering and therefore losses at the mirror surface. This can be compensated for by modifying the size and position of the address electrodes beneath the mirror substrate. This, however, in turn, effects the deflection of the mirror surface, and therefore, the required pull-in voltages. Thus, a second trade-off exists between electrode design and the quality of the mirror surface.

c) Surface Reflectivity

A third major design consideration is the reflectivity of the mirror surface. When the mirror surface is constructed solely of the standard polysilicon, the reflectivity of the mirror suffers, as the reflectivity of polysilicon is approximately 50%. This problem may be solved by depositing an additional metal layer on top of a poly2 mirror surface, as is offered by the MUMPs process. This allows for an increase in the reflectivity of the mirror surface to approximately 90%. However, this improvement comes at a cost. As a result of lack of annealing steps after the deposition of the metal layer, the residual stresses on a metalized mirror surface are greater [19]. Correspondingly, post-releasing, the mirror surface sags to a much larger degree when compared to a non-metalized polysilicon mirror surface. Such an increase in curvature, in turn, leads to undesirable aberrations at the mirror surface.

2.3.2.4 Implemented Designs – Results

Taking into account the majority of the above design criteria, two major designs were implemented by Lin et al [18].

The first design, shown in Figure 15, employed a square 130μm mirror surface created using the same gimbal torsion spring structure described in section 2.3.2.1. Mirror deflection was facilitated by a 2x2 array of square address electrodes positioned in

quadrants underneath the mirror surface. Lateral deflection was accomplished by applying a voltage to adjoining pairs of electrodes, whereas deflection along the diagonal of the mirror surface was accomplished by applying a voltage to individual address electrodes. Figure 17 shows a sample graph of the mirror surface tilt versus the applied voltage.

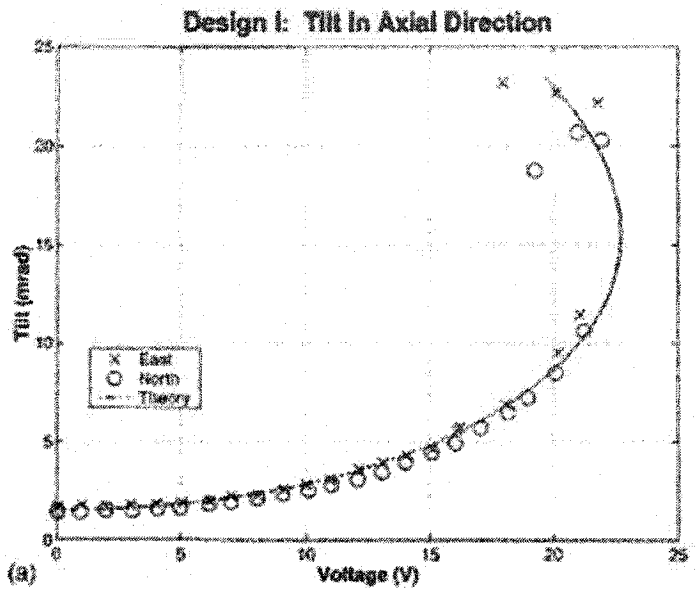

From: Lin et al., J. Microlith., Microfab., Microsyst. **1** (2002), pp. 70-78.

Figure 17 - Design 1: Graph of mirror tilt vs. voltage

Average pull-in voltages for lateral directions varied from 21.8 V to 21.9 V, and 26.3 V in the diagonal directions, resulting in maximum angular deflection at pull-in ranging from 19.4 to 23.4 mrad. Pull-in condition was characterized by a sharp increase in the mirror tilt and hysteresis in the above curve, due to a temporary adhesion of the mirror surface to the substrate. The critical angle for this design was determined to be approximately 12mrad. As seen in Figure 15, this mirror design had reduced surface quality due to print-through. Additionally, a slight surface curvature had the effect of reducing the maximum mirror deflection angle.

The second design strove to improve on the results of the first, by modifying the electrode geometry. In this design, the electrodes were moved to the edges of the mirror surface and the shape of the electrodes was changed in such a way that lateral deflection could be

accomplished using a single electrode, as opposed to a pair of electrodes in design 1. Figure 18 shows a SEM photo of the mirror.

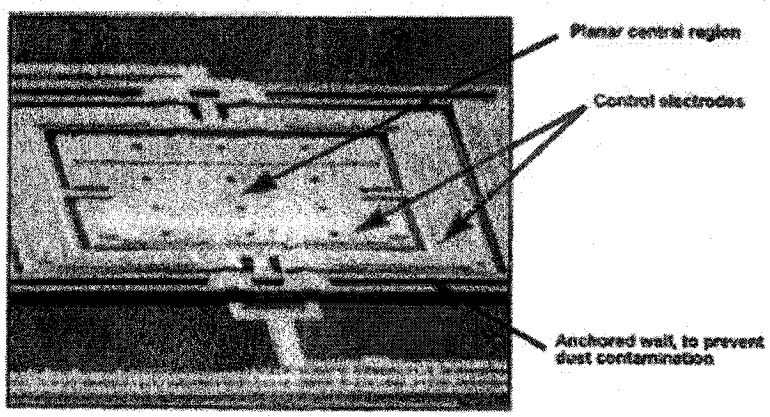

From: Lin et al., J. Microlith., Microfab., Microsyst. 1 (2002), pp. 70-78.

Figure 18 - SEM photo of Design 2

Results indicated improved surface quality, increases in lateral pull-in voltages, while maintaining similar tilt-voltage characteristics. The positioning of the electrodes at the outer edge of the mirror surface created a planar central region, with dimensions 70μm by 100μm, free of defects. As was the case in design 1, the critical angle was measured to be 12mrad.

Both of these designs could be used in an analog fashion to deflect beams at angles less than 12mrad. Above this value, however, hysteresis would make the mirror operation more difficult due to the effects of pull-in. Nevertheless, maximum deflection angles of ±23mrad were observed, indicating a significant degree of beam deflection possible.

2.4 Adaptive Alignment – MEMS Micro-mirrors

Considering the above work, MEMS micro-mirrors were selected as a viable technological platform for an adaptive alignment system for two reasons.

First, standard surface-micromachining MUMPs processes significantly reduce the complexity of MEMS micro-mirror design, compared to alternative non-standard commercial processes. Under such a process, reliable prototypes can be fabricated with

reasonably short turnaround times [18]. To this end, MEMS micro-mirror designs using the MUMPs process have been widely developed, as is evident from the work in [18], [19], and have proven reliability.

Second, the level of angular deflection obtained from surface micromachining is sufficient to provide an adequate level of lateral beam steering in the test platform, previously described. Given a total optical throw of 83mm from transmitter to receiver, it follows that the beam propagation distances between optical modules in this system are typically on the orders of millimeters. As shown in Figure 19, for a beam traveling from module 1 to module 2, incident on a mirror oriented at an angle $\theta = 45^{\circ}$, angular deflections, α, at the mirror result in a lateral deflections, Δh, at module 2.

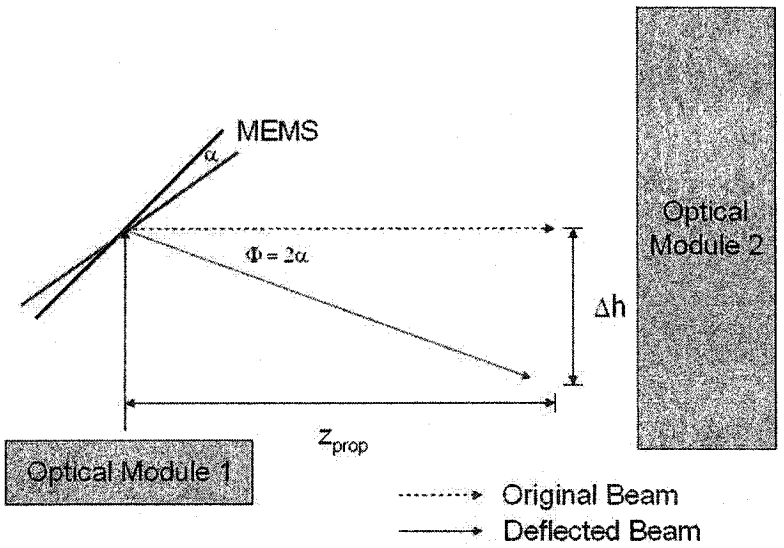

Figure 19 - Lateral Beam Deflection from Angular Tilt, α, of mirror at angle $\theta = 45^{\circ}$

For an on-axis beam, the lateral deflection at module 2, Δh, for a mirror deflection, α, is given by the expression,

$$\Delta h = z_{prop} \cdot \tan(2\alpha) \tag{2}$$

where z_{prop} refers to the propagation distance between the mirror surface and module 2. Clearly, for large propagation distances between the mirror surface and module 2, small angular deflections translate into large lateral beam deflections at module 2. For example, if the mirror described in section 2.3.2.4 is deflected at its critical angle of 12mrad, and is positioned at a distance of 4.25mm from module 2, using equation (2), the lateral

deflection experienced by a beam incident on the center of the mirror is approximately 102μm. In such a configuration, the MEMS micro-mirror may be used to compensate for 102μm of lateral misalignment in module 2, a sufficient level of lateral deflection for misalignment compensation in FSOIs.

2.5 Summary

The necessary background information for this project has been presented. The Demo 1.5 FSOI, the test-platform for this project, is a highly parallel optical link between two in-plane PCBs separated by a distance equivalent to a 1" board-to-board spacing in a rack configuration. Despite its novel implementation, the system has the same main drawback as other FSOI designs – a low-tolerance to component misalignment. Alignment techniques can be classified into three main categories – passive, active, and adaptive alignment techniques. Examples of each have been discussed. MEMS micro-mirrors have been widely fabricated using commercially available standard surface-micromachining, have shown promising beam steering angles, and have proven reliability. They offer a novel approach to achieving beam-steering and therefore adaptive misalignment correction in FSOIs. The following section describes the aforementioned adaptive alignment scheme, integrating MEMS micro-mirror arrays with the Demo 1.5 FSOI test-platform.

3.0 System Design

This chapter describes the development of an adaptive alignment scheme for the Demo 1.5 free-space optical link. The initial design considerations, the integrated MEMS-Demo 1.5 system, the implemented MEMS micro-mirror designs, and an analysis of potential performance issues for the modified free-space optical link are described.

3.1 Design Considerations – Adaptive Alignment

In integrating the MEMS micro-mirrors into the Demo 1.5 system, two major design considerations were addressed.

The first involved *how* the MEMS micro-mirrors would integrate into the existing optical design. As discussed in section 2.1.1.2, the optical relay for the Demo 1.5 system was based on a clustered mini-channel configuration. In this scheme, the beams from each individual cluster were initially collimated by an array of microlenses, before being relayed using a much larger minilens. Adhering to this topology required that beam steering be performed by mirrors with dimensions similar to those of the minilenses. As a result, a single MEMS micro-mirror per OE cluster topology was selected.

The second major consideration involved *where* the MEMS micro-mirrors would be positioned in the existing optical design in order to provide maximum misalignment correction. In examining this criterion, is it useful to consider a general case of the behavior of an off-axis collimated beam in a 4-f telecentric system.

Two types of misalignment must be considered – lateral displacement and angular tilt. Figure 20(a) and (b) shows schematics of both cases. For simplicity, both are considered to occur in the transmitter plane, denoted *TX*.

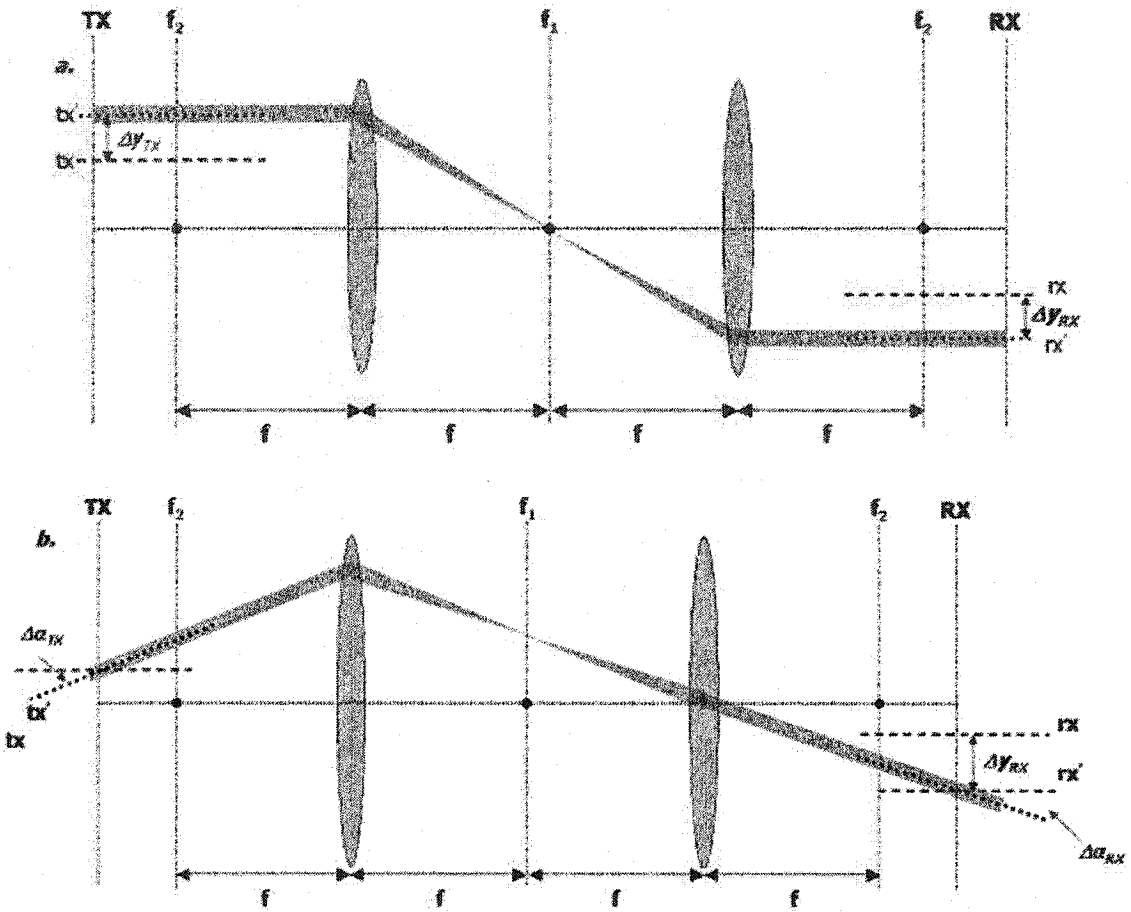

Figure 20 – Positioning of MEMS Micro-mirrors: 4-f Telecentric System
a. Lateral Misalignment of TX Plane, b. Angular Tilt Misalignment of TX Plane

As shown in Figure 20(a), lateral misalignment of the beam in the transmitter plane, Δy_{TX}, results in a corresponding shift of the beam at the receiver plane (*RX*), Δy_{RX}. On the other hand, angular misalignments of the transmitted beam, $\Delta\alpha_{TX}$, result in a lateral displacement, Δy_{RX}, as well as an angular tilt, $\Delta\alpha_{RX}$, of the beam in the receiver plane.

Correction for these misalignments can be accomplished by placing the MEMS micro-mirrors at two different points in the 4-f system. First, the mirrors may be positioned at the focal plane between the telecentric lenses, denoted f_1 in Figure 20, whereas in the

second configuration, the two mirrors may be positioned in two tilt planes located at the front and back focal points of the two lenses, denoted by f_2 in Figure 20.

In the former case, the mirrors are located in a single tilt plane, and therefore can be considered to possess only a single degree of freedom for correcting for misalignments. Figure 21 shows the corrected states for lateral and angular misalignments for a mirror located at this position.

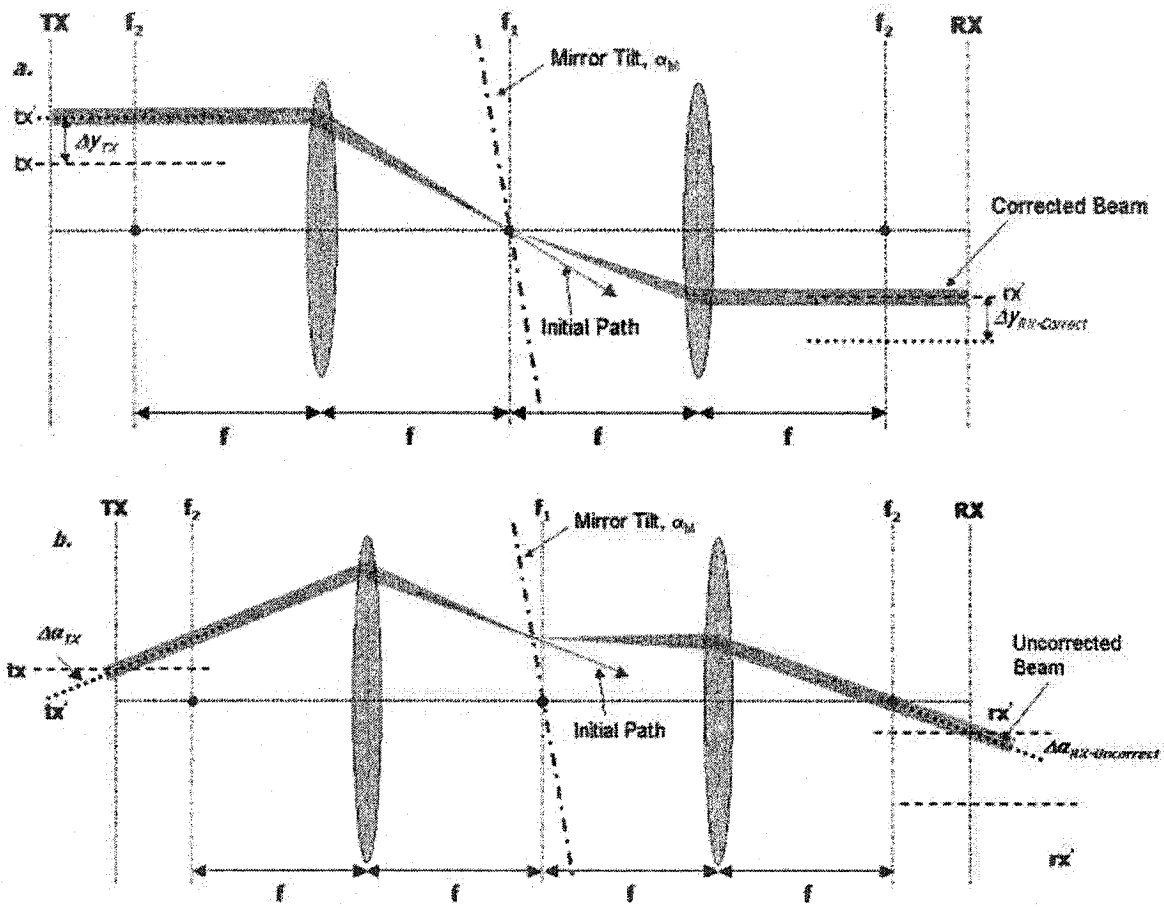

Figure 21 – Mirror Configuration 1
a. Lateral Misalignment – Full Correction,
b. Angular Tilt Misalignment Correction – Partial Correction.

Lateral misalignments, as they only involve one degree of displacement, can be easily corrected by deflecting the beam on the appropriate path at the focal plane of the lenses, [Figure 21(a)]. However, as angular misalignments generate two degrees of misalignment at the receiver plane, only partial correction can be achieved in this

configuration. As shown in Figure 21(b), either the lateral misalignment or the angular tilt of the beam can be corrected, not both.

However, in the latter configuration, as the mirrors are positioned at two separate tilt planes, located at the front and back focal planes of the telecentric lenses, the system inherits two degrees of freedom, as it pertains to correcting for misalignments. Tilting the mirrors in a complementary fashion, complete correction for both lateral and angular tilt misalignments can be accomplished. As shown in the schematics in Figure 22, this is done in such a way that the first mirror generates the required corrective lateral displacement, while the second mirror is tilted at such a way to redirect the beam parallel to the optical axis of the receiver.

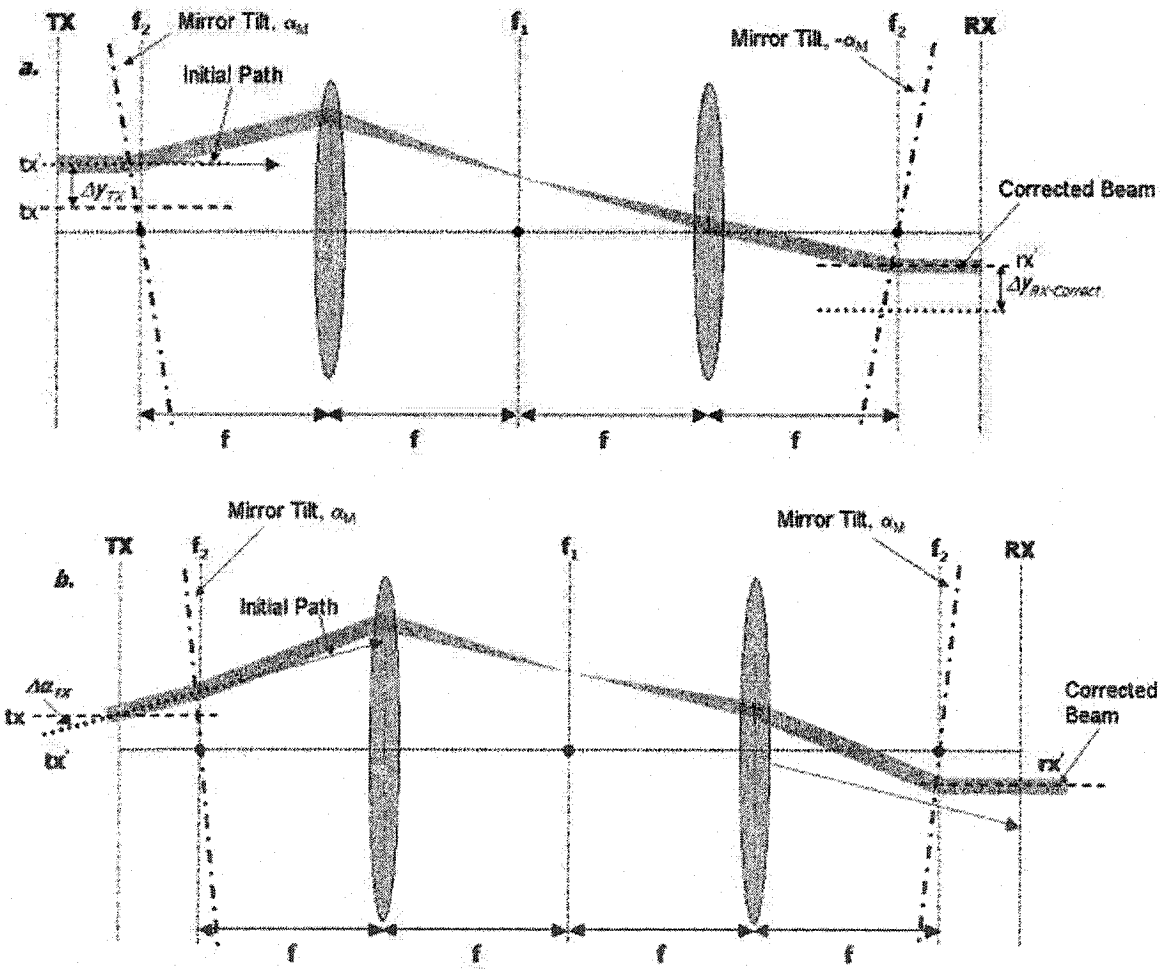

Figure 22 - Mirror Configuration 2
a. Lateral Misalignment – Full Correction, b. Angular Misalignment – Full Correction

It is for this reason that, in order to obtain maximum possible tolerance to both lateral and angular misalignments, the latter configuration was selected.

Now, recall also in the original test platform, two right-angle prisms were located at the same positions, at either end of the relay module, with the purpose of allowing for communication between two *in-plane* PCBs. However, as discussed in section 2.1.1.4, these components were a source of considerable loss, and were therefore ideal candidates to be replaced. By substituting the right-angle prisms with arrays of MEMS micro-mirrors, positioned at the front and back focal plane of the relay module, not only could these undesirable losses be avoided, but beam steering for lateral and angular misalignment compensation could also be accomplished.

The following section describes the modified Demo 1.5 optical link.

3.2 MEMS-Demo 1.5 System

Figure 23 shows a schematic of the integrated MEMS-Demo 1.5 free-space optical interconnect.

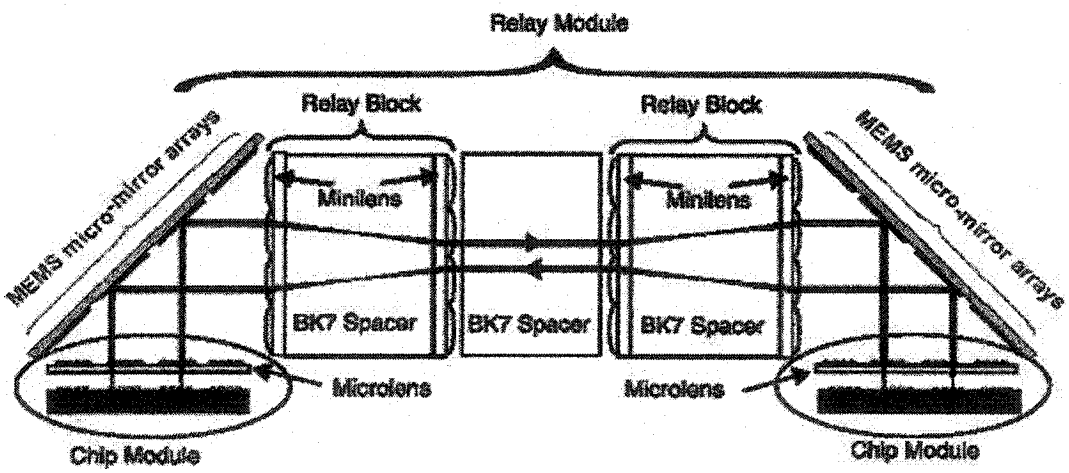

Figure 23 – Schematic of Integrated MEMS-Demo 1.5 FSOI

In order to alleviate the misalignment limitations of the original Demo 1.5 system, the proposed solution replaced the right-angle BK7 prisms with arrays of MEMS micro-mirrors at an angle of 45° at either end of the relay module. A single square mirror-per-

cluster topology was used, providing the necessary 180° optical throw, in addition to allowing for beam steering for misalignment correction. The MEMS mirrors were designed according to both dimensional restrictions imposed by the existing system components, as well as MUMPs process design guidelines. In order to significantly reduce the complexity of the numerical modeling of the active alignment system, a test version of the Demo 1.5 optical system was devised. The modified system, the implemented mirror designs, and several potential performance issues of the integrated system are described in the sections below.

3.2.1 FSOI Design Modifications – Test System

In integrating the MEMS micro-mirrors with the original Demo 1.5 FSOI, two major changes were made to the system setup.

3.2.1.1 Single Test Source

As was shown in Figure 4, the original source setup for the Demo 1.5 system consisted of two OE-VLSI chip modules with 4x8 clusters of 4x4 integrated VCSELs and photodetectors. Such a large number of devices translated in to a setup with complex alignment and drive electronics issues. As a result, a single source offset on the each chip module was selected in order to simplify both the simulation and laboratory setups. In order to most accurately characterize the performance of the modified system, the source with the worst-case center offset within a single cluster was selected. As shown in Figure 24, for the 4x4 device configuration used, the position of the worst-case source was located at distances of 187.5μm offset in both x and y directions from the center of a cluster.

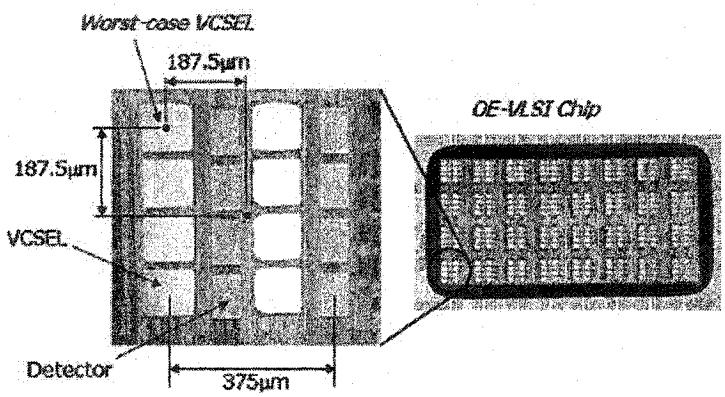

Figure 24 - Worst-Case Source Position

For the simulations described in chapter 4, this worst-case source position was used to characterize the performance of the MEMS integrated FSOI.

3.2.1.2 Single Optical Relay

As previously described, the Demo 1.5 system employed telecentric pairs of minilens arrays to image between the clustered devices on the OE-VLSI chip. Separated by BK7 glass spacers to allow for increased optical throw between transmitters and receivers, each of these modules was referred to as a *relay block.*

However, in determining the viability of using MEMS micro-mirrors for adaptive misalignment correction in FSOIs, the total optical throw between the transmitter and receiver was *not* a key design consideration. Thus, in order to simplify the numerical modeling of the integrated system only a single relay block, consisting of a pair of diffractive minilenses and a BK7 glass spacer, was used. These three optical elements formed what will from this point onwards be referred to as the *minilens module.*

The test system is shown in Figure 25.

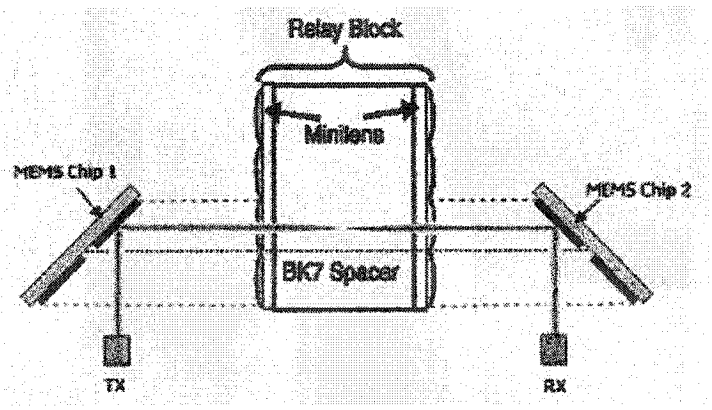

Figure 25 - Schematic of Simplified MEMS Demo 1.5 FSOI

The test system and its components will be described in chapter 4, detailing the numerical modeling of the integrated system. The following section describes the implemented MEMS micro-mirror designs.

3.2.2 MEMS Micro-mirror Arrays

The fundamental criterion for the MEMS micro-mirror designs was the use of a single mirror per cluster topology. As seen in Figure 5, the cluster-to-cluster spacing on the OE chip was fixed at 750μm. Given this dimension, it was initially determined the side length of the square micro-mirror *overall* structure was limited to 750μm. However, it was overlooked, at that time, that by orienting the mirrors at an angle of 45° to the direction of propagation, the apparent aperture in the *y*-axis of the mirror decreased by a factor of $\sqrt{2}$, from 750μm to 530μm. A potential solution to this problem is the fabrication of arrays of rectangular micro-mirror structures with one side length being equal to a factor of $\sqrt{2}$ more than the second side length - 750μm x 1060μm. This performance issue is discussed in further detail in section 3.2.3.1. Given time restrictions and fabrication delays, such a mirror design could not be prototyped, however, a theoretical model of the system under these ideal conditions was modeled and is presented in chapter 4.

Two designs of 750μm square micro-mirror structures were designed and fabricated under the MUMPs process. The allocated MEMS chip dimensions of 4.45 x 4.2mm

limited the maximum array size to 2x2. Figure 26 shows a CAD layout of the MEMS chip.

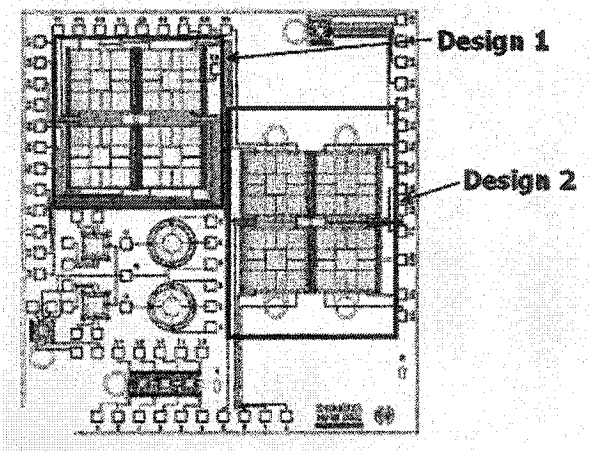

Figure 26 - CAD Layout of Implemented MEMS Chip

Both designs employed a similar design, in which the mirror surface was suspended above the substrate by a set of 4 flexure hinges, located at the corners of each mirror. At 750μm-square, the mirror surface was larger than any other designs previously implemented in the McGill Photonic Systems Group using the MUMPs process. Given this, it was predicted that mirror surface curvature would be another potential performance limiting factor for the integrated link. This potential problem is discussed in further detail in section 3.2.3.2 and experimental results are presented in chapter 5.

As a result, the flexure hinges used in both designs, shown in Figure 27, resembled thick, flat springs, and were designed in order to minimize sagging of the mirror surface.

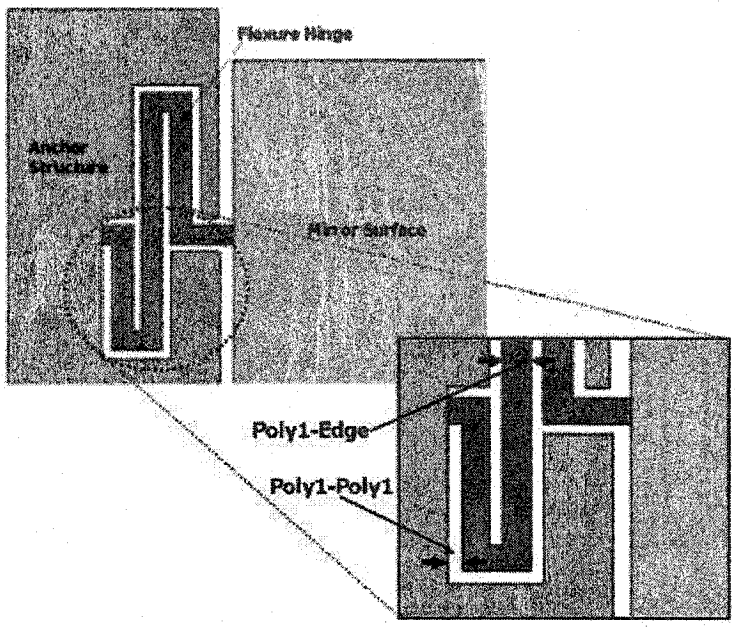

Figure 27 – Schematic of Supporting Mirror Flexure Hinges

The design of supporting structures had the effect of limiting the actual central mirror surface dimensions. Layer width thickness and spacing requirements for the principle polysilicon layers imposed by the MUMPs process required that certain structures be constructed with minimum dimensions. For example, as shown in the inset of Figure 27, MUMPs process guidelines specify a minimum poly1-edge spacing of 3μm and a minimum poly1-poly1 gap of 2μm [20]. Thus, the minimum possible width of the flat-spring flexure hinge design, as shown above, is 3μm. As well, considering an additional minimum spacing of 2μm between poly1 structures, the resulting effect of each bend in the corner hinges was to decrease the overall width of the mirror surface by 10μm. Factoring in the relatively large size of the mirror surfaces, the minimum poly1-edge spacing for the flexure hinges was scaled by a factor of 2, in order to allow for extra support. Ultimately, additional support structures had an effect of reducing the actual mirror surface by approximately 87μm per side-length, to 663μm-square, further indicating that beam clipping of the worst-case beam would have an effect on the performance of the integrated system.

In both designs, the mirror operation was governed by a set of 4 address electrodes and one ground electrode positioned in quadrants directly below the mirror surface. Shown in Figure 28, the size of electrodes was selected in such a way that the surface area of the mirror surface covered by the electrodes was maximized, in order to reduce the required pull-in voltages for the large mirror surface.

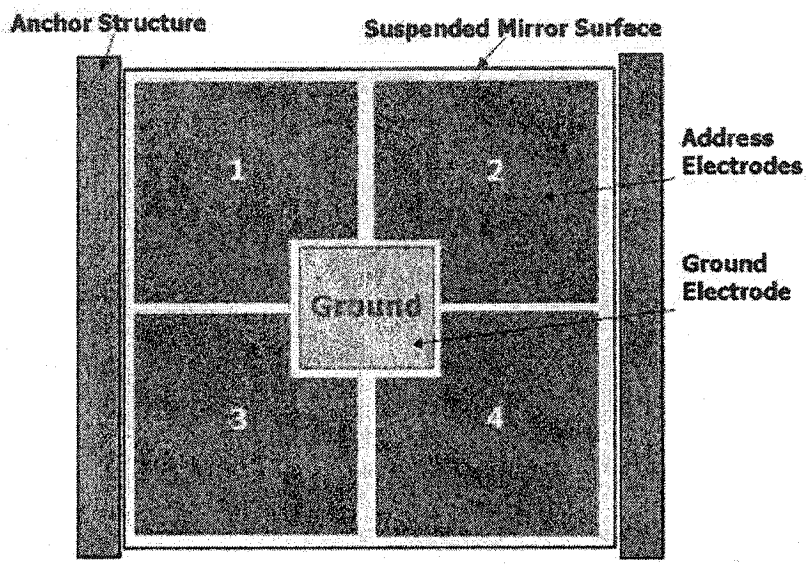

Figure 28 – Positioning of Address and Ground Electrodes

As was the case for the mirrors documented in [18], the size and position of the electrodes beneath the mirror surface were predicted to be potential performance limiting factors. These design considerations are discussed in further detail in section 3.2.3.

The distinguishing feature of the two implemented micro-mirror designs was the polysilicon layer used to create the mirror surface. The following two sections describe the characteristics of each design.

3.2.2.1 Design I

The first design employed a standard mirror surface constructed of the poly1 polysilicon structural layer.

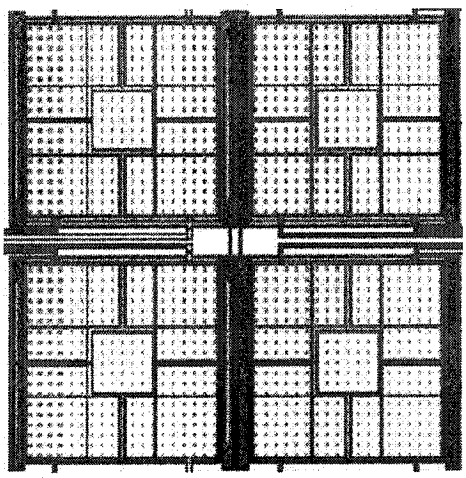

Figure 29 - CAD Layout of 2x2 Array of Micro-mirror Design I

As it can be seen from the MUMPs layer hierarchy shown in Figure 14, after removal of the first sacrificial oxide layer, this results in a mirror surface–substrate gap of magnitude, $d_{POLY1} = 2\mu m$.

As previously discussed, the maximum theoretical mirror deflection for a micro-mirror occurs during 'pull-in' – when the applied voltage is large enough such that the electrostatic force causes the suspended mirror surface to come into contact with electrodes. Without a rigorous analysis of the resulting torque on the mirror surface, an approximation of the maximum theoretical deflection can be easily obtained using simple geometry.

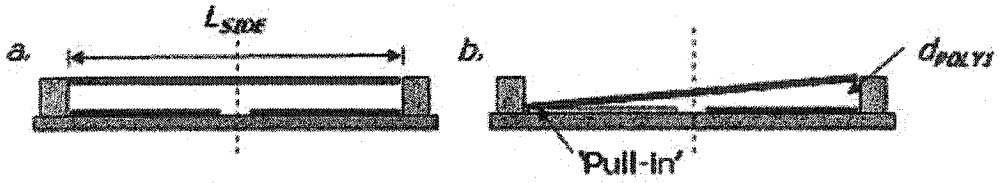

Figure 30 – Approximate Micro-mirror Maximum Theoretical Deflection Angle
a. Mirror at rest, b. Mirror at 'pull-in' (electrodes 1 and 4 operating)

As shown in Figure 30(b), during 'pull-in', the corner of the mirror theoretically drops a vertical distance, d_{POLY1}, contacting the address electrode on which the voltage has been applied. Knowing the side length of the mirror surface, L_{SIDE}, the maximum theoretical deflection, θ_{max}, can be determined from the equation (3):

$$\theta_{\max} = \arcsin\left(\frac{d_{POLY1}}{L_{SIDE}}\right) \quad (3)$$

Given L_{SIDE} = 663μm, the maximum theoretical deflection for design I mirrors was therefore determined to be $\theta_{Design1,\ max} \approx 0.1728^{\circ}$ or 3.01mrad.

3.2.2.2 Design II

The above theoretical pull-in angles were found to be significantly less than those obtained from the micro-mirrors described in section 2.3.2.4. This is largely due to the large size of the mirror surface relative to the surface-substrate gap offered by the poly1 design. As a result, design II employed a modified mirror surface in order to increase the maximum theoretical mirror deflection angle.

In the second design, the mirror surface was constructed of the poly 2 polysilicon structural layer. In order to facilitate the use of poly2 for the mirror surface, a 'pull-ring' structure composed of the poly1 layer was positioned directly beneath the mirror. Post-fabrication, the poly2 and poly1 layers are released and remain unattached. Additional corner connections between the poly1 layer and the anchor structures were inserted in the CAD designs. Known as tethers, these structures are used to keep the poly1 surface from adhering to the poly0 electrodes, post-releasing. During testing, a microscope is used to view the mirror and a metal probe is used to pull the 'pull-ring' structure, breaking the brittle poly1-anchor attachments, thereby sliding the poly1 structural layer out from underneath the poly2 mirror surface. Figure 31 shows a CAD schematic of the 2x2 array of design II micro-mirrors.

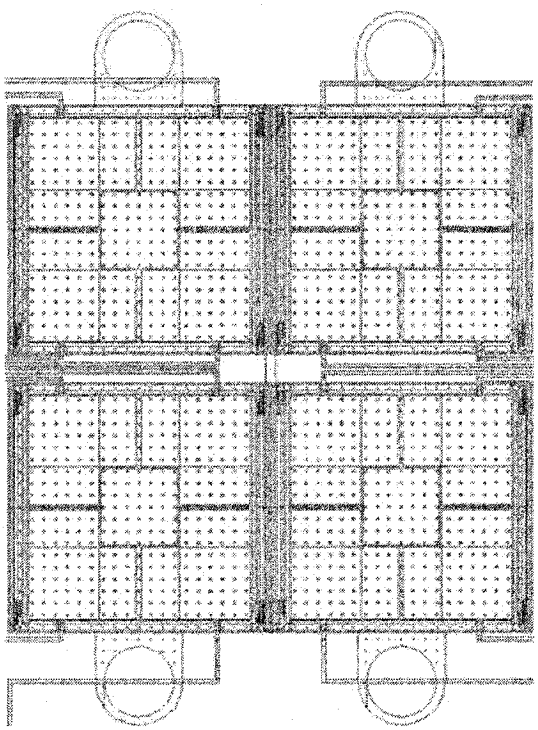

Figure 31 - CAD Layout of 2x2 Array of Micro-mirror Design II

A proven reliable technique used in the Photonic Systems Group, this theoretically allowed for an increase in the mirror surface to substrate gap from 2μm to 4.75μm, in designs I and II, respectively. From equation (3), the resulting maximum theoretical mirror deflection angle for design II mirrors was determined to be $\theta_{Design2,\ max} \approx 0.4105^{\circ}$ or 7.16mrad.

Additionally, as the thickness of the poly2 mirror surface layer is 0.5μm less than the poly1 surface in the MUMPs process, it can be expected that the degree of curvature will be less in magnitude, thereby resulting in increased losses at the mirror surface.

The testing and characterization of the above MEMS designs is described in chapter 5. The following section describes several performance issues pertaining to the integration of the MEMS micro-mirrors with the existing interconnect.

3.2.3 *Integrated System –Performance Issues*

The aforementioned MEMS devices were designed for optimal integration with the existing Demo 1.5 system. Despite this, two characteristics were determined to be potential limiting factors to the performance of the integrated system – 1) the optical aperture of the MEMS designs, and 2) mirror surface sag. These aspects and potential solutions are described below.

3.2.3.1 Beam Clipping - Optical Aperture of MEMS micro-mirrors

The issue of beam clipping at the micro-mirror surfaces is a two-part problem.

First, the maximum cluster spot size incident on the micro-mirror surface must be considered. Basic Gaussian beam propagation theory states that a beam will diverge from an optical source, with the waist of the beam evolving as a function of the position from the source, $\omega(z)$, given by equation (4),

$$\omega(z) = \omega_o \cdot \left[1 + \left(\frac{\lambda \cdot z}{\pi \cdot \omega_o^2}\right)^2\right]^{\frac{1}{2}} \tag{4}$$

where ω_o is the initial $1/e^2$ (13.5%) intensity beam waist radius, z is the propagation distance from the source, and λ is the wavelength [22]. In the far-field propagation regime, such that the propagation distance is sufficiently large, equation (4) reduces to,

$$\omega(z) \cong \frac{\lambda \cdot z}{\pi \cdot \omega_o} \tag{5}$$

At this point, the evolution of the beam waist radius may be approximated linearly from a point source, forming a cone with a full angle,

$$\theta = \frac{\lambda}{\pi \cdot \omega_o} \tag{6}$$

where θ is the far-field half-divergence angle of the beam.

Although, equations (4) through (6) model the evolution of a theoretical Gaussian beam, a real laser beam, such as the VCSELs used in the Demo 1.5 system, does not fit this exact

profile [22]. In order to model a real laser beam, the above equations must be modified, incorporating the M^2 factor, taking into account the variation of a real laser beam from the Gaussian model. Including the M^2 factor, the $1/e^2$ intensity beam radius of a real laser beam changes as a function of propagation distance by equation (7),

$$\omega(z) = \omega_o \cdot \left[1 + \left(\frac{z \cdot \lambda \cdot M^2}{\pi \cdot \omega_o^2}\right)^2\right]^{\frac{1}{2}} \tag{7}$$

, and the beam waist-divergence product in the far-field becomes,

$$\omega_o \cdot \theta = \frac{M^2 \cdot \lambda}{\pi} \geq \frac{\lambda}{\pi} \tag{8}$$

where $M^2 > 1$ for a real laser beam [22].

Using equations (7) and (8), an analysis of the evolution of a VCSEL beam waist radius from the microlens array to the minilens was performed, in order to determine the maximum spot incident on a micro-mirror.

As the microlens arrays were positioned at the focal length of the minilens arrays, the maximum possible spot on the micro-mirror was determined to occur at a distance of 8.5mm from the microlens. This is shown in Figure 32(a).

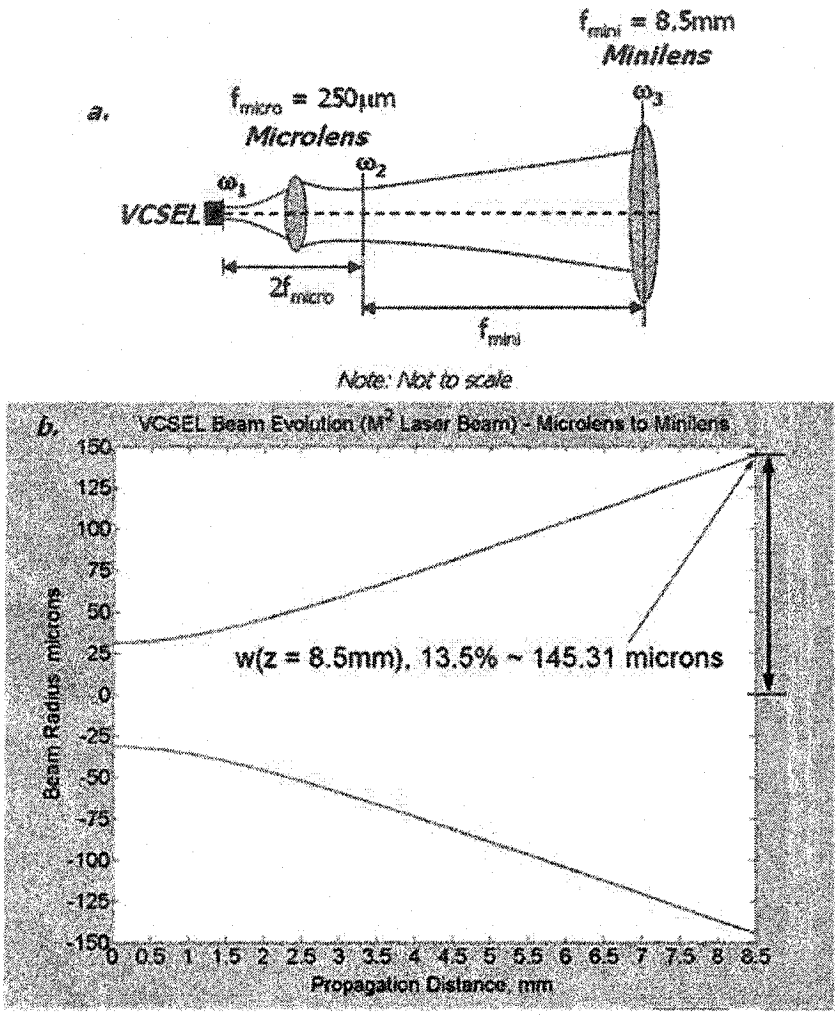

Figure 32 - Beam Waist Evolution between VCSEL and Minilens Arrays
a. Simplified telecentric system, b. Evolution of a Single VCSEL Beam

From equation (8), given a VCSEL mode field diameter (MFD) of 6µm and a full divergence angle of 20° at a wavelength of 850nm, the M^2 factor for the VCSELs was found to be approximately equal to 1.93. Knowing that $\omega_1 = 0.5(\text{MFD}) = 3\mu\text{m}$, the beam waist after the microlens was determined using equation (7) to be approximately $\omega_2 \approx 31.4\mu\text{m}$. Setting $\omega_o = \omega_2$, the waist radius over a propagation distance of 0 to 8.5mm was calculated using expression (7). The evolution of the waist radius is shown in Figure 32(b) above. The maximum $1/e^2$ intensity beam spot radius incident on the mirror, at a distance of 8.5mm from waist ω_2, from a single VCSEL was found to be $\omega_{13.5\%,\,max} \approx 145.31\mu\text{m}$. Recall, the $1/e^2$ intensity waist is related to the 99% beam intensity waist, $\omega_{99\%}$, by equation (9):

$$\omega_{99\%} = 1.5 \cdot \omega_{13.5\%} \tag{9}$$

Using this equation, the waist radius containing 99% of the VCSEL beam power was determined to be $\omega_{99\%,\,max} \approx 217.95\mu m$.

In order to evaluate the effect of the micro-mirrors on beam clipping in the Demo 1.5 system, the beam footprint from a single cluster centered on a MEMS micro-mirror oriented *perpendicular* to the direction of propagation of the beams was examined. Referring to Figure 33(a), given a device pitch of 125μm and a spot radius of 217.95μm per device, the aggregate M^2 beam spot from all of the sources forms a square of side length approximately 810μm. Evidently, for such a beam footprint, 8% clipping in both x and y-axes occurs at the minilens apertures.

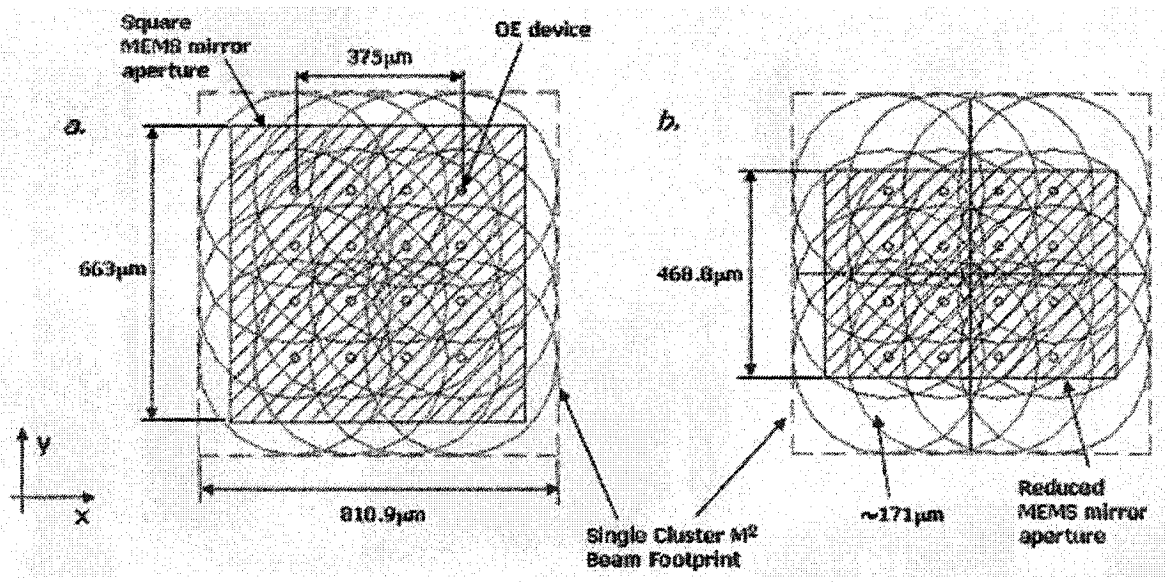

Figure 33 - Single Cluster M^2 Beam Footprint on Mirror Surface
a. Mirror oriented at 90° to axis of propagation, b. Mirror oriented at 45° to axis of propagation

As shown in Figure 33(a), the beams from the devices on the edges of the cluster are significantly clipped by the 663μm-square micro-mirrors, as 147.9μm, or 18% of the total beam footprint is clipped in both x and y-axes of the mirror surfaces.

As well, by orienting the micro-mirrors at the required 45° angle to the optical axis of propagation, additional clipping occurs. As shown in Figure 33(b), this has the effect of reducing the apparent optical aperture of the mirror by a factor of $\sqrt{2}$ in the y-axis, from

663μm to 468.8μm. As a result, the beam footprint is clipped in the *y*-axis by a total of 342.1μm, or approximately 42%. As shown above, almost 50% of the beams from those devices situated at the top and bottom edges of the clusters are lost due to clipping at the mirror surface.

The combination of the two effects has the effect of reducing the overall fill factor of the MEMS micro-mirrors, with respect to the aperture of the minilenses, to 88.4% in the *x*-axis and 62.5% in the *y*-axis – significant clipping for the sources at the edges of each cluster.

During the initial design phase, in order to adhere to a one-mirror-per-cluster topology, the latter effect was not taken into account. Nevertheless, this problem can be solved by using MEMS devices with rectangular surface dimensions of 750μm x 1061μm, in the *x* and *y*-axes respectively. Thus, even with the 45° orientation in the *y*-axis, the mirrors would have apparent optical apertures identical to the 750μm-square minilenses. In doing so, the M^2 beam footprint would only be clipped by approximately 8% at each mirror surface – a substantial improvement.

Due to time constraints and restrictions imposed by the current fabrication technology, such a MEMS micro-mirror design was not implemented. However, the performance of the above ideal MEMS implementation was modeled numerically and will be explained in detail in chapter 4.

3.2.3.2 Aberrations - Surface Sag of MEMS Micro-mirrors

A second major performance factor for the MEMS micro-mirrors is the radius of curvature of the mirror surface. Curvature results from a sagging of the mirror surface, inherent in suspending a thin surface over a large area.

In determining the effect of a beam incident on a curved mirror surface, a primary consideration is determining the mathematical shape of the concave surface. If we consider the mirror surface to be analogous to a homogeneous cable sagging from two

points positioned a distance apart, then the sagging mirror surface can be modeled using a hyperbolic cosine function with vertex at the origin, given by equation (10),

$$y = \cosh\left(\frac{x}{a}\right) - 1 \tag{10}$$

where x is the lateral distance from corner to corner, and a is characteristic of the physical properties of the mirror [23]. It can be shown that for small magnitudes of sag relative to large lateral mirror dimensions, x, the curve in equation (10) follows a similar profile to a spherical surface. Figure 34 shows both curves for a 663μm-square mirror and a mirror surface sag of 2μm.

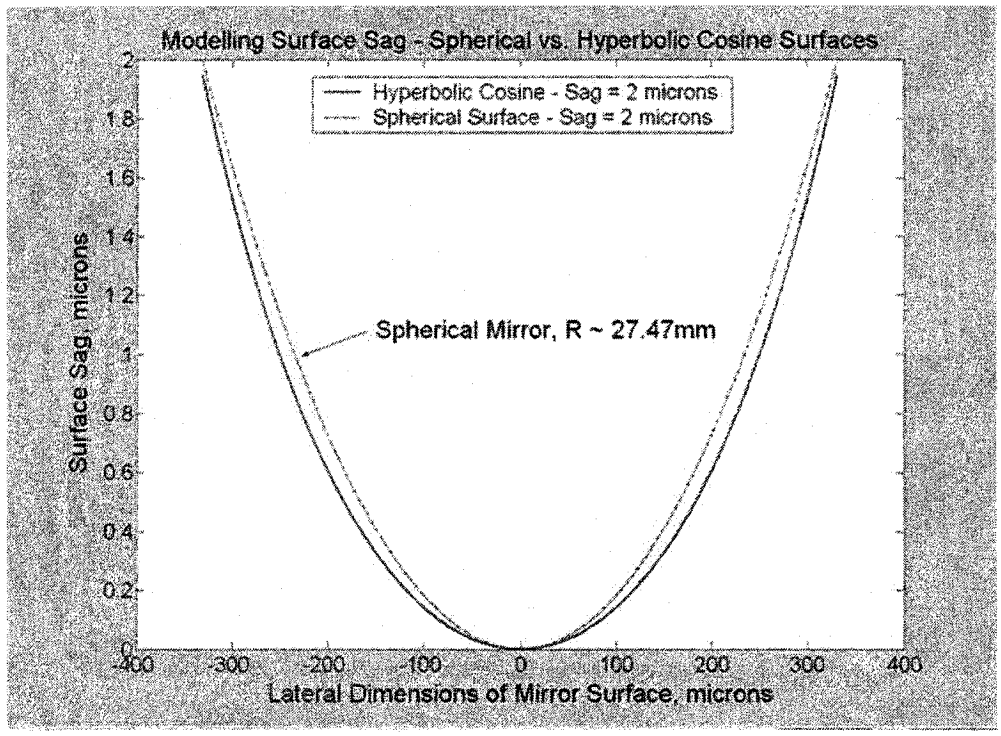

Figure 34 - Hyperbolic Cosine vs. Spherical Surface Profiles for Surface Sag

Recall, as shown in Figure 14, under the MUMPs process, for a standard poly1 mirror surface, 2μm of sag is equivalent to the center of the mirror touching the underlying address electrodes. Thus, assuming uniform sagging in all areas, Figure 34 shows that even for a relatively large degree of surface sag, the hyperbolic cosine profile may be approximated by a spherical surface.

Now, from basic optics theory, a spherical concave mirror surface has the effect causing an on-axis collimated beam to converge to a point, f, given by equation (11),

$$f = -\frac{R}{2} \tag{11}$$

where R is the radius of curvature of the mirror, and the minus sign derives from the focal point existing to the left of the vertex of the mirror, V [24]. This is illustrated in Figure 35(a).

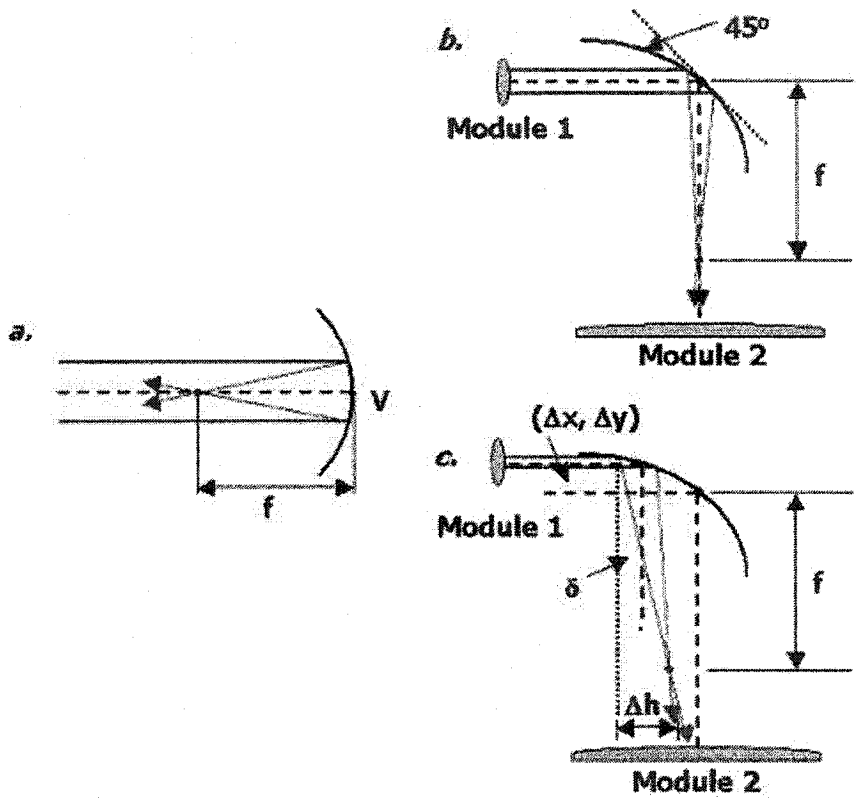

Figure 35 - Effect of Concave Mirror Surface on a On-axis Collimated Beam
a. Mirror oriented perpendicular to direction of propagation,
b. Effect of 45° Concave Mirror on an On-Axis Source,
c. Effect of 45° Concave Mirror on an Off-Axis Source

Now, as is the case with the MEMS-Demo 1.5 system, if the mirror is oriented at 45°, a similar defocusing of the beam occurs [Figure 35(b)]. Ultimately, this translates into an increase in the beam radius at the detector, and, therefore, clipping losses.

For an off-axis source, the effect is two fold. As is shown in Figure 35(c), considering a very small beam radius relative to the dimensions of the mirror, if the beam center is

positioned at a point $(\Delta x, \Delta y)$ off-axis, the concave mirror surface causes not only a defocusing of the beam, but also an angular deflection, δ, of the beam relative to its original path. Angular deflection at the mirror translates into a lateral deflection, Δh, at the subsequent optical module. Evidently, losses result from both effects. Section 4.4 examines both cases in further detail.

3.3 Summary

The design of an active alignment system for an existing free-space optical interconnect has been presented. MEMS micro-mirrors were selected as the appropriate technological platform for the active alignment system, and were determined to fit naturally within the existing optical system. Two micro-mirror array designs were implemented using a commercially available MUMPs surface micromachining process. However, based on process and existing system dimensional restrictions, beam clipping and losses at the mirror surfaces represent potential performance issues for the integrated system. The following section details the numerical modeling of the integrated system, and, using a simplified test version of the Demo 1.5 system, characterizes the improvement in misalignment tolerances offered by the MEMS micro-mirrors.

4.0 Numerical Modeling

Numerical modeling of the integrated system was performed using the Code V optical design software package, a powerful and flexible software tool with applications in image-forming and illumination systems, and, as is the case with this project, photonic and telecom systems. The purpose of such an analysis was to determine the degree to which MEMS micro-mirrors could improve the misalignment tolerances for various components in the Demo1.5 FSOI, as was as the effect of integrating the micro-mirrors into the existing system.

This section briefly introduces the Code V optical design system, followed by a detailed description of the integrated MEMS-FSOI system setup, the misalignment and mirror curvature simulations, and the corresponding results.

It must be noted that in all numerical simulations the key metric used to determine the impact of the MEMS micro-mirrors on the system performance was the power incident on the detector surface. From this point forward, all discussions of overall system throughput refer to the received power at the detector.

4.1 Code V

The Code V optical design software package was selected for the simulation of this system for several reasons.

First, Code V provides a full spectrum of analysis tools for the characterization of the performance of an optical system. Code V offers both real ray tracing and diffractive

beam propagation. Both tools are required for a full evaluation of the system under investigation.

Secondly, Code V allows a user to create and modify an optical design both visually and manually, using either the graphical-user interface or command-based prompting. From a first-order analysis, the graphical approach was invaluable for the creation of a static form of the modified interconnect and the evaluation of the performance of the system from a *'what you see is what you get'* perspective. A dynamic view of the system, using command-based scripts, however, was essential for performing a misalignment analysis of various system components. Run in the form of macros, customizable prompting scripts allow the user to perform various tasks repetitively with ease. A typical script can modify various system properties, activate any number of analysis simulations, sort the results, and finish by outputting desired results in the form of a standard text file for easy viewing and integration with additional analysis tools.

The following section describes the Code V system implementation, detailing the properties of each component.

4.2 Code V Implementation – MEMS-Demo 1.5 FSOI

As shown in Figure 25, the simplified test system employed a single transmitter and receiver, combined with a single relay block. In keeping with the idea of a single worst-case test source, a further simplification was made for the purpose of the Code V system modeling. This involved simulating the propagation of a test source through a single minilens element separated by a BK7 glass spacer. Figure 36 shows a basic schematic of the simulation setup.

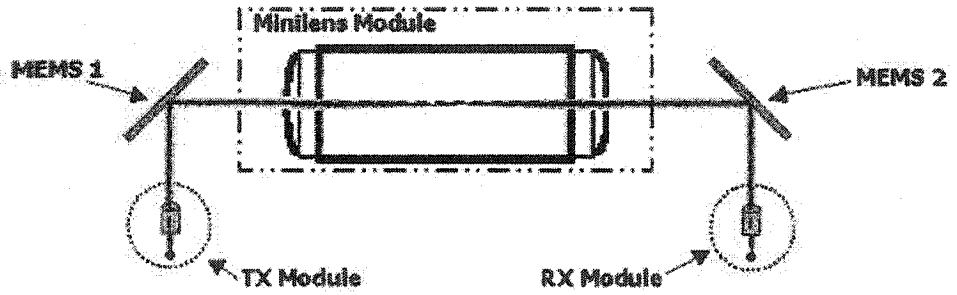

Figure 36 - Schematic of Simulation Setup for Integrated MEMS Demo 1.5 System

As the test system consisted of 9 separate optical elements, a simple and repeatable method was required in order to appropriately characterize component tolerances to misalignment. This was accomplished by grouping sets of individual elements into larger modules. In doing so, it was assumed that the components making up these modular blocks could be precision assembled during fabrication, and would therefore have negligible internal misalignment. The resulting system consisted of 5 separate modules – the transmitter module (TX), the micro-mirrors, labeled MEMS1 and MEMS2, the minilens module, and the receiver module (RX) [Figure 36].

Using the graphical-user interface, each optical component was implemented in the Code V environment. Table 5 in Appendix I shows a screen capture of the Code V Lens Data Manager, specifying the important properties of each of the 18 optical surfaces used to implement the system. The surfaces and their properties are explained in detail in sections 4.2.2 through 4.2.5, outlining the construction of the 4 major modular system components. First, however, an explanation of the co-ordinate system used to position each element in the system is necessary.

4.2.1 Decentered System – Global Coordinates

In the majority of optical systems, the mechanical and optical axes for each component are not coincident. In other words, the local coordinate axes of certain components can be tilt or offset with respect to other components. These are referred to as tilted or decentered systems. Code V allows for 7 different types of component decenters; differences in each arising from the treatment of discontinuities in the local coordinate systems of offset components.

A *global coordinate* system, in which surfaces or rays are expressed in a single Cartesian coordinate system, was used to specify the positions and tilts of each component in the MEMS-Demo 1.5 test system. This type of coordinate mapping was advantageous for this setup for two main reasons.

First, using global coordinates, individual components could be tilted or laterally displaced without altering the position or optical axes of the remaining components in the system. This is an obvious requirement for the investigation of component misalignment tolerances.

Secondly, global coordinates allow the lateral positions and angular tilts of large numbers of surfaces to be referenced to a single surface. Thus, if a surface is tilted or decentered, all those surfaces referenced to it experience the same misalignment. This largely simplified the repetitive process of displacing various components during the analysis of the misalignment tolerances, as only a single surface displacement was necessary. This is discussed in further detail in section 4.3. Table 6 in Appendix I shows a screen capture detailing the properties of the decentered surfaces used to implement the MEMS-Demo 1.5 system.

The subsequent sections describe the characteristics of the 5 modules used to construct the MEMS-Demo 1.5 system.

4.2.2 TX Module

The TX module was constructed assuming that both the OE chip and microlens array could be precision-aligned during the assembly process. As shown in Table 5 in Appendix I, it was specified by surfaces *Object* through *4*, and consisted of a single VCSEL, an air gap of 44μm, a silica substrate of thickness 300μm, and a circular refractive microlens of diameter 125μm with a focal length of 250μm in air – as outlined in section 2.1.1, describing the Demo 1.5 setup.

The highly divergent 850nm VCSEL beam was specified by determining the object numerical aperture of the source. Given an M^2 full-divergence angle of 20° and an M^2 factor of approximately 1.93, this results in a Gaussian beam full-divergence angle of,

$$\theta_{Gaussian} = \frac{\theta_{M^2}}{M^2} = 10.36^{o} \tag{12}$$

As specified in the Code V environment, the object numerical aperture, NA_{object}, is given by equation (13),

$$NA_{object} = n \cdot \sin\left(\frac{\theta_{Gaussian}}{2}\right)[rad] \tag{13}$$

where n is the index of refraction of the material through which the beam propagates. Given an air gap of 44μm, a refractive index in air of $n = 1$, the resulting object numerical aperture was determined to be $NA_{object} \approx 0.0902$rad.

The microlens array was implemented using two optical surfaces – *STOP(2)* and *3* . The stop surface, labeled *'Substrate'*, consisted of the 300μm-thick fused-silica microlens substrate. This was represented by a 300μm-thick glass slab, denoted *'silica'* in Table 5, with a refractive index, $n_{fusedSi} = 1.45268$, and square clear and edge apertures of side-length 125μm.

It must be noted that in the Code V environment, a clear aperture represents the light-gathering aperture of a component, whereas an edge aperture specifies the overall physical dimensions of the component. Evidently, these dimensions need not be coincident. However, for the purpose of this project, the clear and edge apertures were identical. From this point forward, the optical aperture of a component refers to both clear and edge apertures.

The collimating circular refractive microlens of focal length 250μm was specified using surface *3*, a plano-convex thin lens of index, $n_{fusedSi}$, with a circular aperture of 125μm, and a radius of curvature, R_2, given by equation (14), the formula for the focal length of a thin lens,

$$\frac{1}{f} = (n_{lens} - 1)\left(\frac{1}{R_1} - \frac{1}{R_2}\right) \tag{14}$$

Using this expression, the radius of curvature of the microlens was found to be $R_2 \approx$-0.11317mm. This value was further optimized using ray tracing simulations to $R_2 =$ -0.1145, in order to give a better representation of the collimated beam at the output of the microlens. Figure 37 shows the propagation of a Gaussian beam through the TX module.

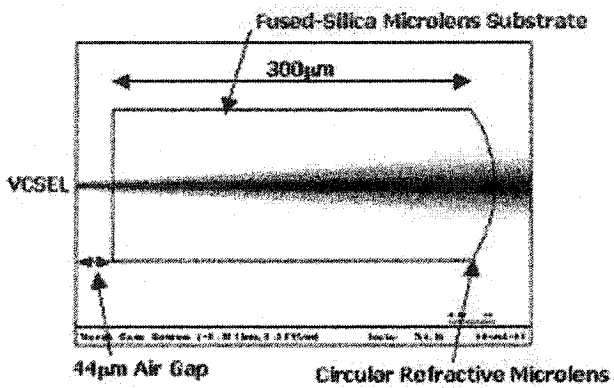

Figure 37 - Propagation of Gaussian Beam through TX module

4.2.3 MEMS Micro-mirrors

The MEMS micro-mirror structures were specified by surfaces *6*, denoted *'MEMS 1'*, and surface *13*, labeled *'MEMS 2'*. As shown in Figure 38, the micro-mirrors were positioned such that they intercepted the beams from the first minilens located vertically off-center in the minilens array.

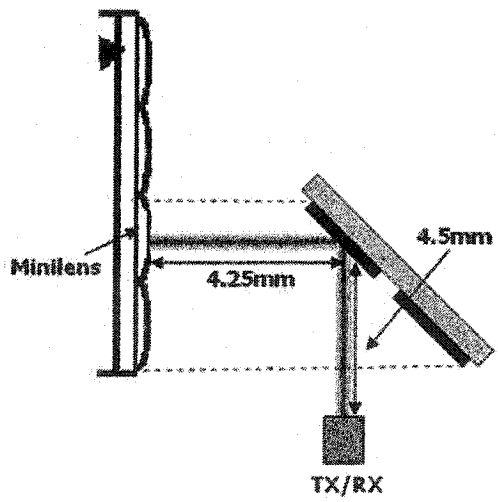

Figure 38 – Position of MEMS Micro-mirrors

Oriented at the required 45° angle to the optical axis, the mirrors were located at distances of $f_{mini}/2 = 4.25$mm and $(f_{mini}/2 + f_{micro}) = 4.5$mm from the minilens module, and TX and RX modules, respectively. These distances were representative of the distances required for the telecentric system used in the Demo 1.5 optical relay design.

Three implementations of the MEMS-Demo 1.5 system were simulated. Each employed micro-mirrors with differing characteristics.

The first, shown in Figure 39(a), used square, perfectly reflective mirrors with side lengths equal to 663μm – equivalent dimensions to the fabricated MEMS designs described in section 3.2.2.1. From this point forward, this implementation will be referred to as the practical MEMS-Demo 1.5 setup.

As discussed in section 3.2.3.1, in order to solve the problem of beam clipping at the mirror apertures, a second implementation utilized rectangular mirrors of dimensions 750μm by 1060μm, and reflectivities of 100% [Figure 39(b)]. From this point forward, this will be referred to as the ideal MEMS-Demo 1.5 setup.

The last set of simulations investigated the effect of mirror curvature on the throughput of the static system models of the previous two MEMS implementations [Figure 39(c)].

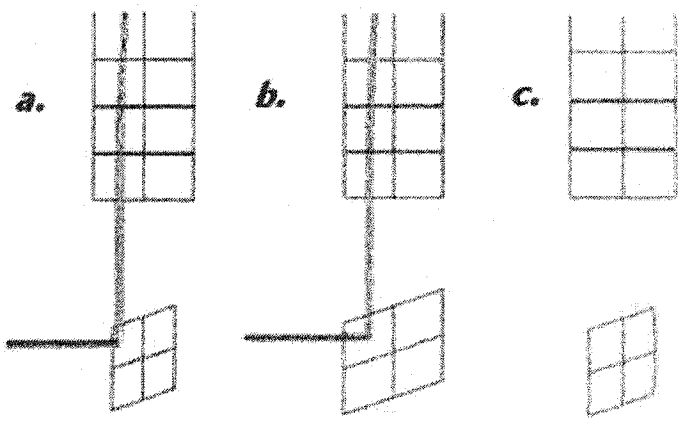

Figure 39 - Three Code V MEMS Micro-mirror Implementations
a. 663-μm-square MEMS mirrors, b. Ideal rectangular Micro-mirrors, c. Concave Mirror Surface

These simulations and their results are discussed in depth in sections 4.3 and 4.4.

4.2.4 Minilens Module

The minilens module was constructed assuming that the diffractive minilens arrays and the BK7 glass spacer were precision aligned during the assembly process. Represented by 6 optical surfaces, *7* through *12*, in the Code V environment, the minilens module consisted of a pair of diffractive minilenses and fused-silica substrates, separated by a BK7 glass spacer.

The 256-level diffractive Fresnel minilenses were treated as simple plano-convex lenses using the SWEATT model. The SWEATT model states that a thin holographic or diffractive optical element can be represented by a simple lens with a refractive index approaching infinity, and near-zero curvature and thickness [25]. Assuming negligible lens thickness, a high refractive index, n_{SWEATT}, and selecting a desired focal length for the lens, f, the required radius of curvature of the lens, R_1, can be determined accordingly from equation (14). Given a focal length of f = 8.5mm in air, and assigning a refractive index, $n_{lens} = n_{SWEATT}$ = 1,000,000, the minilenses at either end of the relay block were represented by surfaces *7*, and *11* and *12*, labeled *'Thin Fresnel 1'* and *'Thin Fresnel 2'* (Table 5), using plano-convex thin lenses of thickness 1μm, square optical apertures with a side length equal to 750μm, and radii of curvature, $R_{1,\ mini1}$ = 8499991.5mm and $R_{1,\ mini2}$ = -8499991.5mm, respectively.

The fused-silica minilens substrates were represented by surfaces *8* and *10*, labeled *'Mini Subs 1'* and *'Mini Subs 2'*, respectively, by 1mm-thick slabs of glass of index, $n_{fusedSi}$ = 1.45268, with 750μm-square optical apertures.

The last component of the minilens module was the BK7 glass spacer, surface *9*, positioned between the two diffractive minilenses and silica substrates. The optical aperture of the spacer was specified identical to the aperture of a single minilens element, and the thickness of the spacer was selected such that each minilenses were separated by a distance equivalent to twice the minilens focal length in air, $2f_{mini}$. However, as the

beam propagates in both the fused-silica and BK7 glass, the actual optical path length is longer, and is given by equation (15),

$$2f_{actual,\min i} = 2f_{\min i} \cdot n_{eff} \tag{15}$$

where n_{eff} is the effective index of the substrate-spacer structure as seen by a beam at a wavelength of 850nm. As the thickness of the spacer is large in comparison with the thickness of the substrates, the effective index may be reasonably approximated by the index of BK7 glass at a wavelength of 850nm, $n_{eff} = n_{bk7,\ 850nm} = 1.507$. This resulting substrate-spacer structure was assigned a thickness, t_{BK7}, given by the equation (16),

$$t_{BK7} = \left(2f_{\min i} \cdot n_{bk7,850nm}\right) - 2t_{substrate} \approx 23.619mm \tag{16}$$

Figure 40 shows the Code V schematic of the Minilens module.

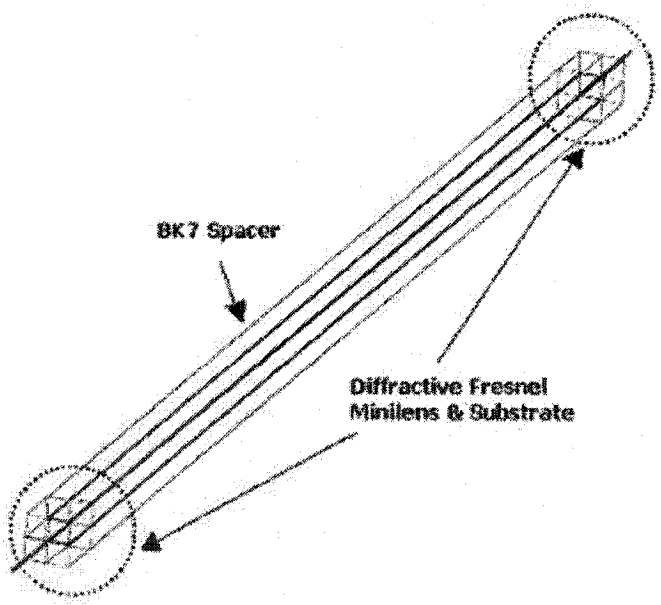

Figure 40 - Code V Schematic of Minilens Module

In order to facilitate simple misalignment of the minilens module, the lateral position and tilt of surface *7*, *'Thin Fresnel 1'*, was globally referenced to the object surface (VCSEL), a fixed component (Table 5). The remaining 5 surfaces comprising the minilens module were then referenced to surface *7*. As a result, any changes in the tilt or position of surface *7* caused corresponding changes in the remaining surfaces of the minilens module, leaving the rest of the system undisturbed.

4.2.5 RX Module

The RX module was constructed under similar assumptions used to model the assembly of the TX module. As shown in Table 5, the RX module, positioned at a distance of 4.235mm from the second micro-mirror, was represented by 5 optical surfaces, *14* through *18*, in the Code V environment. A plano-convex microlens, surface *15*, labeled *'Micro 2'*, with a circular optical aperture 125μm in diameter and a radius of curvature R_{micro} = 0.1145mm was attached to 300-μm slab of silica glass of index $n_{fusedSi}$. A 44-μm air-gap separated the microlens substrate from a square detector, with a side length of 50μm, at the image surface. In order to obtain accurate clipping results at the image surface, a dummy surface, surface *17*, labeled *'Dummy Image'*, was positioned coincident with the image surface with an optical aperture of 50μm-square, representative of the actual aperture of a detector on the OE-VLSI chip.

Figure 41 shows a Code V schematic of the RX module.

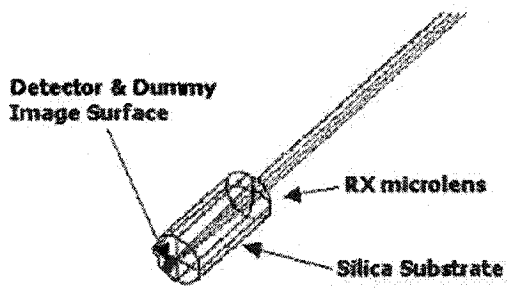

Figure 41 - Code V Schematic of RX module

Figure 42 shows a Code V schematic of the overall implemented MEMS Demo 1.5 system.

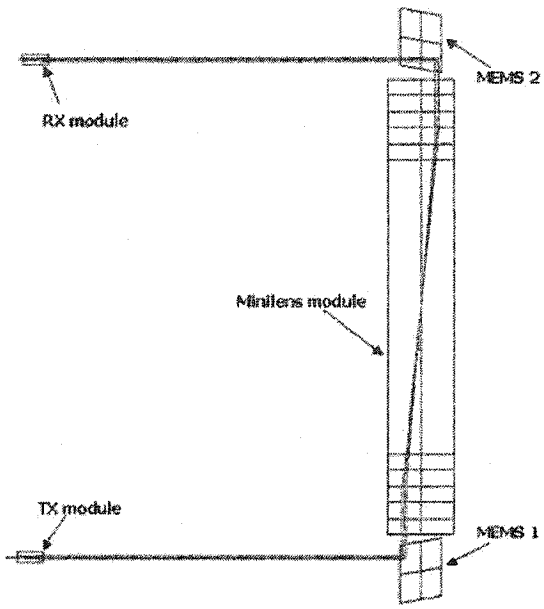

Figure 42 – Code V Setup of MEMS-Demo 1.5 FSOI

4.3 Misalignment Simulations

This section discusses the misalignment analyses performed for the test versions of both the practical and ideal MEMS-Demo 1.5 FSOI implementations, describing in detail the method, simulations, and the corresponding results.

4.3.1 Process - Determining Misalignment Tolerances

In order to accurately reflect those elements that would be mutually aligned in a practical laboratory setup, the 5 main modules described in the preceding section were further classified into 4 *misalignment modules*. Shown in Figure 43, the resulting 4 misalignment modules will be referred from this point forward as the transmitter (TX) module, the Minilens module, the MEMS-Minilens module, and the receiver (RX) module.

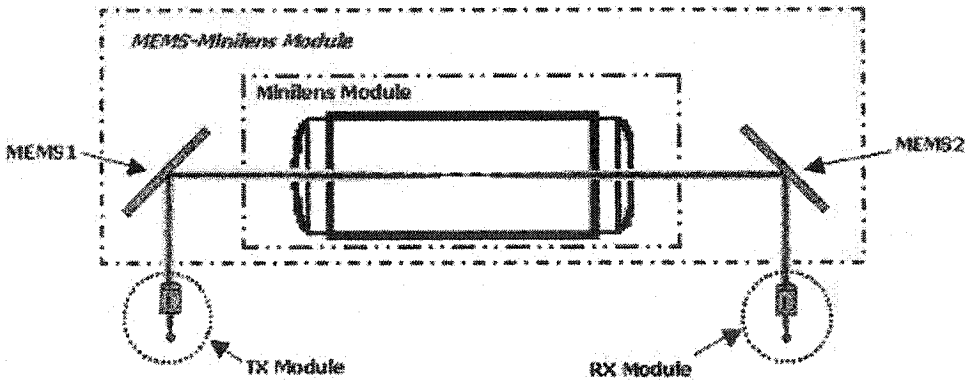

Figure 43 - MEMS-Demo 1.5 Misalignment Modules

Misalignment analysis was performed by displacing a single module, while leaving the rest of the system undisturbed. Modular displacement was accomplished using global coordinate referencing and a technique employing dummy optical surfaces. Using diffractive Gaussian beam propagation simulations, the system throughput, in the form of the normalized fraction of energy incident on the detector surface, was then calculated and plotted as a function of component misalignment. Command-based scripts were written to systematically perform the necessary misalignment and calculate the resulting system throughput. The details of the above elements of the simulation process are described in the subsequent sections.

4.3.2 Redundant Optical Surfaces – Module Misalignment

In Code V, redundant optical surfaces, known as dummy surfaces, are invaluable for implementing various tilt and positional configurations between components in an optical system. In this system, 4 additional surfaces, numbered *1*, *4*, *5*, and *14*, were created as misalignment surfaces to help facilitate angular tilt and lateral misalignment measurements for the aforementioned 5 misalignment modules.

Surface *1*, labeled *'Dummy Substrate'*, and surface *4*, denoted *'Dummy TX'*, were used to effectively tilt and laterally displace the TX module. As is shown in Table 6 in Appendix I, using the appropriate global coordinate reference surface assignments for the surfaces in the TX module, angular tilts of surface *1* resulted in tilting of the microlens and substrate structures, while leaving the rest of the system undisturbed. This, coupled with

changes in the angle of the VCSEL beam, effectively simulated angular tilt misalignments in the TX module. Similarly, by inducing changes in the lateral position of surface 4, the lateral position of all successive components in the system altered accordingly, effectively simulating a lateral misalignment of the TX module with respect to the rest of the system.

Surface *5*, *'Dummy MEMS-MINI'*, was used to effectively misalign the *MEMS-Minilens* module. By referencing the two mirror surfaces and the minilens module global reference surface, *'Thin Fresnel 1'*, to surface *5*, all three optical elements could be moved in both angular and lateral fashions as a single unit, leaving the rest of the system undisturbed.

In the RX module, an additional dummy surface, surface *14*, was inserted and using global coordinates was referenced to surface *4*, 'Dummy TX2'. The remaining surfaces for the RX module were then referenced to surface *14*. In a similar fashion to all other dummy surfaces, by tilting or displacing surface *14*, the lateral position or tilt of all other surfaces in the RX module change accordingly, without affecting the position of components in the rest of the system.

4.3.3 Diffractive Beam Propagation Simulations (BPR)

The Code V diffraction-based beam propagation tool traces a beam through an optical system, and, using diffraction propagation techniques in conjunction with geometrical ray tracing, determines the normalized intensity or phase of a beam at selected optical surfaces [26]. The user can specify the characteristics of the input beam in a variety of ways, including the traditional Gaussian beam profile. BPR simulations, unlike the standard Gaussian-beam propagation tool offered by Code V, take into account Fresnel reflections, as well as beam clipping and diffraction at optical apertures. This tool is therefore invaluable for characterizing the behavior of beams in free-space optical systems, such as the system under investigation. Despite this, the BPR simulation only propagates scalar field distributions, and therefore does not take into account the polarization state of the beam [26]. This beam characteristic, however, did not need to be

considered for the purpose of this project, as polarization effects are minimal in the optical components used to construct the FSOI under investigation.

4.3.4 *Misalignment Simulations – Code V Command-Based Scripts*

Macros written using the Code V prompting language were written to displace surfaces in the Code V environment, corresponding to the various misalignment modules. BPR simulations were then used to propagate a Gaussian beam through the system, and output the normalized fraction of energy of the beam incident at the detector to an external text file. Done in a systematic fashion for the lateral and angular tilt misalignments of all misalignment modules, plots of the system throughput versus module misalignment were obtained. The schematics shown in Figure 44 below illustrate examples of both lateral and angular tilt misalignments.

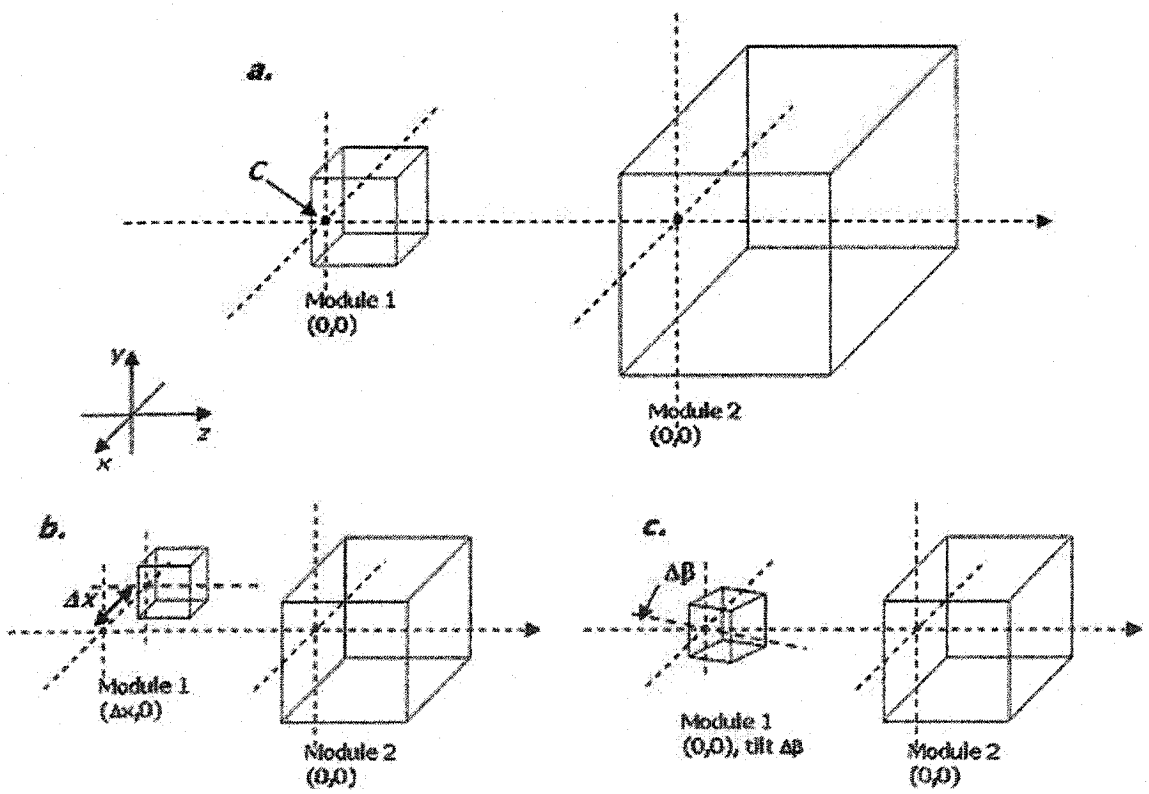

Figure 44 - Examples of Lateral & Angular Tilt Component Misalignments
a. Static Case, b. Lateral Misalignment, Δx, c. Angular Tilt Misalignment, $\Delta\beta$

It must be noted that the position and tilt of surfaces in the Code V environment are specified by lateral and angular decenters. From this point forward, both lateral and

angular misalignments will be referred to as changes to the lateral and angular tilt decenters of an optical surface, respectively.

As shown in Figure 44(b), lateral displacements involved changing the position of a module along the two axes perpendicular to the axis of propagation. Altering the *x*, *y*, or *z* decenters shifts a surface horizontally or vertically along the *x*, *y*, or *z*-axes, respectively.

Angular tilt misalignments, involved changing the angle between a module's two primary axes, and a third axis about a selected center point such that the resulting axis of propagation for the module changed accordingly [Figure 44(c)]. This is accomplished using the three Code V angular decenters – alpha, beta, and gamma. As shown in Figure 45(a) and (b), modifying alpha and beta decenters, tilt an optical surface about its center point in the *y*-*z* and *x*-*z* planes, thereby rotating the module about the *x*-axis and *y*-axis, respectively. Changing the third angular coordinate, gamma, tilts a surface about its center point in the *x*-*y* plane, rotating the module about the *z*-axis [Figure 45(c)]. These terms will be referred to repeatedly in the subsequent sections.

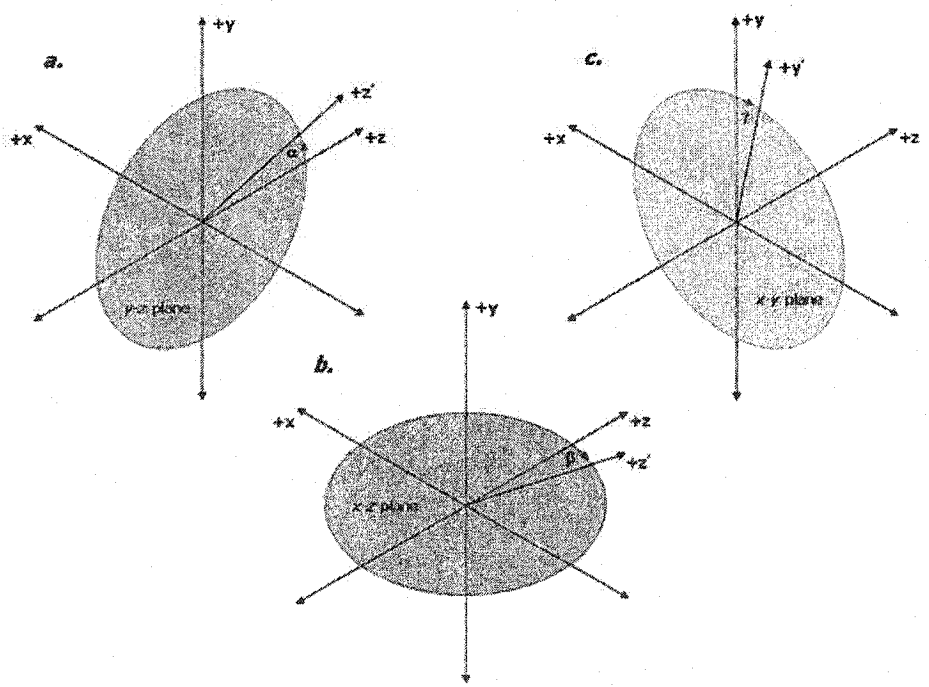

Figure 45 - Code V Angular Tilt Decenters
a. Positive Alpha Tilt, b. Positive Beta Tilt, c. Positive Gamma Tilt

The above process was completed for both static and dynamic cases of the practical and ideal micro-mirror implementations of the MEMS-Demo 1.5 system. In the static case, the micro-mirrors remained fixed, whereas the dynamic case involved tilting the mirrors incrementally from 0 to $\pm 0.1725^{o}$, such that maximum throughput for each case of module misalignment was observed. To accomplish the mirror deflection, text files were used to input the appropriate mirror tilts into the Code V system. *Matlab* cubic interpolation functions were used to interpret the resulting simulation data, and obtain smooth plots of the system throughput versus module misalignment. These plots were then used to obtain the appropriate misalignment tolerances for both the uncorrected and corrected systems.

The following section details the above simulations and the observed results.

4.3.5 Misalignment Simulations – Results

In this section, the lateral and angular module misalignment simulations for both the practical and ideal MEMS are described, highlighting the improvement in misalignment tolerances offered by the use of MEMS micro-mirrors as beam steering components in the Demo 1.5 FSOI. For all simulations, system tolerances to misalignment were deemed as the maximum misalignment for no greater than a 5% decrease in the maximum system throughput.

It must be noted that Table 5 and Table 6 in Appendix I will be referred to repeatedly in the following section, when describing the surfaces used to perform the necessary lateral and angular tilt misalignments of the modules.

4.3.5.1 TX Module

This section describes the lateral and angular tilt misalignment tolerances for the TX module.

a) Lateral Misalignment

For both practical and ideal micro-mirror system implementations, lateral misalignment of the TX module was accomplished by systematically changing the x and y decenters of surface *4*, labeled *'Dummy TX2'*, in the range 0 to 100μm, in steps of 10μm. Using global coordinates, all other surfaces in the system were referenced to surface 4. By inducing lateral misalignments in surface 4, the rest of the system shifted with respect to the TX module, effectively creating TX module misalignment. Figure 46 shows the resulting misalignment curves.

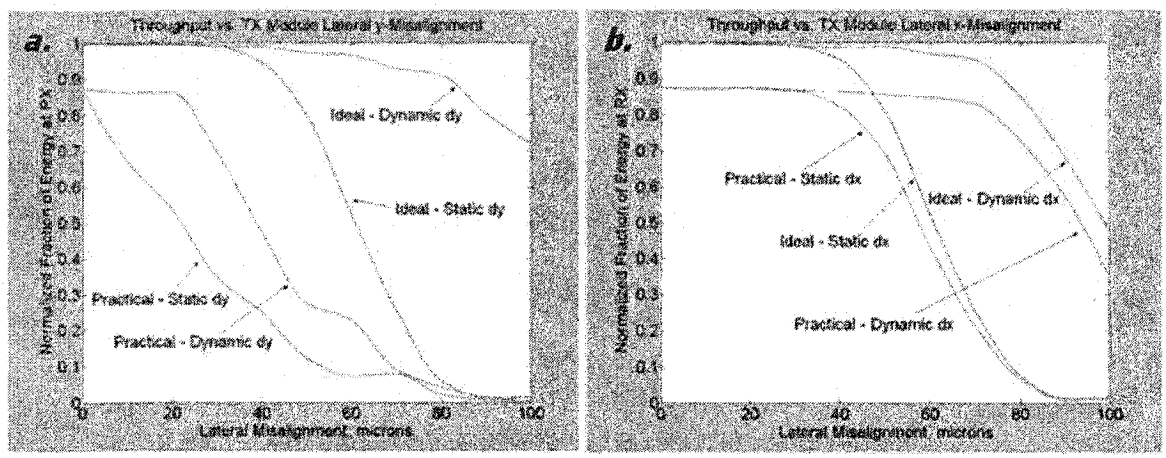

Figure 46 – Throughput vs. TX Module Lateral Misalignment
a. Lateral y-axis misalignment, b. Lateral x-axis misalignment

For the practical MEMS setup, Figure 46(a) and (b) show for zero lateral misalignment, an overall throughput of approximately 87% was observed. As was predicted, losses for the static case were primarily as a result of beam clipping of the worst-case source at both MEMS micro-mirrors. In the practical implementation, smaller mirror dimensions and the 45° orientation of the mirrors in the y-z plane, caused a smaller mirror apparent optical aperture and therefore beam clipping. As shown in the curves in Figure 46(a), the practical system throughput dropped off linearly as y-misalignment increased, thereby indicating that the worst-case source was initially clipped by the y-aperture of both mirrors. Correction for this was obtained by deflecting the beam further back onto the aperture of the second mirror. Improvement is clearly visible, as the lateral y-misalignment tolerance increased by approximately 20μm, from 3μm to 23μm, in the static and dynamic cases, respectively.

The ideal rectangular MEMS implementation was created to alleviate the beam clipping performance issues of the smaller square MEMS mirrors. Figure 46(a) clearly shows that the ideal MEMS system has an overall throughput of approximately 99% in the case of perfect alignment. In this state, beam clipping was minimized, as the apparent optical aperture of the mirrors in both axes was equal to the optical aperture of the 750μm-square minilenses, resulting in a mirror fill factor of 1. Similar to the practical setup, the dynamic system showed an improvement of 31μm in the ideal *y*-misalignment tolerance, from 42μm to 73μm. Compared to the practical system this is a significant improvement in the lateral correction in the *y*-axis - an increase of 50μm, from approximately 23μm to 73μm.

As shown in Figure 46(b), in both practical and ideal MEMS setups, beam clipping did not occur in the *x*-aperture of the mirror surfaces. As a result, the lateral *x*-misalignment tolerances were comparatively equal. For both micro-mirror implementations, an improvement of 31μm was observed, from 41μm to 72μm in the static and dynamic systems, respectively.

It must be noted, however, that in the dynamic system a lower tolerances was observed for lateral *x*-misalignments than was for lateral *y*-misalignments in Figure 46(a). This can be explained from the fact that the maximum beam deflection angle in the *x*-axis is less than in the *y*-axis, and is related to the angular tilt of the mirror in the *y-z* plane, α.

Referring to Figure 19, from basic optics theory, a beam incident on a plane mirror at an angle θ in the *y-z* plane will reflect off the surface at the same angle. If the mirror is tilted at an angle, α, the beam will be deflected, in the *y-z* plane, from the original path by an angle equal to twice the mirror deflection, given by equation (17)

$$\varphi_y = 2 \cdot \alpha \tag{17}$$

Consider now a three-dimensional mirror oriented at an angle, θ, in the y-z plane [Figure 47(a)].

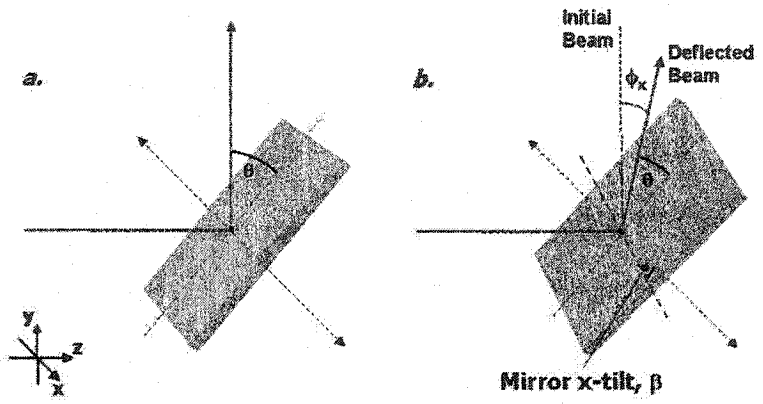

Figure 47 - Beam Deflection from Mirror Tilt in *x*-axis
a. Mirror at rest, b. Mirror tilt in *x*-axis.

If an angular tilt, β, is introduced in the *x*-*z* plane of the mirror, the beam is deflected both at an angle θ in the *y*-*z* plane, and at an angle ϕ_x in the *x*-*z* plane [Figure 47(b)]. The angle, ϕ_x, therefore, determines the theoretical lateral beam deflection possible from a micro-mirror tilt, β.

The relationship between θ, β, and ϕ_x can be determined using vector analysis, and is given by equation (18):

$$\phi_x = \arccos\left[\cos^2(\theta)\cos^2(\beta) + \sin^2(\theta)\right] \tag{18}$$

As is evident from the above equation, the angular beam deflection in the *x*-*z* plane due to a mirror tilt, β, is also dependent on the orientation of the mirror in the *y*-*z* plane, α. However, assuming only minimal deviations of θ in the *y*-*z* plane, $\theta \pm \alpha_{max}$, where $\alpha_{max} = 0.1725^\circ$ (as determined in section 3.2.2.1), the expression for the maximum theoretical beam deflection in the *x*-axis may be approximated by a mirror fixed at an angle, $\theta = 45^\circ$. Thus, equation (18) reduces to:

$$\phi_x = \arccos\left[\cos^2(\beta)\right] \tag{19}$$

As described in section 3.2.2.1, $\beta_{max} = \pm 0.1725^\circ$. Using equation (19), the approximate maximum lateral *x*-axis beam deflection angle is therefore $\phi_x \approx \pm 0.243^\circ = \pm 4.24$mrad. Comparatively, according to equation (17), the maximum lateral beam deflection angle in

the y-axis is $\phi_y = 2\alpha_{max} = 0.345^\circ$ =-6.02mrad. Both of these values were verified using Code V real ray-tracing simulations.

For the practical system, as was previously discussed, the smaller mirror aperture in the y-axis contributed to decreased dynamic misalignment correction when compared to lateral x-misalignments – thereby negating the above effect. However, in the ideal system, with equal apparent optical apertures in both axes, decreased correction for x-misalignments became apparent, as the curve for lateral x-misalignment for the TX module fell off prematurely [Figure 46(b)].

The following section describes the results of angular tilt misalignment of the TX module for both MEMS setups

b) *Angular Tilt Misalignment*

Angular tilt misalignment analyses for the TX module were accomplished by perturbing the alpha and beta decenters for the globally referenced surface *2*, labeled *'Substrate'*, as well as the position and angle of the VCSEL beam. The TX module was, therefore, effectively tilted at an angle about the center point of the microlens substrate. For both setups, the mirrors were systematically tilted in the range of ±2°, in steps of 0.4° were used to obtain the necessary misalignment curves. Figure 48 shows the resulting plots for both MEMS implementations.

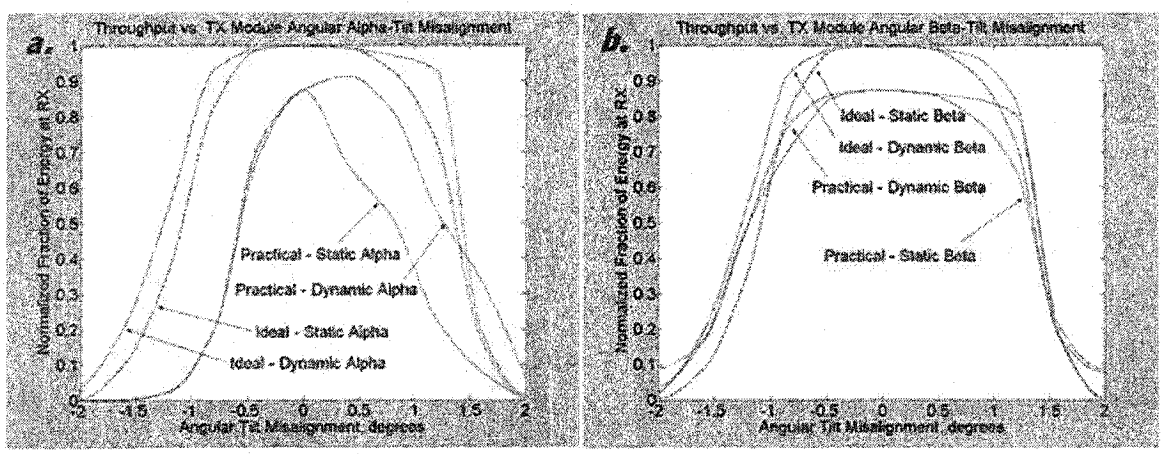

Figure 48 – Throughput vs. TX Module Angular Tilt Misalignment
a. Alpha-tilt misalignment, b. Beta-tilt misalignment

For the practical MEMS implementation, two major features of the curves in Figure 48(a) and (b) must be noted. First, the above curves are not symmetric about the central axis. This can be explained by the fact that the worst-case source was offset from the central axis of the rest of the system. Secondly, as was the case for lateral misalignment, the system performance for TX module alpha-tilt misalignment suffered considerably. As shown in Figure 48(a), the throughput dropped off sharply in both directions for the static system. For increasing negative alpha tilts of the TX module, the beam centroid was pushed closer to the edge of the mirror aperture, thereby causing beam clipping. Since the loss occurred at the first mirror, this effect was uncorrectable, as is illustrated in the dynamic alpha-tilt curve, resulting in a tolerance of -0.2° for negative alpha-tilt angular misalignments. Conversely, for positive alpha tilts, the drop was attributed to beam clipping at the minilens aperture. In this case, the TX module was tilted in such a way that although a larger fraction of the beam was incident on the mirror, the beam contacted the mirror at a shallower angle and therefore deflected to a point closer to the edge of the minilens aperture, inducing additional clipping losses. As is shown in the curve for the dynamic system, the latter effect was corrected for by using the first micro-mirror to compensate for the shallow reflection angle, deflecting the beam away from the edge of the minilens. Correspondingly, the dynamic system increased the positive alpha-tilt tolerances by approximately 0.785°, from 0.015° to 0.80°.

The ideal MEMS implementation again succeeded in improving the above tolerances. The curves in Figure 48(a) show a marked improvement in the alpha-tilt angular misalignment tolerances when compared to the practical system. For the static case, tolerances of -0.65° and 0.7° were observed when compared to -0.15° and 0.1° in the practical implementation. In the dynamic system, both negative and positive alpha-tilt tolerances increased by -0.2° and 0.35°, from -0.65° to -0.85° and 0.75 to 1.10°, respectively.

Figure 48(b) shows the resulting curves for beta-tilt misalignment of the TX module for both practical and ideal systems. As expected, the static beta-tilt misalignments for both

systems were coincident, as both systems had the same mirror x-aperture. Thus, static tolerances were measured to be -0.6° and 0.75°. Slight correction was observed in both dynamic setups. For the practical system, tolerances -0.7° and 1.15° were observed, improvements of -0.1° and 0.4°, for negative and positive beta-tilts, respectively. The ideal system showed similar corrective ability, with tolerances of -0.75° and 1.05°, improvements of -0.15° and 0.25°.

In both alpha and beta-tilt misalignments, it is clear that beam clipping at the mirror and minilens apertures was again the limiting factor for angular tilt misalignments. Although the mirrors were used to deflect the beam at an angle opposite to the angular misalignment of the TX module, this was not sufficient to improve the misalignment tolerances. Once the angles were sufficient to introduce clipping, the mirrors were unable to correct for the misalignment.

A summary of the TX module lateral and angular misalignment tolerances are presented at the end of this section.

4.3.5.2 RX Module

This section describes the lateral and angular tilt misalignment simulations and results for the RX module.

a) Lateral Misalignment

For both MEMS implementations, RX module lateral misalignment tolerances were determined by systematically displacing globally referenced surface *13* by a total 100μm in steps of 10μm, in both *x* and *y* axes. Figure 49 shows plots of throughput versus lateral RX misalignment for both practical and ideal MEMS setups.

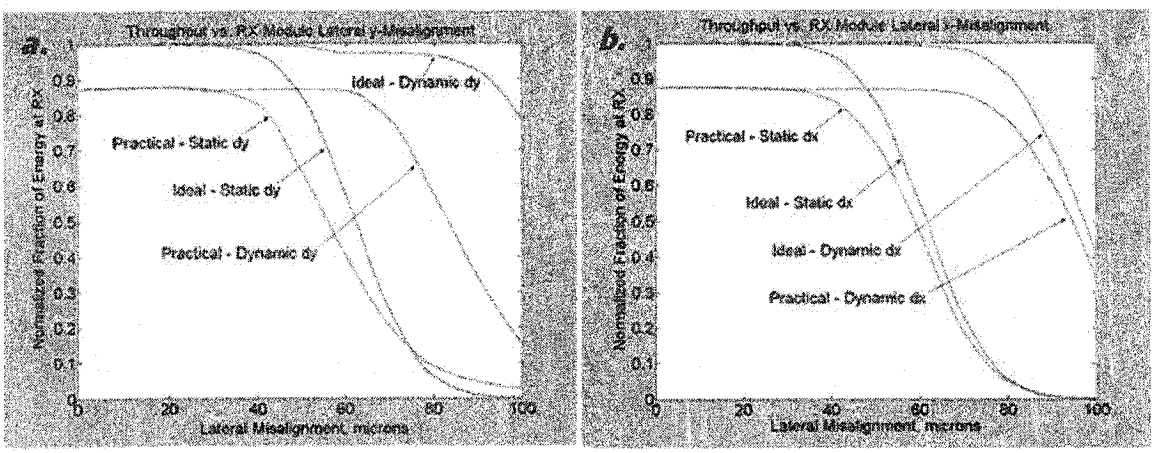

Figure 49 - Throughput vs. RX Module Lateral Misalignment
a. Lateral *y*-misalignment, b. Lateral *x*-misalignment

The above lateral misalignment curves for the RX module display a clear improvement in lateral tolerances resulting from the MEMS beam steering system.

Figure 49(a) shows the resulting plots for *y*-misalignment of the RX module for both MEMS setups. In both static implementations, the RX module did not suffer the same tolerance limitations due to the smaller aperture of the MEMS mirrors in the *y*-axis. This was attributed to the fact that the limiting factor for the misalignments in the RX module was beam clipping at the microlens aperture. Increasing lateral *y*-misalignment of the RX module created a vertical displacement of the beam center on the surface of the microlens. Given a microlens *y*-aperture of 125μm, a vertical beam displacement equal to one-half the microlens aperture, 62.5μm, resulted in 50% transmission. This is verified by both static curves in Figure 49(a).

Correction was achieved by actuating the mirrors in a complementary fashion such that the first mirror deflected the beam closer to the bottom edge of the second mirror, thereby resulting in the maximum achievable lateral beam deflection at the receiver. In the practical MEMS setup, the *y*-misalignment tolerance improved by approximately 27μm, from 41μm to 68μm. In the ideal system, however, an increase of 42μm was observed, from 41μm to 83μm. Discrepancies between these tolerances can be attributed to differences in mirror aperture size. For both dynamic implementations, when using

aforementioned misalignment correction method, beam clipping at the second micro-mirror apertures, instead of at the RX microlens aperture, ultimately limited the maximum permissible RX module misalignment. Correspondingly, the tolerances for the ideal system were comparatively larger, indicating an increased tolerance by approximately 15μm.

Conversely, as was the case for *x*-misalignment of the TX module, both practical and ideal MEMS setups exhibited similar tolerances to lateral misalignment in the *x*-axis. From the curves in Figure 49(b), in both cases tolerances improved by approximately 34μm, from 41 to 76μm in the static and dynamic implementations, respectively. As was the case for *y*-misalignment, these tolerances were ultimately limited by beam clipping at the *x*-aperture of the second micro-mirror. Additionally, as was observed in the TX module misalignment simulations, less correction in the *x*-axis resulted from the smaller maximum lateral beam deflection described in section 4.3.5.1.

b) Angular Tilt Misalignment

An analysis of the angular tilt misalignment tolerances for the RX module was accomplished in both MEMS implementations by systematically changing the alpha and beta decenters for global reference surface *13*. In doing so, the RX module was tilted about the center point of the microlens surface. Given a symmetric beam incident on the microlens, tilt misalignments ranging from 0° to 10°, in steps of 1°, were simulated. Figure 50 shows a schematic of the RX module tilted at $\alpha_{RX} = 5°$, and the misalignment curves for both practical and ideal MEMS implementations.

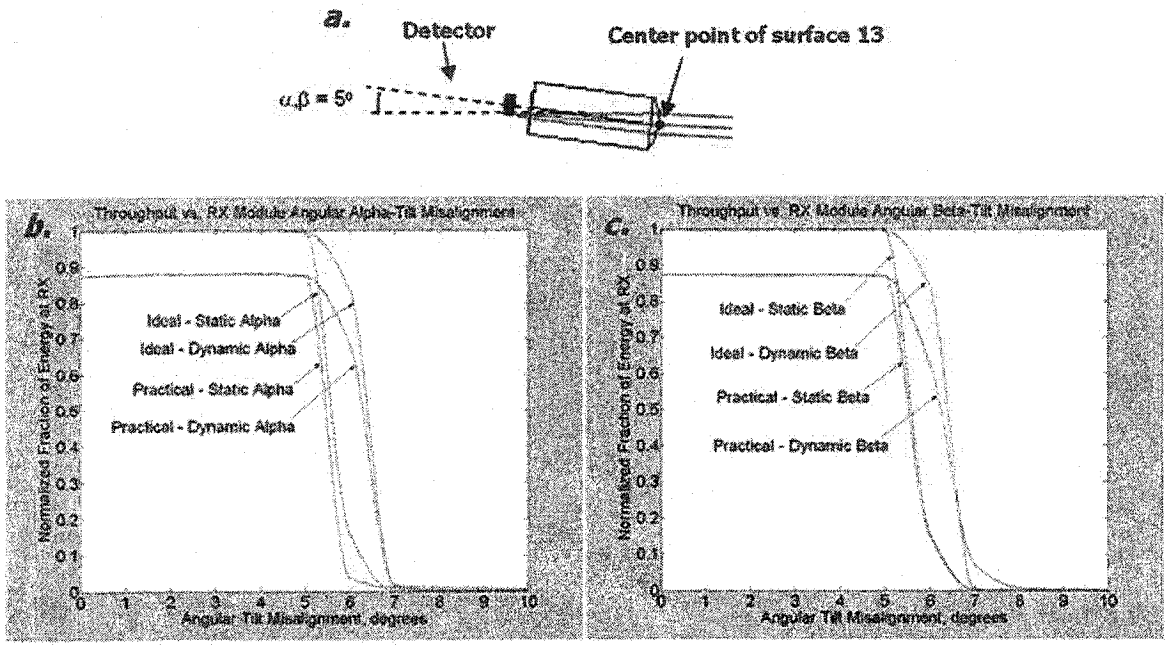

Figure 50 – RX Module Angular Tilt Misalignment
a. Schematic of angular tilt of RX module, b. Alpha-tilt misalignment, c. Beta-tilt misalignment

From Figure 50(b) and (c), it is clear that for both the practical and ideal MEMS setups, relatively no improvement was observed in the angular tilt tolerance of the RX module, between the static and dynamic cases. In both plots, alpha and beta-tilt misalignment tolerances increased ±0.25°, from approximately ±5.15° to ±5.4°. These improvements are minute in comparison to the 10° tilt range. This was attributed to an aberration at the RX microlens that could not be accommodated by lateral beam deflection using the micro-mirrors. As shown in Figure 50(a), as the RX module was tilted about the center point of the microlens surface, the position and angle of the 50μm-square detector surface, represented by the blue square, and the angles at which the marginal rays contacted the fast optical surface, changed accordingly. The chief ray, however, remained incident at the center point of the microlens. This resulted in a transverse focal aberration, causing the focal point of the beam at the image plane to be shifted vertically by a distance, Δh, given by equation (20),

$$\Delta h = f_{micro} \cdot \tan(\phi) \tag{20}$$

where ϕ is the angular tilt of the module and f_{micro} is the focal length of the microlens.

Increasing ϕ also increases Δh, resulting in abrupt beam clipping as the center of the beam reaches the edge of the detector surface. For example, according to equation (20), a tilt of $\phi = 5.71^{\circ}$ corresponds to a vertical shift, $\Delta h = 25\mu m$. Given a 50μm full-aperture width of the detector, the above 25μm shift translates into 50% clipping of the beam at the edge of the detector surface. This was observed and is verified in the plots in Figure 50. The mirrors were unable to correct for this aberration, as a beam deflected laterally off-axis on the microlens either underwent clipping at the microlens aperture or was refracted further off the detector surface.

A summary of the misalignment tolerances for the RX module is presented at the conclusion of this section.

4.3.5.3 Minilens Module

This section describes the lateral and angular tilt misalignment tolerances for the minilens module.

a) Lateral Misalignment

Lateral misalignment tolerances for the minilens module were determined by displacing the globally referenced surface *6* by a total of 50μm, in steps of 5μm, in both *x* and *z* axes. The *z*-axis, in this case, was equivalent to displacement in the *y*-axis for all other modules, due to the 90° orientation of the minilens module with respect to the rest of the system. Figure 51 shows the resulting misalignment curves for both MEMS implementations.

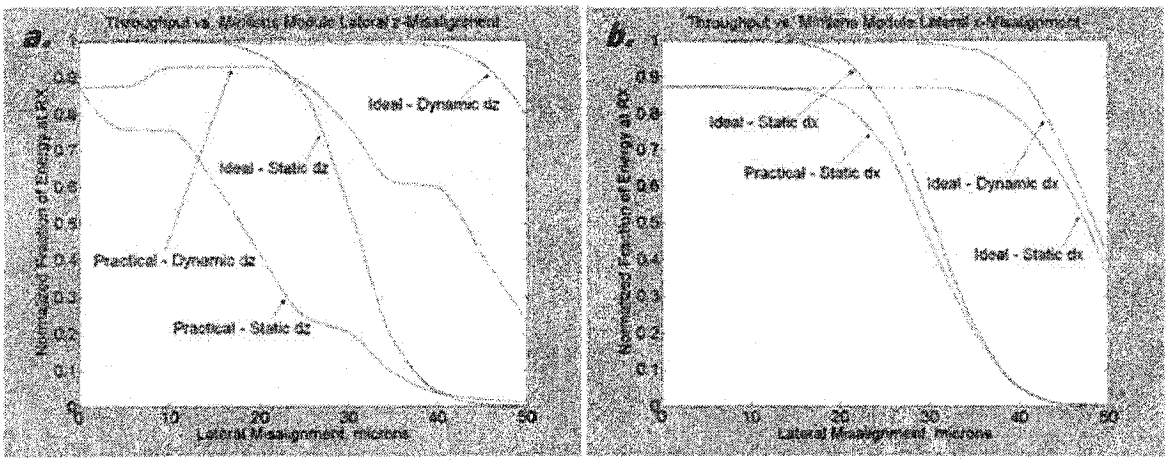

Figure 51 - Throughput vs. Minilens Module Lateral Misalignment
a. Lateral *z*-misalignment, b. Lateral *x*-misalignment

Figure 51(a) shows the curves for lateral misalignment of the minilens module in the *z*-axis. Again, it is evident that the static implementation of the practical MEMS setup suffered from misalignment laterally in the *y*-axis. As seen above, clipping at the smaller mirror apertures caused the throughput to drop off immediately for any magnitude of *z*-misalignment of the minilens module. Correction was achieved in a similar fashion the lateral TX module misalignment simulations. Using complementary mirror deflection angles, the beam was deflected initially by the first mirror to a point closer to the middle of the second mirror aperture, and secondly by the second mirror back onto the RX microlens aperture. In doing so, an improvement of approximately 25μm, from 2.5μm to 27.5μm, was observed in the dynamic system. The increased *y*-aperture of the mirrors in the ideal system compensated for this problem. The ideal system exhibited a static *z*-misalignment tolerance of approximately 21μm – significantly larger than the static tolerance for the practical MEMS setup. Additionally, the dynamic implementation resulted in an increase of 23μm, from 21μm to 44μm – an overall improvement of 16.5μm in the *z*-misalignment tolerance offered by the increased mirror aperture size of the ideal system.

Figure 51(b) shows the system throughput as a function of misalignment in the *x*-axis. As was the case for the TX and RX modules, no improvement was observed in the *x*-misalignment tolerance between the two MEMS setups. In the dynamic implementations

of both systems, tolerances were improved by 16.5μm, from approximately 21μm to 37.5μm.

It must again be noted that discrepancies between correctable distances in the x and y directions were as a result to the decreased beam deflection angle in the lateral x-axis. Both ideal and practical systems showed correction of 23μm and 25μm in the z-axis, respectively, while only exhibiting 16.5μm of correction in the x-axis.

Comparing the above lateral misalignment tolerances and correctable distances for the minilens module to those obtained for the TX and RX module, it can be seen that these values were observed to be roughly one-half of the misalignment tolerances of the TX and RX module. This can be explained by considering the behavior of a beam propagating through the minilens module.

Recall, the minilens module is constructed using a pair of minilens elements positioned in a 4-f telecentric configuration. From basic optics theory of a telecentric system, a beam contacting the minilens at an off-axis point *(x,y)*, undergoes negative unit magnification about the central optical axis, and exits the module at the point *(-x, -y)*. Now, if the optical axis of the minilens is laterally displaced along the x or y-axis by Δx or Δy, a total displacement of $2\Delta x$ or $2\Delta y$ occurs in the beam position after propagating through the minilens module. Thus, lateral misalignments of the minilens module are therefore equivalent to lateral misalignments of the TX and RX module scaled by a factor of 2. For example, as was seen above, minilens x-misalignment tolerance of approximately 37.5μm was simulated for the practical setup, whereas TX and RX module x-misalignment tolerances of 72μm, and 75μm were observed. The tolerances for y-misalignment in the practical setup do not adhere to this theory, as beam clipping at the mirror apertures distorted the results.

b) Angular Tilt Misalignment

Angular tilt tolerances the minilens module were determined by changing the alpha and beta decenters for the globally referenced surface *6*, thereby effectively tilting the

minilens module about the center point of the first minilens. For the practical MEMS setup alpha and beta tilts of magnitudes ±0.18° in steps of 0.036° were used, whereas for the ideal implementation tilts of ±0.20°, in steps of 0.04°, were simulated. Figure 52 shows the resulting misalignment plots.

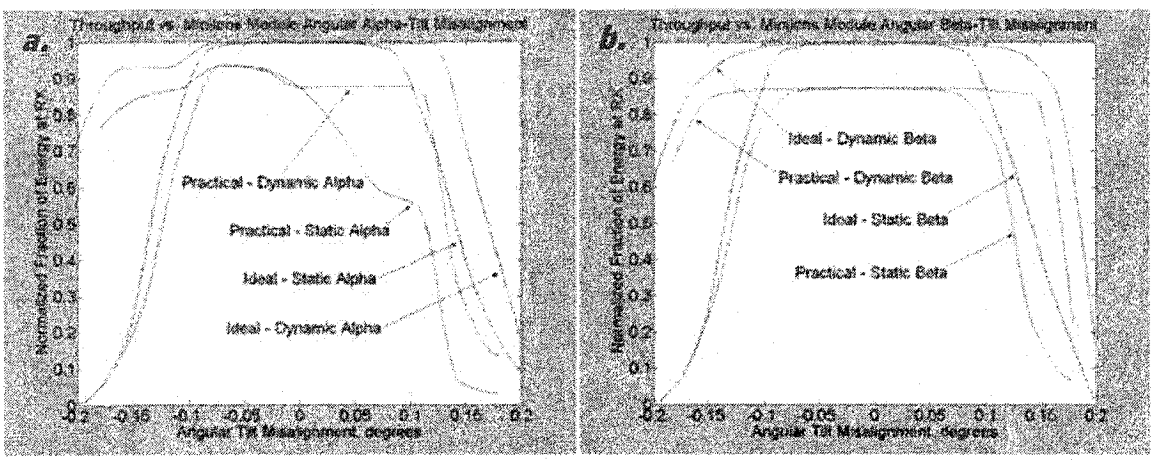

Figure 52 - Throughput vs. Minilens Module Angular Tilt Misalignment
a. Alpha-tilt misalignment, b. Beta-tilt misalignment

From Figure 52(a), a clear asymmetry exists in the curves for negative and positive angular alpha-tilts of the practical MEMS system. Negative angular tilts of the minilens caused the beam to be deflected to a point closer to the middle of the second mirror, thereby reducing clipping losses and causing the overall system throughput to increase. However, for increasingly negative alpha-tilts of the minilens module, increased clipping at the RX microlens aperture occurred, causing the throughput to drop off dramatically at a negative alpha-tilt tolerance of approximately -0.095°. Conversely, for positive angular tilts, beam clipping at the second mirror aperture was the limiting factor, as minilens tilts in this direction deflected the beam further off the edge of the second mirror. Correspondingly, the curve dropped off sharply, resulting in a positive alpha-tilt tolerance of 0.02° for the static system. Correction for both of the above effects was accomplished by deflecting the mirrors in such a way to oppose the lateral deflection of the beam on the second mirror. Correspondingly, alpha-tilt tolerances increased to -0.155° and 0.12° in the dynamic implementation, improvements of -0.06° and 0.1°.

A similar negative alpha-tilt tolerance of -0.095° was observed in the static implementation of the ideal setup, as clipping at the RX microlens aperture, again, was

the limiting factor. Conversely, the increased mirror *y*-aperture in the ideal system significantly improved the positive alpha-tilt tolerance for the static system, from 0.02° to 0.09°, an increase of 0.07°. Dynamic tolerances were found to be -0.105° and 0.135°, improvements of -0.01° and 0.045°. For positive alpha-tilts, only a minute improvement of 0.015° was observed between practical and ideal systems, corresponding to the increase in *y*-aperture of the mirrors. This is explained by the fact that although the micro-mirror apertures were increased and additional beam steering was used to try to correct for increased angular tilts, the minilens angular tolerances remained ultimately limited by clipping at the minilens aperture. Conversely, a reduced dynamic tolerance to negative alpha-tilt was observed in the ideal system – a value of -0.105°. Evidently, this result did not adhere well to theory, as both practical and ideal negative alpha-tilts were expected to be identical. Extensive further analysis was done to determine the nature of these discrepancies. Ultimately, it was determined that these inconsistencies were attributed to simulation error.

Figure 52(b) shows the results for beta-tilt misalignment of the minilens module for both MEMS implementations. As expected, both practical and ideal systems exhibited similar behavior for angular beta-tilts of the minilens module. As seen in Figure 52(b), in both systems, the dynamic implementations improved beta-tilt tolerances from approximately ±0.095° to ±0.155°, increases of ±0.06°.

A summary of the misalignment tolerances for the minilens module is presented at the end of this section.

4.3.5.4 MEMS-Minilens Module

In order to simulate the effect of mounting the two mirrors and the relay block to a customized optomechanic component in a practical laboratory setting, lateral and angular tilt misalignments of the MEMS-Minilens module were investigated.

a) Lateral Misalignment

Lateral misalignment of the MEMS-Minilens module was effectively simulated by varying the x and y-decenters for the globally referenced surface *5*, labeled *'Dummy MEMS-Mini'*. In the practical MEMS implementation, x and y-misalignments ranged from 0 to 50μm, in steps of 5μm, whereas for the ideal setup, displacements ranged from 0 to 50μm, in steps of 5μm, in the x-axis, and 0 to 175μm, in steps of 17.5μm, in the y-axis. Reasons for the difference in the ranges of y-misalignments between the two implementations will become evident later. Misalignments of the module along the optical z-axis were considered impractical tolerances given the large Rayleigh range of the collimated beam exiting the TX module, when compared to the propagation distances under investigation. Figure 53 shows the resulting misalignment curves for both the practical and ideal MEMS setups.

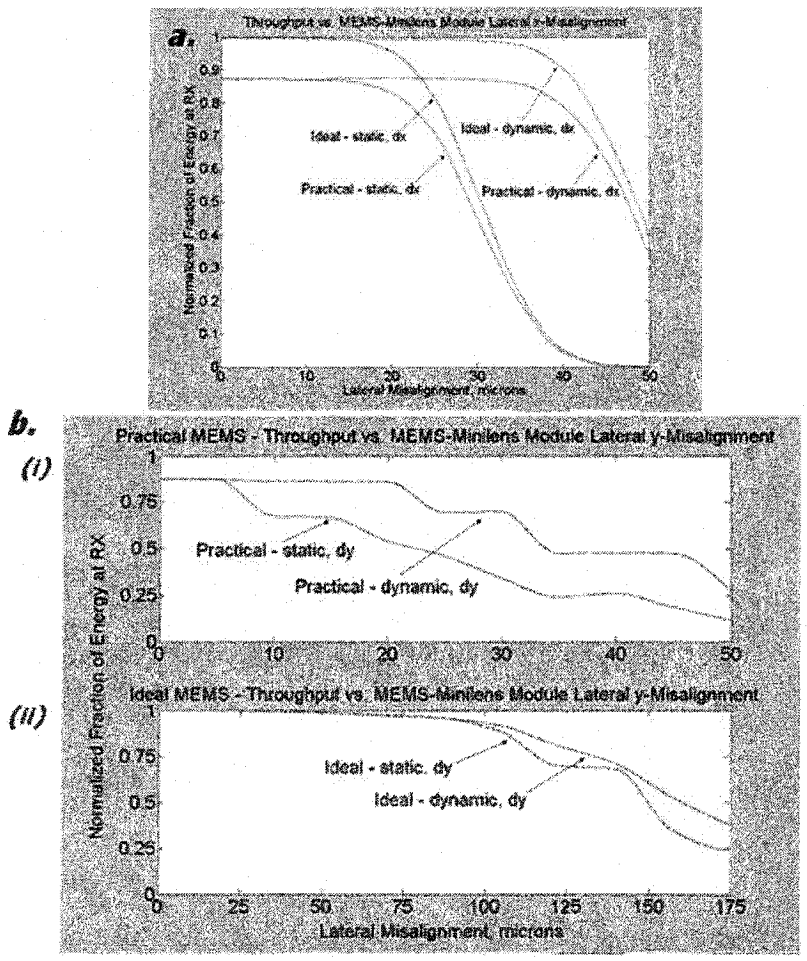

Figure 53 - Throughput vs. MEMS-Minilens Module Lateral Misalignment
a. Lateral x-misalignment, b. Lateral y-Misalignment

For both MEMS implementations, Figure 53(a) indicates similar x-misalignment behavior for the MEMS-Minilens module, as was shown in Figure 52(a) for the minilens module. In the latter case, the position of the central optical axis of the minilens module was the determining factor for the final position of the beam at the detector surface. Consequently, similar throughput characteristics were expected. In both systems, the mirror deflection used in the dynamic system improved the x-misalignment tolerance by approximately 16.5μm, from 21μm to 37.5μm.

Figure 53(b) shows the curves for lateral y-misalignment of the MEMS-Minilens module. As expected, the limiting factor for the practical MEMS implementation was beam clipping at the first mirror y-aperture – illustrated in curve Figure 53[b-(i)]. Similar effects were described in the results for the TX and Minilens module [Figure 46(a) and Figure 52(a)]. For the static system, a linear decrease in the throughput, from its initial value of 87%, was observed, as the beam was simply shifted further off y-aperture of the first mirror for additional y-misalignments. Correction was accomplished by deflecting the beam further back onto the second mirror aperture using the first mirror. The dynamic curve indicates a y-misalignment tolerance of 22μm, an improvement of approximately 15μm, from 7μm in the static system. However, clipping at RX mirror aperture, ultimately arrested the maximum corrective deflection. This is more evident in Figure 53[b-(ii)], showing lateral y-misalignments of the MEMS-Minilens module in the ideal MEMS implementation. With the increase in mirror aperture, the tolerance to misalignment correspondingly increased from approximately 22μm in the practical MEMS setup to 99μm in the ideal MEMS setup. However, in the ideal setup, virtually no correction was visible from static to dynamic cases, as clipping at both the mirror and minilens aperture had the effect of negating the effects of the beam steering.

b) Angular Tilt Misalignment

For the previous three modules, based on the position and global reference surfaces used to characterize the modules, alpha and beta-tilts were the only practical angular tilt tolerances. However, for the MEMS-Minilens module, all three angular tilt decenters, alpha, beta and gamma, were considered to be practical misalignments. Thus, angular tilt

tolerances for the MEMS-Minilens module were determined by changing the three tilt decenters for the globally referenced surface *5*, thereby effectively tilting the module about the center point of the first micro-mirror surface. Gamma-tilts of ±0.15°, in steps of 0.03°, beta-tilts of ±0.5°, in steps of 0.1°, and alpha-tilts of -2° to 0°, in steps of 0.2° were used to obtain the required misalignment curves. Figure 54 shows the plots for both MEMS setups.

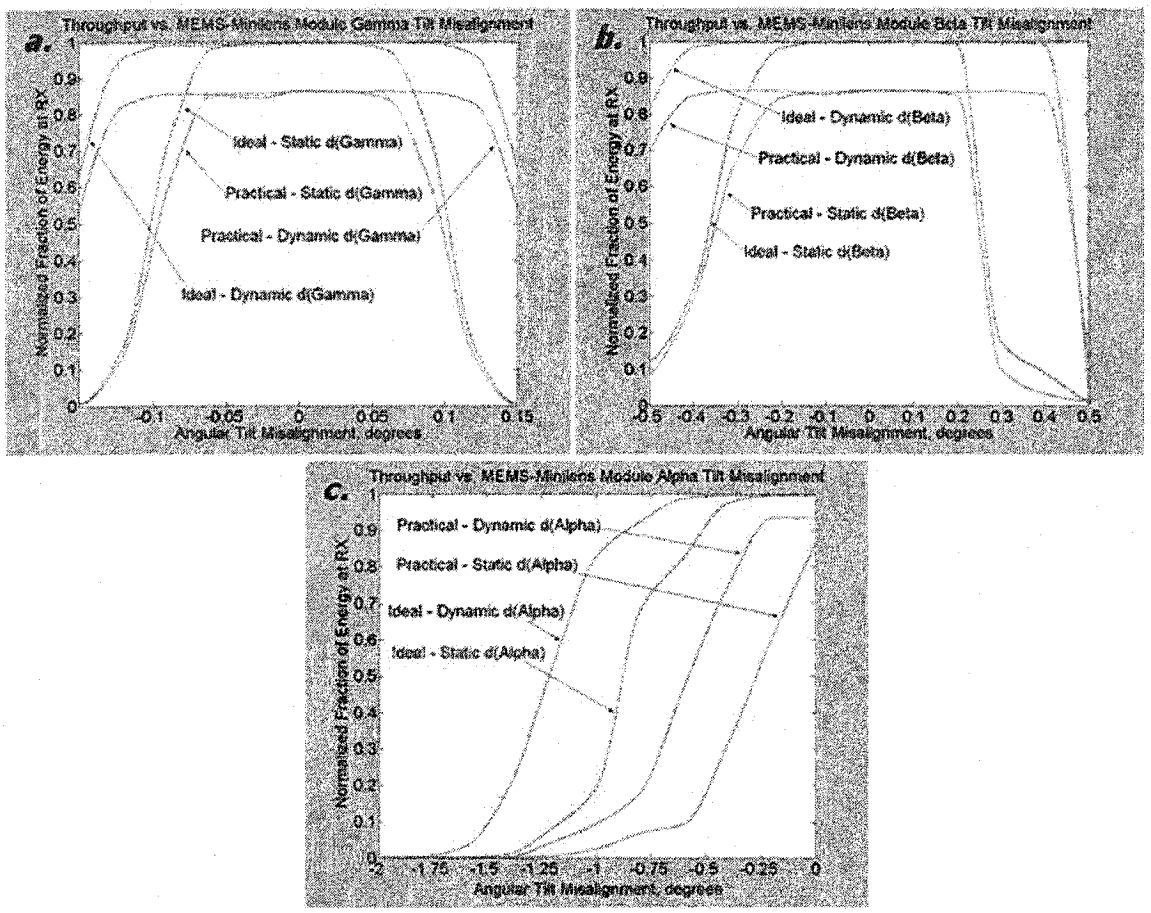

Figure 54 - Throughput vs. MEMS-Minilens Module Angular Tilt Misalignment
a. Gamma-tilt misalignment, b. Beta-tilt misalignment, c. Alpha-tilt misalignment

Figure 54(a) shows the resulting curves for gamma misalignments for both practical and ideal systems. Despite the improvement in mirror aperture size in the ideal system, both practical and ideal MEMS implementations exhibit identical gamma tilt tolerances in both the uncorrected and corrected systems. As well, the curves are symmetric about the axis. Both of these characteristics indicate that for gamma angular tilt misalignments of the MEMS-Minilens module, the limiting performance factor was beam clipping at the

aperture of the RX microlens. As gamma tilts were increased, the worst-case beam was offset radially along the circular microlens aperture by a distance, Δr, on the aperture of the microlens given by equation (21),

$$\Delta r = z_{prop} \cdot \tan(\gamma) \tag{21}$$

where z_{prop} is the propagation distance from the first to the second MEMS mirror. Given z_{prop} = 34.8485mm, for 50% of the beam to lie off the microlens aperture with a diameter of 125μm, equation (21) gives required gamma tilt of approximately ±0.102°. This is verified in the curves in Figure 54(a). Correction for gamma misalignment was accomplished by changing, accordingly, the mirror beta-tilts, laterally shifting the beam back onto the microlens aperture. As expected, significant improvements were evident in the dynamic forms of both implementations. Static system gamma-tilt tolerances were determined to be ±0.07°, while the introduction of dynamic MEMS beam steering allowed a 60% improvement, ±0.055°, to ±0.125°.

Figure 54(b) shows the resulting curves for beta-tilt misalignment. Similar to the case of gamma-tilt misalignment above, both practical and ideal MEMS implementation exhibited similar uncorrected and corrected MEMS-Minilens module beta-tilt misalignment tolerances. As was the case for beta-tilt misalignment of the minilens module, the curves in Figure 54(b) were found to be asymmetric in nature. For negative beta-tilts of the MEMS-Minilens module, the system throughput dropped off less dramatically than in the case of positive beta-tilt misalignments. In the former case, the beams were deflected laterally away from the edge of the second mirror aperture, as was observed for gamma-tilt misalignments, and as a result, clipping at the RX microlens aperture was the major performance limiting factor. Conversely, positive beta-tilt misalignments caused the beam to not only be deflected laterally only the x-aperture of the RX microlens, but also closer to the edge of the second mirror aperture. Thus, the combination of clipping at both the mirror and RX microlens, contributed to the sharp drop in the system throughput for the positive beta-tilts. Correction for the above effects was achieved by changing the beta-tilts of the mirrors, thereby steering the beam further back onto the appropriate apertures. As seen in the dynamic curves in Figure 54(b), the

static system beta-tilt tolerances were determined to be ±0.225°, while the introduction of dynamic MEMS beam steering allowed an increase of ±0.2°, to ± 0.425°. It must be noted that gamma-tilt tolerances were found to be significantly less than those for beta-tilt misalignments. This can be attributed to the fact that the propagation distance for gamma tilts, z_{prop}, is comparatively much larger and therefore small gamma deflections result in large lateral deflections at the RX microlens aperture.

Figure 54(c) shows the curves for MEMS-Minilens module alpha-tilt misalignment for both MEMS setups. As was seen in the case of angular and lateral misalignments of all other modules, the major limiting factor for the performance of the practical MEMS setup under alpha-tilt misalignments of the MEMS-Minilens module was beam clipping at the y-aperture of the micro-mirrors. As alpha tilt tolerances were increased, the angle of incidence at the first micromirror altered accordingly, effectively deflecting the beam closer to the edge of the aperture of the second micro-mirror. A corresponding drop in throughput was then observed due to beam clipping at the second mirror aperture. This beam deflection was accommodated by tilting both mirrors in complementary fashion at an angles opposite to the tilt misalignment, and thus, for small angles, effectively canceling out the beam deflection for small angles. At large angles, however, beam clipping at the mirror apertures was the dominant effect. Correspondingly, alpha-tilt misalignment tolerances were found to be significantly less, at -0.05° and -0.375° for uncorrected and corrected cases, respectively, than in the ideal MEMS setup. In the latter implementation, an increased fill-factor minimized beam clipping at the mirror apertures, and instead, for large negative alpha-tilts the beam was deflected at angles such that clipping at the aperture of the minilens module became the limiting factor. As expected, in the static case, an alpha-tilt of approximately -0.9° translated into 50% clipping at the minilens aperture [Figure 54(c)]. Tolerances were therefore found to be 0.475° and 0.75°, improvements of 0.425 and 0.375° from the static and dynamic cases of the practical setup, respectively.

It must be noted that positive alpha-tilt misalignments resulted in unexplainable anomalies in the Code V beam propagation results and abnormal software terminations.

Extensive further analysis was done to determine the nature of these discrepancies. Ultimately, it was determined that these inconsistencies were attributed to simulation error. As a result, only the above negative alpha-tilt misalignments were considered and positive misalignments were assumed to be similar in nature.

4.3.6 Summary – Misalignment Tolerances

4.3.6.1 Lateral Misalignment

Table 2 shows a summary of the static and dynamic misalignment tolerances achieved from the simulations of both MEMS implementations. Recall these tolerances represent the required component misalignment for a 5% drop in the power incident on the detector surface.

Table 2 - Summary of Lateral Misalignment Tolerances
a. Lateral – *dy*, b. Lateral – *dx*

a.	Lateral, dy (μm)						
	Practical MEMS			Ideal MEMS			Practical vs. Ideal
Module	Static	Dynamic	*Improvement*	Static	Dynamic	*Improvement*	*Dynamic Improvement*
TX	3	23	*20 (x 7.7)*	42	73	*31(x 1.73)*	*50 μm (x 3.17)*
RX	41	68	*27 (x 1.65)*	41	83	*42 (x 2.02)*	*15 μm (x 1.22)*
Minilens	2.5	27.5	*25 (x 11)*	21	44	*23 (x 2.09)*	*16.5 μm (x 1.6)*
MEMS-Minilens	7	22	*15 (x 3.14)*	99	99	—	*77 μm (x 4.5)*

b.	Lateral, dx (μm)						
	Practical MEMS			Ideal MEMS			Practical vs. Ideal
Module	Static	Dynamic	*Improvement*	Static	Dynamic	*Improvement*	*Dynamic Improvement*
TX	41	72	*31 (x 1.75)*	41	72	*31 (x 1.75)*	—
RX	41	76	*35 (x 1.85)*	41	76	*35 (x 1.85)*	—
Minilens	21	37.5	*16.5 (x 1.78)*	21	37.5	*16.5 (x 1.78)*	—
MEMS-Minilens	21	37.5	*16.5 (x 1.78)*	21	37.5	*16.5 (x 1.78)*	—

From the above simulations, it is evident that the MEMS micro-mirrors were largely successful in improving the lateral misalignment tolerances for all modules in both the practical and ideal MEMS-Demo 1.5 implementations. As is illustrated in Table 2(a), in both setups the dynamic beam steering system allowed for improvements in *y*-misalignment tolerances by scale factors greater than 1.65 to as large as 11, over the static systems. Additionally, as shown in Table 2(b), the MEMS micro-mirrors allowed for a consistent improvement in *x*-misalignment tolerances by scale factors greater than 1.78, when compared to the static system.

Comparing the dynamic tolerances offered by the practical and ideal MEMS systems, the former setup was found to be significantly more sensitive to lateral y-misalignment [Table 2(a)]. By introducing a mirror fill factor of 100% in the latter implementation, clipping at the mirror apertures was minimized, and, as expected, dynamic tolerances to component y-misalignment in the improved by scale factors as little as 1.22, in the case of the RX module, to as large as 3.17 and 4.5, as was observed for the TX and MEMS-Minilens modules.

As both setups employed micro-mirrors with identical x-apertures, no improvements were observed in the dynamic x-misalignment tolerances between the two MEMS micro-mirror implementations. As described in section 4.3.5.1, in both implementations the 45° orientation of the micro-mirrors caused a reduction in the maximum possible lateral beam deflection angle in the x-axis. Correspondingly, x-misalignment tolerances were found to be slightly less than those for misalignment in the y-axis. This effect is illustrated in Table 2(b), and is most visible in the dynamic x-misalignment tolerances obtained in the ideal implementation. In the practical setup, however, unequal apparent optical apertures in the x and y-axes distorted the results, therefore masking this effect.

4.3.6.2 Angular Tilt Misalignment

Table 3 below shows a summary of the static and dynamic angular tilt misalignment tolerances achieved for both practical and ideal MEMS setups.

Table 3 – Summary of Angular Tilt Misalignment Tolerances
a. Alpha-tilt misalignment, b. Beta-tilt misalignment, c. Gamma-tilt misalignment

a.

	Angular, dα (degrees)						
	Practical MEMS			Ideal MEMS			Practical vs. Ideal
Module	Static	Dynamic	*Improvement*	Static	Dynamic	*Improvement*	*Dynamic Improvement*
TX	-0.2, +0.015	-0.2, +0.8	*0, +0.785*	-0.65, +0.75	-0.85, +1.10	*-0.2, +0.35*	*-0.65, +0.3*
RX	± 5.15	± 5.4	*± 0.25*	± 5.15	± 5.4	*± 0.25*	—
Minilens	-0.095, +0.02	-0.155, +0.12	*-0.06, +0.1*	-0.095, +0.09	-0.105, +0.135	*-0.01, +0.045*	*(+0.05), 0.015*
MEMS-Minilens	± 0.05	± 0.375	*± 0.325*	± 0.475	± 0.75	*± 0.275*	*± 0.375*

b.

	Angular, dβ (degrees)						
	Practical MEMS			Ideal MEMS			Practical vs. Ideal
Module	Static	Dynamic	*Improvement*	Static	Dynamic	*Improvement*	*Dynamic Improvement*
TX	-0.6, +0.75	-0.7, +1.15	*-0.1, +0.4*	-0.65, +0.75	-0.75, +1.05	*-0.15, +0.25*	*-0.05, (-0.1)*
RX	± 5.15	± 5.4	*± 0.25*	± 5.15	± 5.4	*± 0.25*	—
Minilens	± 0.095	± 0.155	*± 0.06*	± 0.095	± 0.155	*± 0.06*	—
MEMS-Minilens	± 0.225	± 0.425	*± 0.2*	± 0.225	± 0.425	*± 0.2*	—

c.

	Angular, dγ (degrees)						
	Practical MEMS			Ideal MEMS			Practical vs. Ideal
Module	Static	Dynamic	*Improvement*	Static	Dynamic	*Improvement*	*Dynamic Improvement*
MEMS-Minilens	± 0.07	± 0.125	*± 0.055*	± 0.07	± 0.125	*± 0.055*	—

Table 3(a), (b), and (c) illustrate the increase in angular tilt tolerances offered by the dynamic beam steering system in both MEMS implementations. Notable improvements by as much as 0.785°, 0.4°, and 0.055° in alpha, beta, and gamma-tilt misalignments, respectively, were observed between the static and dynamic systems.

Table 3(a) highlights the improvement in dynamic alpha-tilt angular tolerances offered by the ideal MEMS implementation. Increases as great as 0.65° for negative alpha-tilts of the TX module and as little as 0.375° for positive alpha-tilts of the MEMS-minilens module were observed – all significant improvements resulting from the MEMS micro-mirror beam steering system.

As shown in Table 3(b), in both setups, similar tolerances for all modules, excluding the TX module, were found for beta and gamma-tilt misalignment, as no modifications were made to the mirror dimensions in the *x*-axis. As previously discussed, discrepancies between the predicted and observed results for the TX module were as a result of repetitive, unexplainable anomalies in the Code V simulations.

Table 3(c) also shows that no improvements were observed between the two MEMS setups for gamma-tilt misalignment of the MEMS-minilens module. Again, this can be explained by the identical *x*-aperture of the micro-mirrors in the two implementations.

It should be noted that in both MEMS implementations, the dynamic systems were unable to make any substantial correction for angular misalignment of the RX module. As previously discussed, this was attributed to the fact that angular tilts of the RX module resulted in transverse spherical aberrations of the beam at the detector surface. This effect could not be corrected for using the lateral beam steering offered by the MEMS micro-mirrors.

4.3.7 Comparison – Demo 1.5 vs. MEMS-Demo 1.5 FSOIs

Table 4 compares the minimum dynamic misalignment tolerances obtained from the above simulations of MEMS Demo 1.5 system to those obtained in the misalignment analysis of the original Demo 1.5 system.

Table 4 – Misalignment Tolerances: Demo 1.5 FSOI vs. MEMS-Demo 1.5 FSOIs

Misaligned Components	Demo 1.5	*Practical MEMS*	*Ideal MEMS*
VCSEL-microlens	± 25 μm	± 23 μm (-8%)	± 72 μm (x 2.88)
Relay	± 12.5 μm	± 27.5 μm (x 2.2)	± 37.5 μm (x 3)
Relay Θx, Θy	± 0.05 degrees	± 0.12 degrees (x 2.4)	± 0.105 degrees (x 2.1)

For the most part, significant improvements were observed in the misalignment tolerances between the Demo 1.5 and the two MEMS Demo 1.5 systems described above. In the practical MEMS setup, the TX module minimum lateral misalignment tolerance was found to be 8% less than the tolerance found for the Demo 1.5 system, as a result of the smaller apparent optical aperture of the practical square micro-mirrors. However, this was corrected for in the ideal MEMS implementation, as the minimum tolerance was found to be 50μm greater than the Demo 1.5 system. Similar increases were observed for misalignment in the relay block, as both practical and ideal systems improved the minimum tolerance by scale factors of 2.2 and 3 times the value documented for the original system. The above table also highlights a marked improvement in the angular tolerance of the relay block was observed when compared to the original Demo 1.5 system. Simulation results for both practical and ideal MEMS systems showed that the minimum angular misalignment tolerance for the relay block was increased by scale factors of 2.4 and 2.1, respectively.

Misalignment correction in the Demo 1.5 system has been illustrated via Code V numerical simulations. Clearly, if incorporated into the Demo 1.5 system, MEMS micro-mirrors would allow for significant improvement in virtually all of the relevant misalignment tolerances.

4.4 Mirror Curvature Simulations

A third simulation was performed to examine the effect of MEMS micro-mirror surface sag, and therefore mirror surface curvature, on the performance of both the practical and ideal MEMS setups. For the sake of simplicity, these simulations were performed on static, and therefore perfectly aligned, systems. As was outlined in section 3.2.3.2, for a source incident at a point *(x,y)* off-axis relative to the rest of the system, two major effects result from introducing a curvature in the mirror surfaces – defocusing and lateral beam deflection. In the interest of reducing simulation complexity, two separate simulations were conducted, with the purpose of decoupling these aberrations. Tolerances for the mirror radii of curvature were determined uniquely for each case, highlighting not only the maximum tolerable mirror sag, but also the limiting performance factor.

4.4.1 Curvature Simulation I - Defocusing Effect

In the first simulation, the effect of defocusing for an on-axis source was examined. In both MEMS setups, command-based scripts were used to systematically record the system throughput for decreases in the radii of curvature of from 30mm to 2mm, in steps of 2mm. Cubic interpolation functions with resolutions of 0.001 were used to represent the simulation data. Figure 55(a) shows resulting curves for both setups.

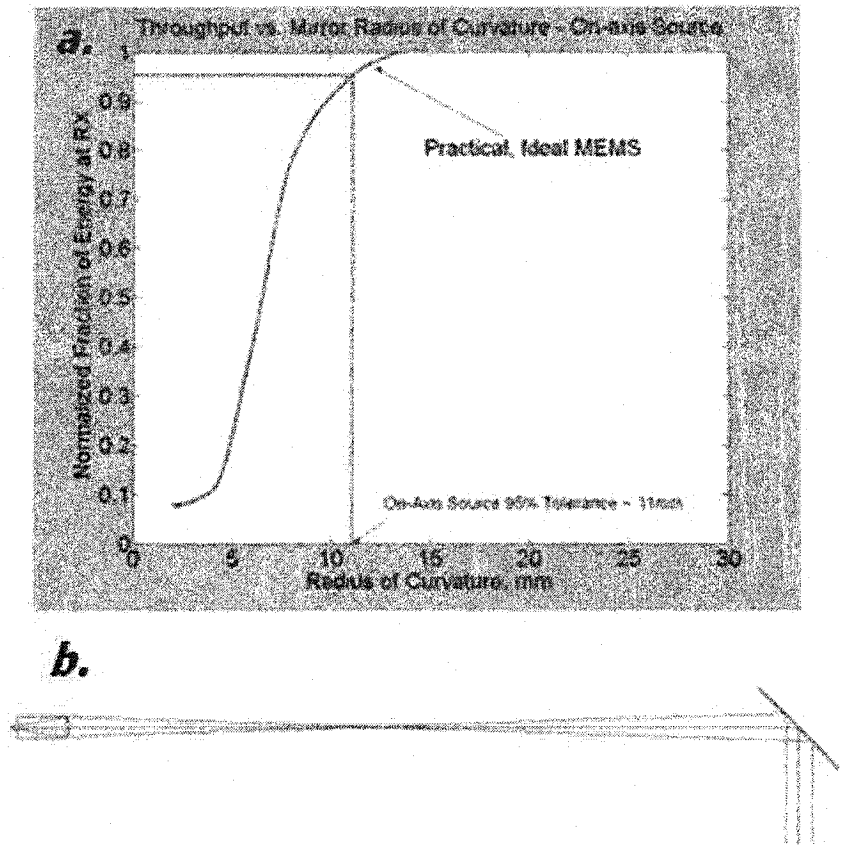

Figure 55 - Defocusing Effect: Throughput vs. Mirror Radius of Curvature

As expected, the curves for both setups were coincident, as clipping at the mirror apertures was not a factor for the on-axis source. Correspondingly, unclipped overall throughputs of approximately 99% were observed in both the practical and ideal MEMS setups. As the radii of curvature of both mirrors were decreased, defocusing of the beam introduced, first, clipping at the microlens aperture, followed by clipping at both the microlens and minilens apertures. As a result, the curves for the practical and ideal systems were coincident, exhibiting 95% mirror curvature tolerances of approximately 11mm [Figure 55(a)].

4.4.2 Curvature Simulation II – Lateral Beam Deflection

A second simulation examined the effect of varying mirror radius of curvature on the angular, and therefore lateral, deflection of an off-axis beam. The off-axis beam in this case was the worst-case source in a cluster. In order to do so, the angular deflection of a beam incident on a curved mirror surface was approximated by tilting perfectly flat

mirrors at the appropriate angles. Referring to the diagram in Figure 56, by taking the mirror tilt as equivalent to the tangent to the curved mirror surface at the point of incidence, *I*, of the off-axis beam, an approximation for the radius of curvature of the mirror, R_{MEMS}, as a function of the mirror tilt, $\Delta\alpha$, can be determined.

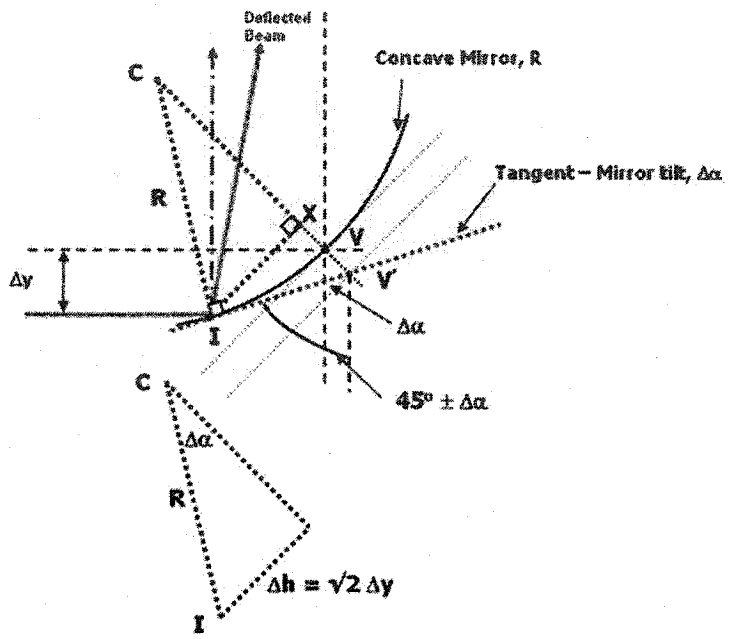

Figure 56 - Approximation of Curved Mirror Surface using Tilted Mirrors

Using simple geometry, this is given by equation (22),

$$R_{MEMS} \cong \frac{\sqrt{2} \cdot \Delta y}{\sin(\Delta\alpha)} \tag{22}$$

where, Δy, is the position of the off-axis beam on the y-axis of the mirror surface. The same equation applies to angular deflection in the lateral x-axis.

Command-based scripts were used to deflect the mirrors at the required angles and record the system throughput. Using the above equation and the resulting simulation data, plots of the throughput as a function of mirror tilt and approximate radii of curvature of the mirrors were obtained. Figure 57(a) and (b) show the curves for both systems.

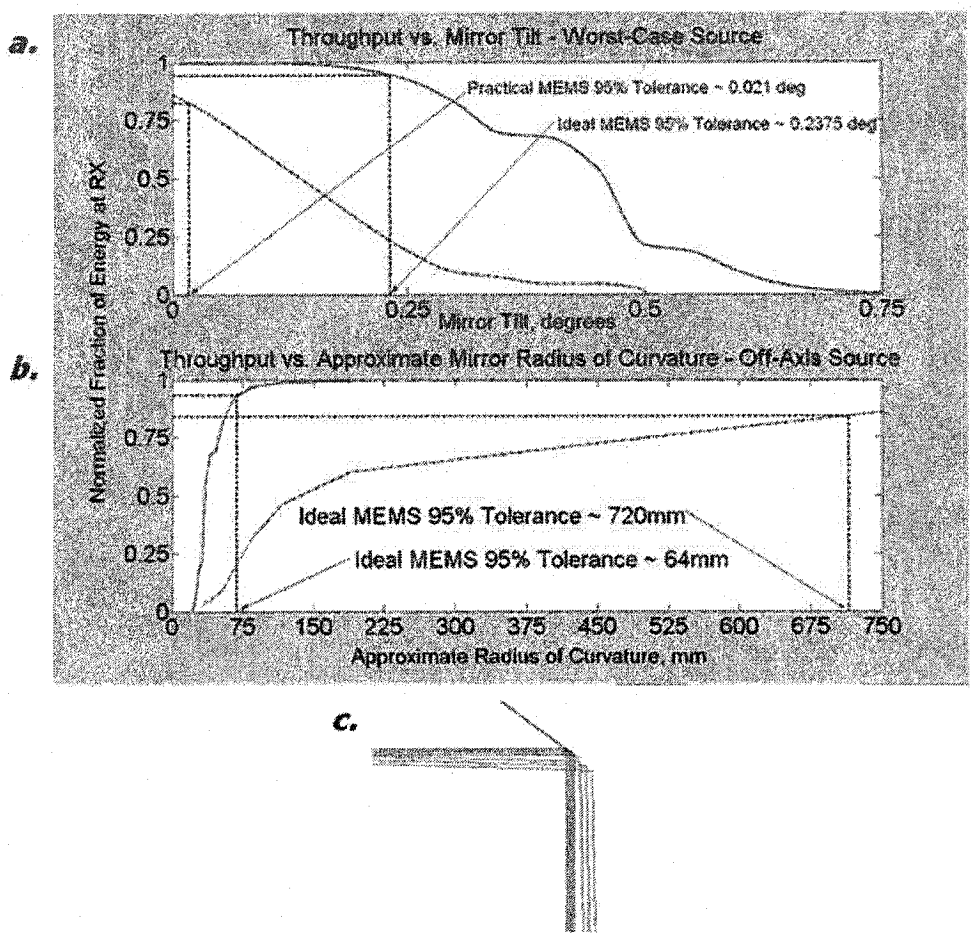

Figure 57 –Throughput vs. Approximate Mirror Radius of Curvature
a. Throughput vs. Mirror Tilt,
b. Throughput vs. Approximate Radius of Curvature,
c. Practical MEMS setup – Beam Clipping at 2nd mirror aperture

In the case of the practical MEMS setup, for small mirror tilts, the throughput dropped immediately, as a result of beam clipping at the second mirror aperture. As the curvature of the first mirror was decreased, the beam centroid deflected laterally towards the edge of the second mirror-aperture, inducing clipping [Figure 57(c)]. This resulted in a mirror tilt tolerance of approximately 0.021^{o} at both mirrors. Using the above formula, this translates into an approximate mirror radius of curvature minimum tolerance of 720mm [Figure 57(b)].

Conversely, the increased mirror apertures in the ideal system allow for a significant increase in the mirror tilt tolerance. Ultimately, beam clipping at the second minilens aperture was the limiting factor, causing the throughput to drop significantly at mirror tilts

of approximately 0.02375°. This translated into an approximate minimum mirror radius of curvature of 64mm [Figure 57(b)], a significant improvement from the practical system.

4.4.3 Analysis – Minimum Tolerable Radii of Curvature

For the defocusing effect, the minimum tolerable radius of curvature in both cases was found to be approximately 11mm. Comparing this to the above tolerances, 720mm and 64mm for practical and ideal systems, respectively, it is clear that the lateral beam deflection resulting from a change in the radii of curvature of the mirrors is the dominant effect of changing the radius of curvature of the micro-mirrors. Minimum tolerances for radii of curvature of the MEMS mirrors were therefore 720mm and 64mm, for the practical and ideal MEMS implementations, respectively.

As was discussed in section 3.2.3.2, assuming a spherical surface profile for the sagging mirror surface, the above minimum mirror curvatures were used to determine an approximation for maximum acceptable level of surface sag. This was done using the simple geometry of a chord of length, *2d*, on a circle of radius, *R*. As shown in Figure 58, the chord half-length, *d*, is equal to one-half the side length of the mirror surface and the height of the chord, *h*, is equal to the surface sag for the center of the mirror surface.

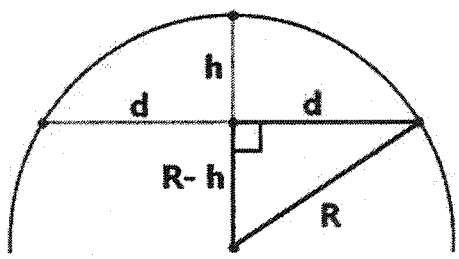

Figure 58 - Determining Radius of a Circle from a Chord

From a right angle triangle with side lengths *(R-h)*, *d*, and *r*, the radius of the circle as a function of *d* and *h* is given by the equation (23):

$$R = \frac{d^2 + h^2}{2h} \tag{23}$$

Figure 59 is a plot of the radius of curvature of the micro-mirror surface as a function of the surface sag, *h*, for both MEMS setups. One-half side lengths of 331.5μm and

530.33μm were used for the practical and ideal MEMS mirrors, respectively, corresponding to the largest lateral dimension of each mirror surface.

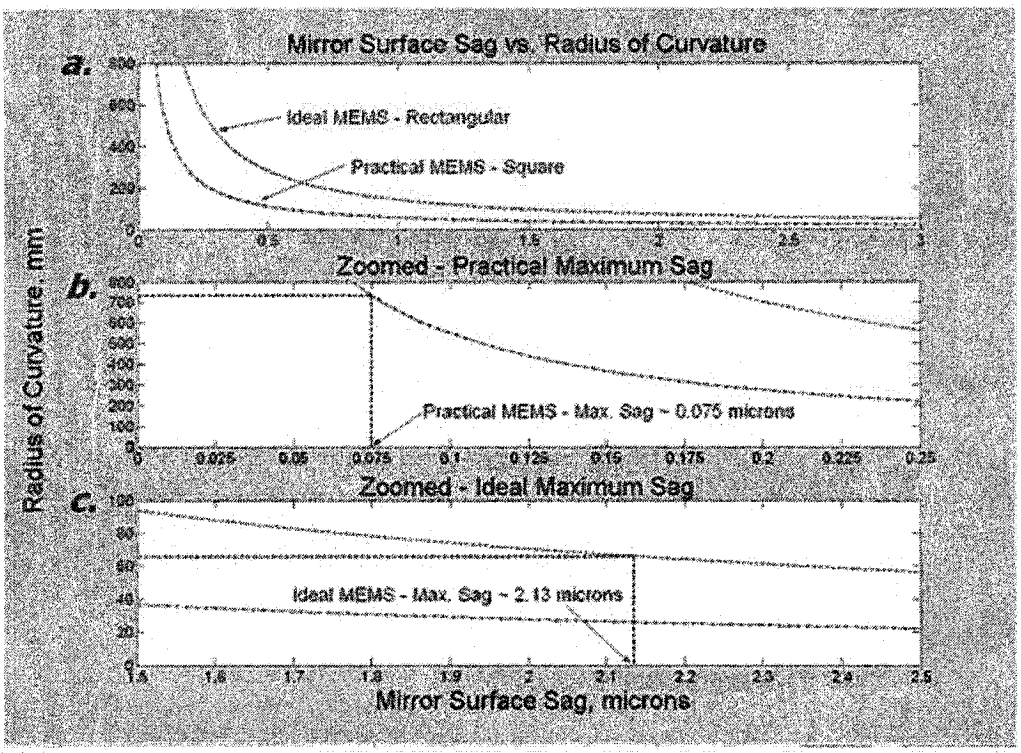

Figure 59 - Mirror Surface Curvature vs. Lateral Mirror Surface Sag

From the above curves, the minimum mirror radii of curvature of 720mm and 64mm therefore correspond to maximum mirror surface sags of 0.075μm [Figure 59(b)] and 2.13μm [Figure 59(c)] for the practical and ideal setups, respectively.

The above theoretical values for the practical setup are compared to experimental values in the subsequent chapter.

4.5 Summary

The numerical modeling of two implementations of the MEMS-Demo 1.5 FSOI has been presented. Lateral and angular misalignment tolerances for both systems were determined using Code V diffractive beam propagation simulations. Dynamic implementations of both MEMS systems allowed for correction for misaligned components, and therefore significant improvement in virtually all tolerances.

Additionally, the effect of mirror curvature on system performance was simulated in both setups. Minimum radii of curvature and therefore the maximum tolerable mirror surface sag were determined. The following chapter discusses the test and characterization of the two MEMS micro-mirror designs described in section 3.2.2.

5.0 Testing & Characterization of MEMS Micro-mirrors

The following section describes the testing and characterization of the implemented MEMS micro-mirror designs, highlighting the mechanical and physical characteristics of the prototypes implemented using the MUMPs process.

5.1 Experimental Setup

The two MEMS micro-mirror designs previously described were placed in a standard open-faced chip carrier and tested in order to examine the mechanical behavior, surface quality, and the uniformity of the arrays. Figure 60 shows a photograph of the MEMS chip, including both designs 1 and 2, and chip carrier.

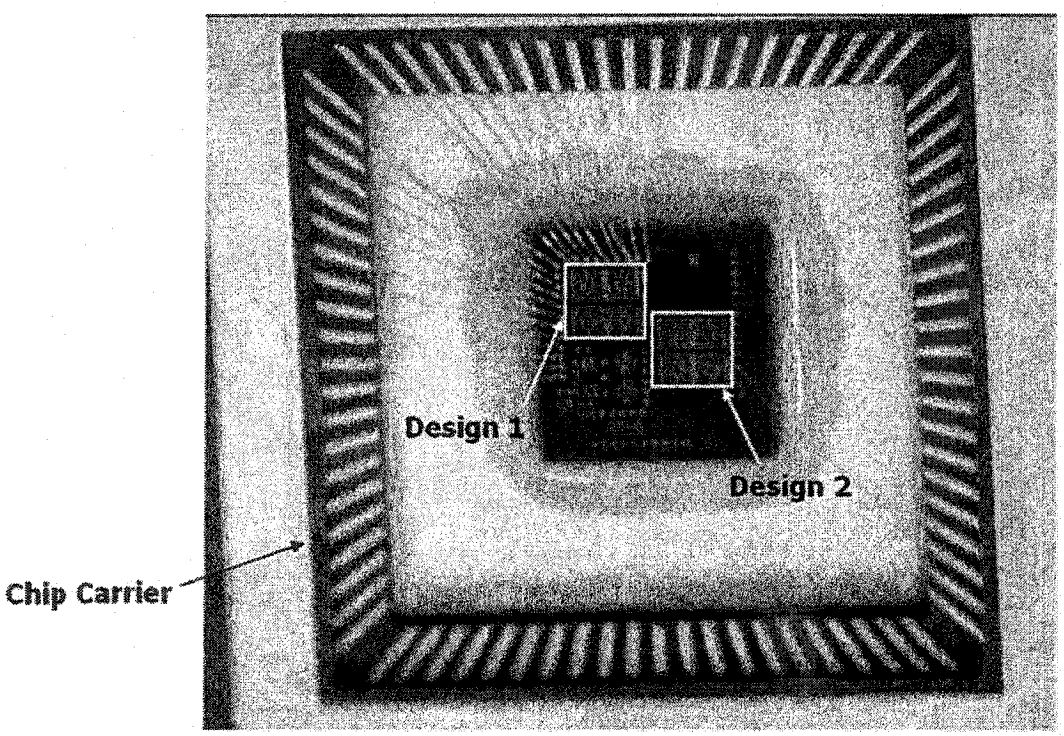

Figure 60 - Photograph of MEMS Chip & Chip Carrier

A thermally curing epoxy was used to fasten the chip to the chip carrier and aluminum wedge wirebonding was used to create the electrical interconnections between the address electrode bond pads on the chip and the pads on the chip carrier.

An optical profiler was used to test and characterize the prototyped micro-mirror designs. The test setup resembled the system documented in [19], and consisted of a phase-shifting Mirau interferometer, an *x-y-z* translation and tilt stage, and an electrical break-up unit. Figure 61 shows a schematic and photograph of the experimental setup.

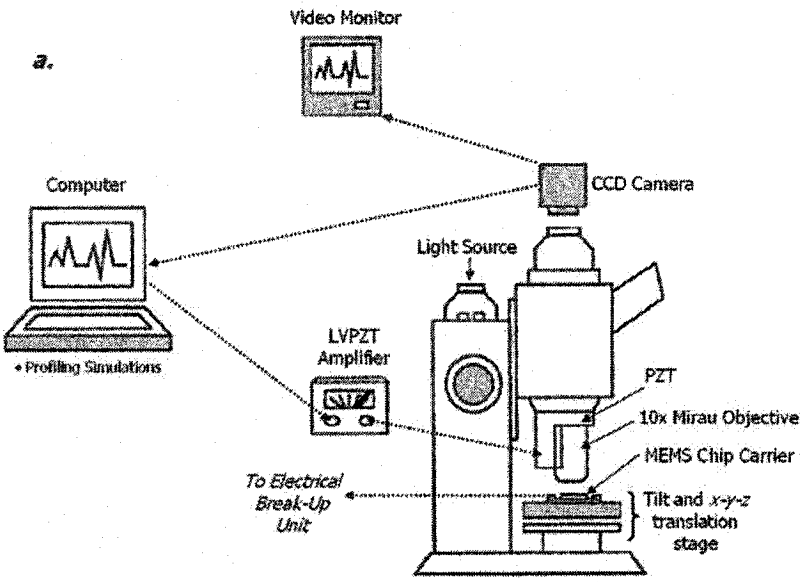

Adapted From: J. E. Lin, "Design and Characterization of MEMS Micro-mirror Devices", Master of Engineering Thesis, McGill University, Montreal, July 2001, pp. 64.

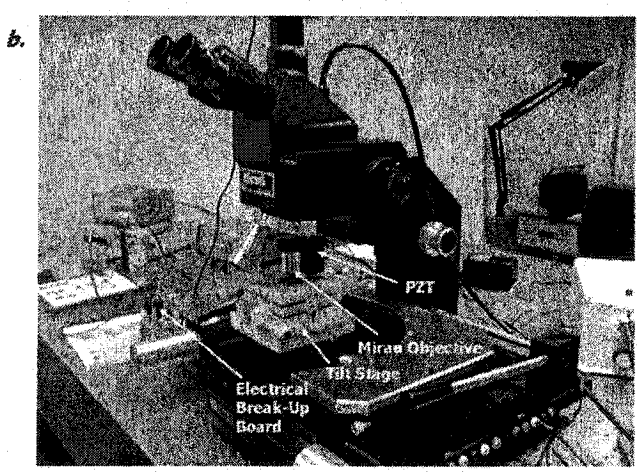

Figure 61 - MEMS Micro-mirror Test and Characterization Setup
a. Schematic, b. Photograph

As illustrated above, the phase-shifting Mirau interferometer was constructed using a white-light optical microscope, a 10x Mirau objective, and a CCD camera, mounted on a piezoelectric objective scanner (PZT).

According to the basic operating principles of an interferometer, by placing a test sample at one working distance away from the objective lens, patterns of light and dark fringes can be observed using a CCD camera [18]. These fringes represent constructive and destructive interference between waves of different path lengths originating from the sample. Using the PZT coupled with a computerized stepping algorithm, changes in these path lengths and therefore in the phase of the fringe pattern can be induced. Profiling programs, based on various phase-shifting algorithms, can be used to analyze these changes and create a representation of the surface profile of the sample. Vertical scanning interferometric software previously developed by the McGill Photonic Systems Group was used for this purpose [27], [28].

In order to obtain an accurate surface profile, it is critical that the surface of the sample is aligned perpendicular to the microscope objective. This was accomplished by placing the sample on *x-y-z* tilt and lateral positioning stages. The orientation of light and dark fringes on the surface of the sample, when viewed through the microscope, were used to indicate proper test sample alignment.

The electrical break-up unit facilitated electrical connection between the various pins on the chip carrier, and therefore the corresponding mirror address electrodes on the MEMS chip, to a standard voltmeter. By increasing the voltage in steps at individual and pairs of electrodes, mirror deflection was observed. Incorporating this unit into the phase-shifting Mirau interferometer, tests were performed to examine the mechanical operating characteristics of the micro-mirror designs.

The following section describes the test results for micro-mirror designs.

5.2 Design I – Test and Characterization

5.2.1 Surface Profile

The phase-shifting interferometer was used to obtain accurate surface profiles of the design I micro-mirrors at rest. Due to limitations in the optical resolution of the interferometer and the relatively large size of the mirror structures, only partial surface profiles could be obtained at any one time. Two important characteristics were examined – 1) surface quality, and 2) curvature of the mirror surface.

5.2.1.1 Surface Quality

Figure 62 shows a photograph of a design I micro-mirror array and a partial interferometric scan of a mirror surface.

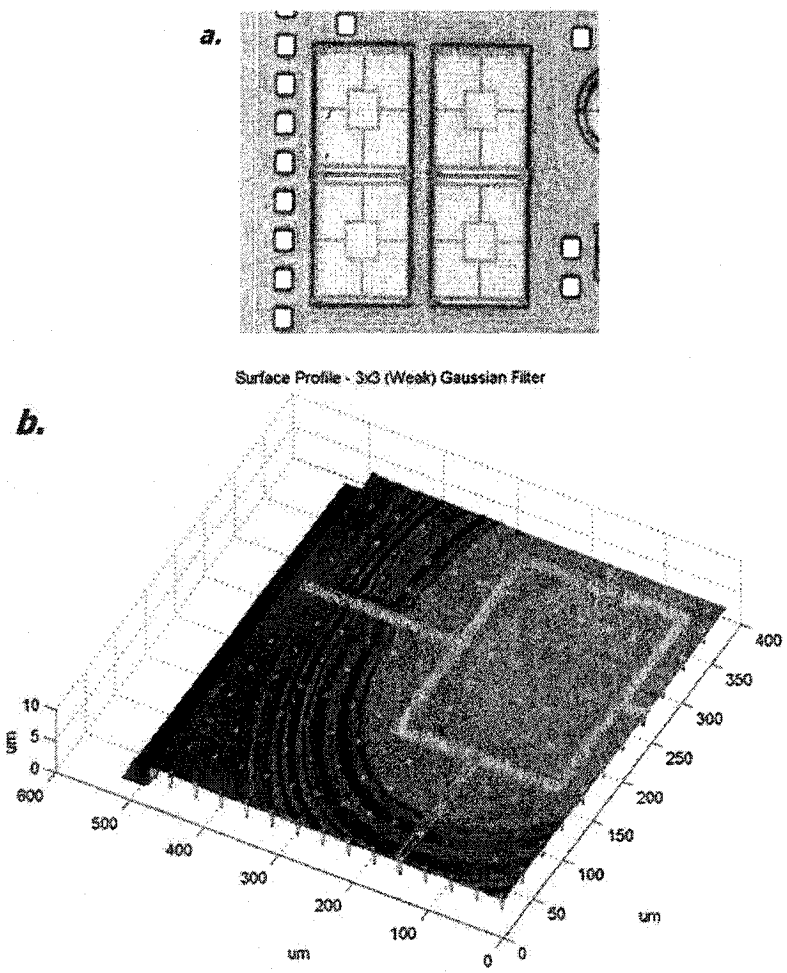

Figure 62 - Design I Micro-mirror
a. CCD capture of mirror under microscope, b. Partial Interferometric Scan of Surface Profile

As seen in the above photos, a considerable amount of print-through was visible on the mirror surface, originating from the poly0 address electrode structures beneath the mirror surface.

The holes visible in the mirror surface were used during the etching process to facilitate the releasing of the oxide layers from the poly1 mirror surface. Although small in relation to the size of the mirror surface, MUMPs process guidelines state a minimum 30μm spacing between poly1 etch holes [20]. Consequently a large array of etch holes was required in order to guarantee proper releasing of the mirror surface.

Both characteristics would undoubtedly increase scattering and diffraction, and therefore losses at the mirror surface.

5.2.1.2 Surface Curvature

Accurate representations of the surface profiles of design I micro-mirrors were obtained by examining the degree of surface curvature from cross-sections of the mirror surface in both diagonal and lateral directions. Figure 63 shows the locations of the appropriate cross-sections. These cross sections will be referred to repeatedly in the following discussion.

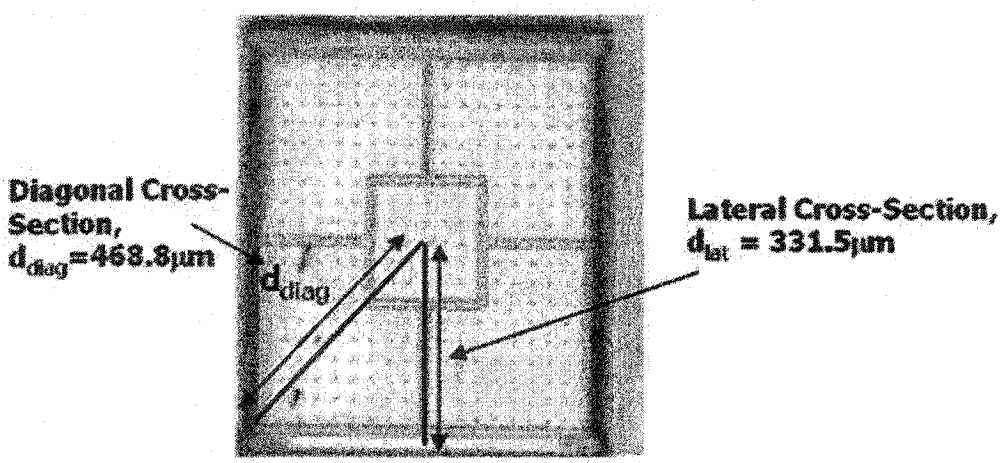

Figure 63 - Diagonal and Lateral Cross-Sections of Design I Mirror

Figure 64 shows a diagonal cross-section of a design I mirror surface obtained from the optical profiling simulations.

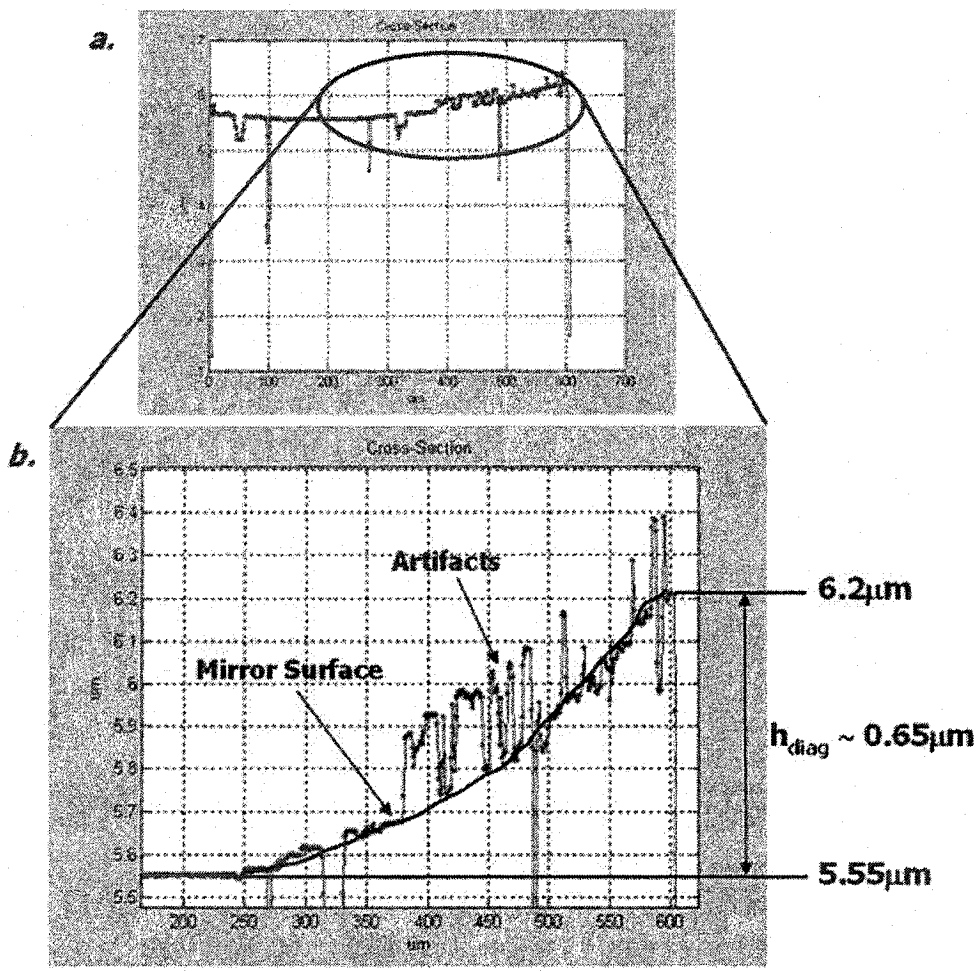

Figure 64 – Diagonal Cross-section of Design I Mirror Surface
a. Diagonal mirror surface profile, b. Diagonal surface profile – zoomed

Figure 64(a) clearly shows a sagging central portion of the mirror surface. Figure 64(b) shows a zoomed in portion of the graph in part (a). From this graph, the edge and the center of the micro-mirror surface along the diagonal were measured at heights of approximately 6.20µm and 5.55µm above the chip substrate, resulting in a diagonal surface sag of approximately h_{diag} = 0.65µm. Surface sags of this magnitude were present to a similar degree in all other scans of design I mirrors.

It must be noted that spikes in the above curve are artifacts of the interferometric scan, representing residual noise from etch holes as well small errors in positioning of the test sample. Similar results were observed for lateral cross sections of the mirror surface.

Figure 65 shows a lateral cross-section of a design I mirror surface obtained from the optical profiling simulations.

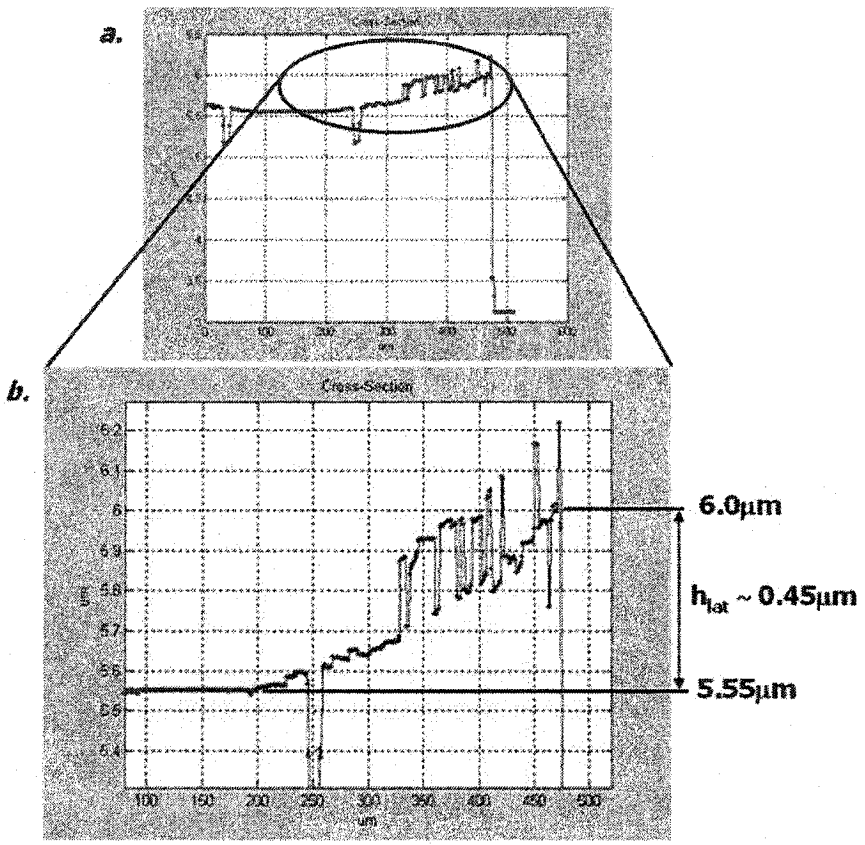

Figure 65 - Lateral Cross-Section of Design I Mirror Surface
a. Partial mirror surface profile along lateral cross-section, b. Lateral surface profile – zoomed

Figure 65(b) shows a zoomed in portion of the surface profile, indicating the magnitude of lateral mirror surface sag. Similar to the diagonal cross-section, surface profile scans indicate that the central portion of the mirror surface sags to a relative height of 5.55µm above the chip substrate. In the former case, the edge of the mirror referred to the far corner of the mirror surface, and was measured at a height of 6.2µm. In the latter case, however, along the lateral cross-section of the mirror, the edge of the mirror lacks the support of the hinge structure at the corner of the mirror. Correspondingly, as illustrated

in Figure 65(b), the edge of the mirror dropped to a height of approximately 6.0μm above the chip substrate, resulting in a total lateral surface sag of approximately $h_{lat} = 0.45\mu m$.

As discussed in section 3.2.3.2, given the dimensions of the mirror surface relative to the degree of sag measured at the center of the mirror surface, a spherical surface is an accurate approximation of both the lateral and diagonal surface profiles. Using equation (23) in section 4.4.3, diagonal and lateral side lengths of 468.8μm and 331.5μm [shown in Figure 63], respectively, and the measured surface sags above, correspond to diagonal and lateral mirror surface curvatures of $R_{diag} \approx 122.10mm$ and $R_{lat} \approx 169.06mm$, respectively. Although the lateral sag is less in magnitude than the sag across the mirror diagonal, the lateral distance over which the sag occurs is less, thereby giving the mirror surface a smaller radius of curvature. This results in a more concave mirror surface in the lateral direction towards the edge of the mirror surface. Figure 65 shows plots of both the measured surface profiles superimposed on spherical surfaces with radii of curvature to fit the measured data.

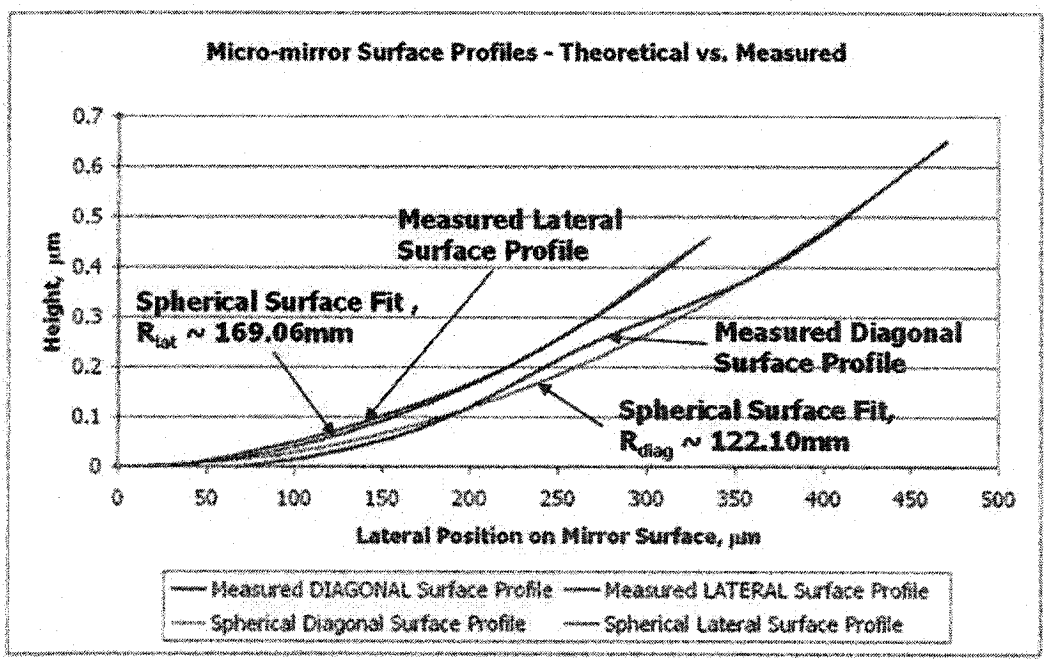

Figure 66 - Measured & Spherical Surface Fit Micro-mirror Surface Profiles

Figure 65 illustrates that the measured surface profiles adhere well to the profiles of spherical surfaces with two *different* radii of curvature. This confirms the assumption that the sag of the micro-mirror surface for this design may be modeled as spherical in nature.

The differences in radii of curvature in the lateral and diagonal directions create a non-uniform aspherical mirror surface, which, in a test setting, would clearly cause increased losses at the mirror surface, thereby making the mirror extremely optically inefficient. Pertaining to the performance of curved mirrors in the practical MEMS-Demo 1.5 system, the smallest radii of curvature will be the limiting factor. In this case, the radius of curvature of the diagonal cross-section, 122.10mm, is well below the 720mm minimum radii of curvature determined from the simulations described in section 4.4.3. Referring to Figure 67 below, this translates into a theoretical maximum practical MEMS system throughput of approximately 48% - an unacceptable level of losses.

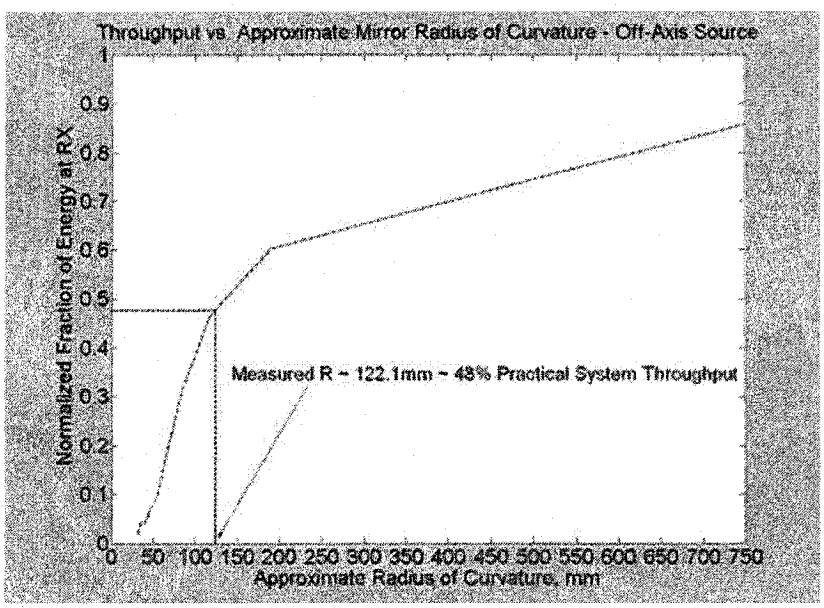

Figure 67 - System Throughput for Measured Mirror Surface Radii of Curvature

Overall, in order to allow for the use of these mirrors in a proper laboratory setting, improved designs must be investigated with the aim of decreasing the degree of surface sag and improving surface uniformity. Possible improvements to this design are discussed in section 5.4.

5.2.2 Operating Characteristics

The operation of design I micro-mirrors was observed by grounding the micro-mirror structure and applying positive voltages to various address electrodes using the electrical break-up unit and voltmeter. The resulting surface profile was used to determine the lateral angular deflection and pull-in characteristics of the micro-mirrors.

5.2.2.1 Lateral Angular Deflection

As illustrated in Figure 68 below, lateral mirror deflection was measured by applying positive voltage to pairs of adjacent address electrodes, for example E3 and E4, and obtaining both side edge and center cross-sections of the mirror surface across the entire surface of the mirror (i.e. from E1 to E3).

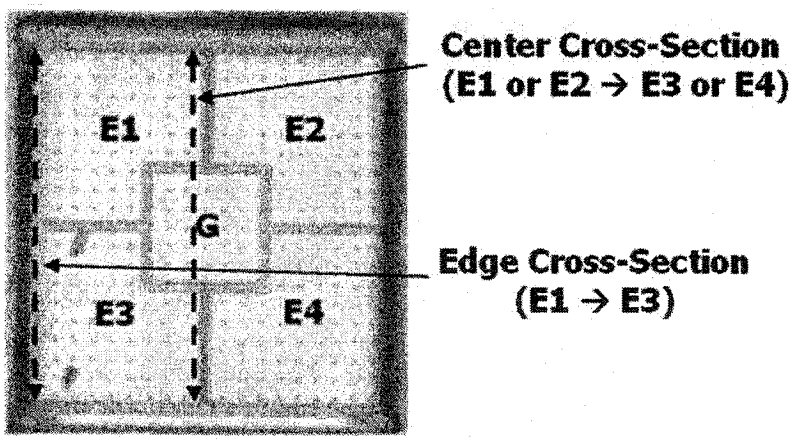

Figure 68 - Measuring Lateral Angular Deflection

In each case, the applied voltage was increased in steps until pull-in condition was achieved.

Figure 69 shows cross-sections of the lateral deflection of the mirror surface for an applied voltage of 2V on electrodes E3 and E4.

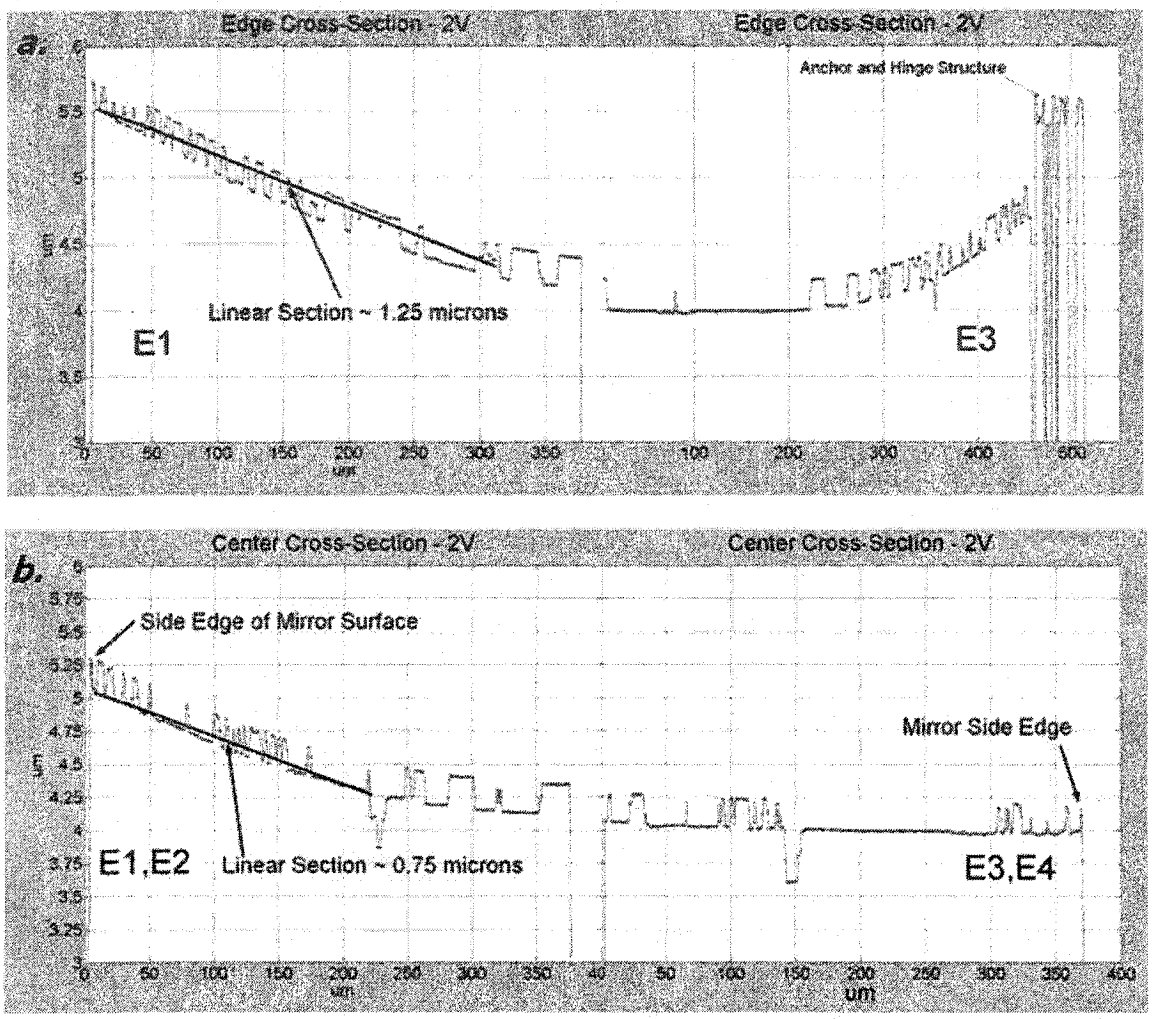

Figure 69 - Lateral Mirror Surface Profiles for Applied Voltage of 2V on E3 and E4
a. Edge surface profile, b. Center surface profile

Figure 69(a) shows cross-sections of a side edge of the mirror surface from E1 to E3. The mirror surface at the hinge above E1 (far left) is level with the anchor structure at a height of approximately 5.5μm above the chip substrate. Laterally along the edge of the mirror from E1 to E3, the mirror surface deflects in a linear fashion for a lateral distance of 330μm (roughly one-half the side length of the mirror), to a height of roughly 4μm. This results in a vertical deflection of approximately $\Delta h_{2V\text{-}edge} \approx 1.25\mu m$ and an equivalent angular deflection of this section of the mirror surface of $\theta_{2V\text{-}edge} \approx 3.77mrad = 0.216^{\circ}$. The remaining portion of the mirror surface is held flat at a height of approximately 4μm, before curving upwards by 0.75μm towards the opposite hinge above the E3 electrode.

A similar surface profile was observed for a lateral cross-section across the center of the mirror surface [Figure 69(b)]. Linear angular deflection was observed for approximately 200μm laterally across the surface, resulting in a vertical deflection of approximately $\Delta h_{2V\text{-}mid} \approx 0.75\mu m$ or an angular tilt, $\theta_{2V\text{-}mid} \approx 3.74mrad = 0.214^{\circ}$, while the remaining portion of the mirror above electrodes E3 and E4 was pulled flat to a height of approximately 4μm.

Figure 70 below shows the deflection of the mirror surface for an applied voltage of 6V on electrodes E3 and E4.

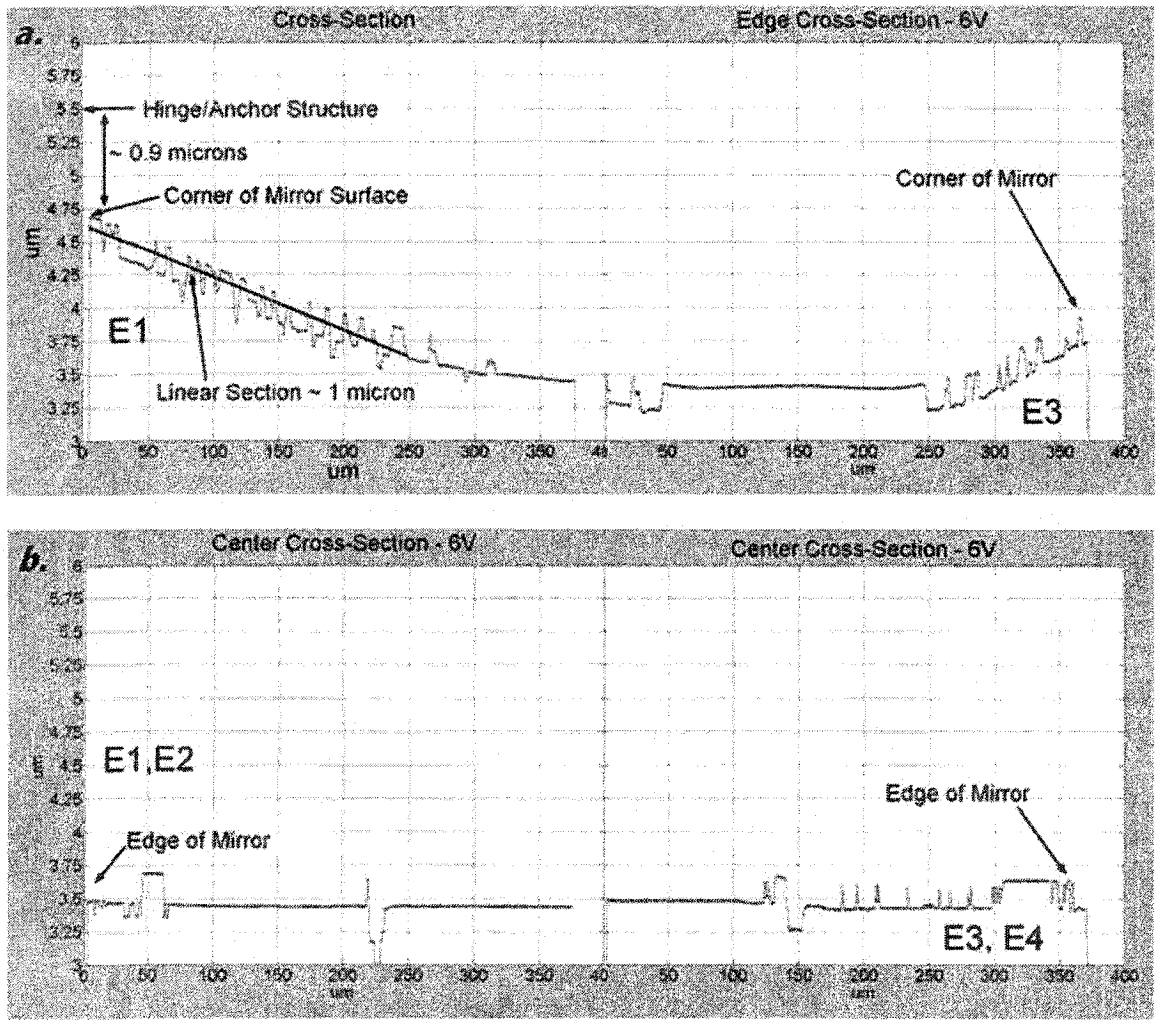

Figure 70 - Lateral Deflection for Applied Voltage of 6V on E3 and E4
a. Edge surface profile, b. Center surface profile

Figure 70(a) shows a cross-section of the side edge of the mirror surface. At this voltage, the voltage was sufficient to pull the far corner of the mirror surface down to a height of 4.6μm – a distance of 0.9μm below the anchor structure. Moving laterally along the edge of the mirror surface, a similar linear-like deflection occurred over a lateral distance equal to 250μm resulting in a total vertical deflection of approximately $\Delta h_{6V\text{-}edge} \approx 1\mu m$ or $\theta_{2V\text{-}edge} \approx 4mrad = 0.229^{o}$. As was the case for an applied voltage of 2V, the remaining half of the mirror surface was pulled flat to a height of 3.5μm.

Figure 70(b) shows a cross-section of the middle of the mirror surface. Unlike the edge of the mirror surface, the applied voltage was sufficient to pull the entire middle portion of the mirror flat to a height of 3.5μm. Given that the maximum mirror surface-substrate gap is 2μm for the design 1 micro-mirrors, and the maximum height of the mirror surface in the scan was 5.5μm, any further increase in the applied voltage would have caused the mirror surface to pull into contact with the address electrodes on the chip substrate.

Figure 71 compares the measured mirror edge surface profiles for applied voltages of 2V and 6V(left-sides of the curves in Figure 69 and Figure 70), to the maximum predicted linear mirror surface deflection, described in section 3.2.2.1. Note that this figure shows cross-sections of only one-half of the mirror surface.

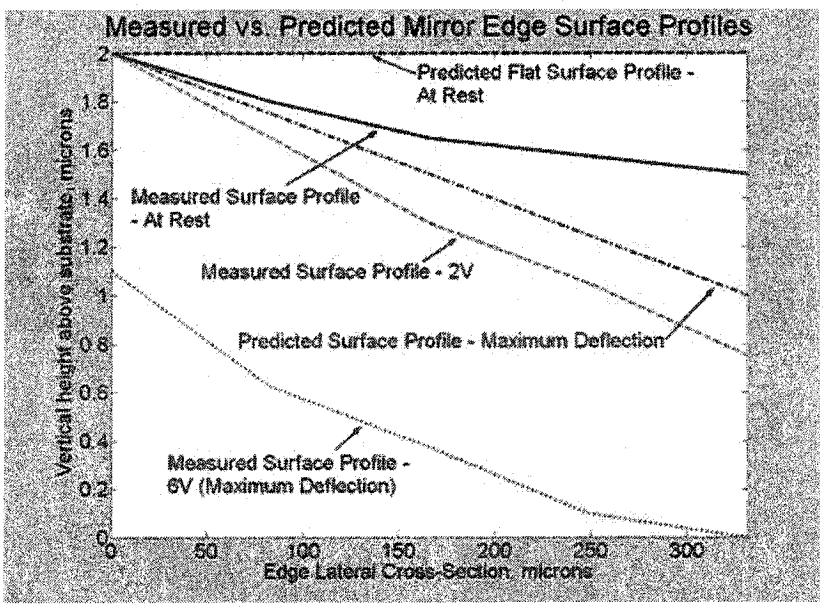

Figure 71 - Measured vs. Predicted Mirror Edge Surface Profiles

The measured surface profiles for applied voltages of both 2V and 6V are significantly deviated from the predicted result for maximum theoretical mirror deflection. In all cases, operating voltages, although linear deflections were observed for portions of the mirror surface, the lateral angular deflection of the mirror surface was highly non-uniform, as the electrodes pulled one-half of the mirror surface flat to a constant height above the chip substrate, while causing a linear angular deflection in the remaining half. This indicates that applied voltages induced a change in curvature of the mirror surface, rather than a distinct angular deflection.

5.2.2.2 Pull-in Voltage

On average, pull-in voltages ranged from 6V to 9V in both lateral and diagonal directions. Distinct pull-in angles were not observable as a result of the non-uniform deformation of the mirror surface during actuation, as discussed above.

Additionally, it was found that once pull-in occurred, the effects were irreversible, and the mirror surface remained attached to the substrate, causing the mirrors to become inoperable. This permanent deformation was attributed to the large size of the mirror surface, and the minimal degree of support in the center of the mirror surface inherent with such a design. Figure 72 shows an interferometric scan of a mirror frozen in the pull-in state.

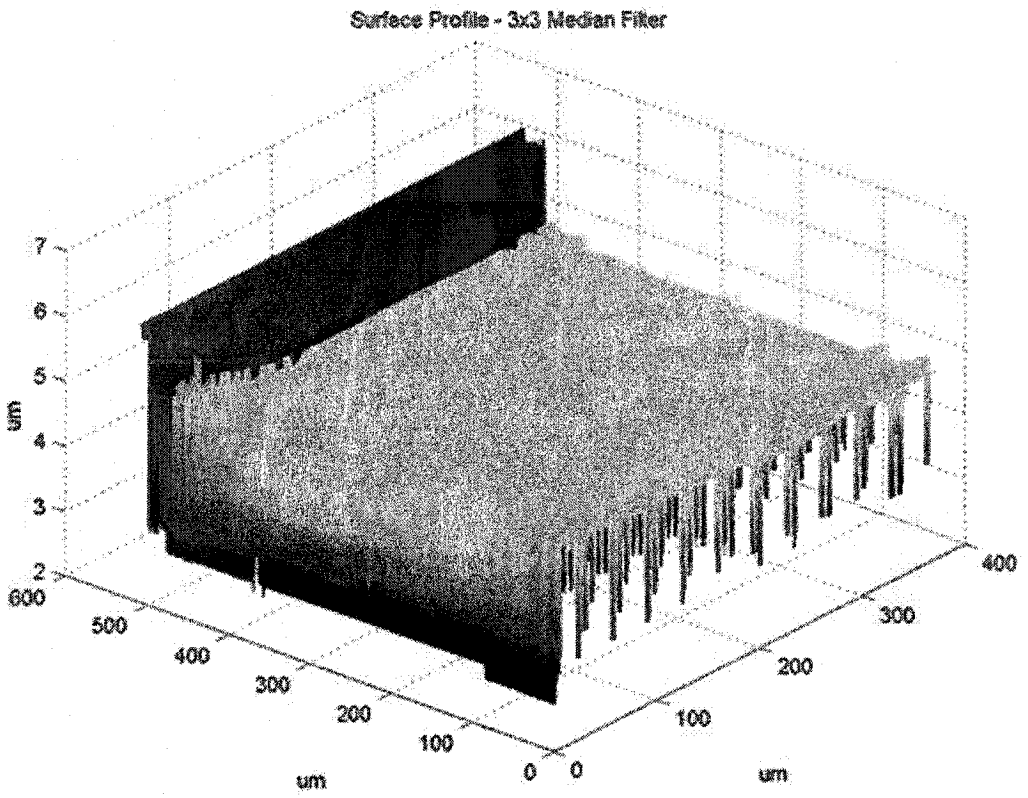

Figure 72 – Scan of Design I Micro-mirror at Pull-In

5.3 Design II – Test and Characterization

As a result of an error in design, the prototyped design II micro-mirrors were found to have a fatal structural defect. During the design process, improper dimensioning of the poly2 mirror surface etch holes resulted in improper etching of the underlying oxide layers during fabrication. As a result, these layers failed to release from the poly2 mirror surface post-fabrication. As shown in Figure 73, this resulted in a 'dome-shaped' mirror surface profile.

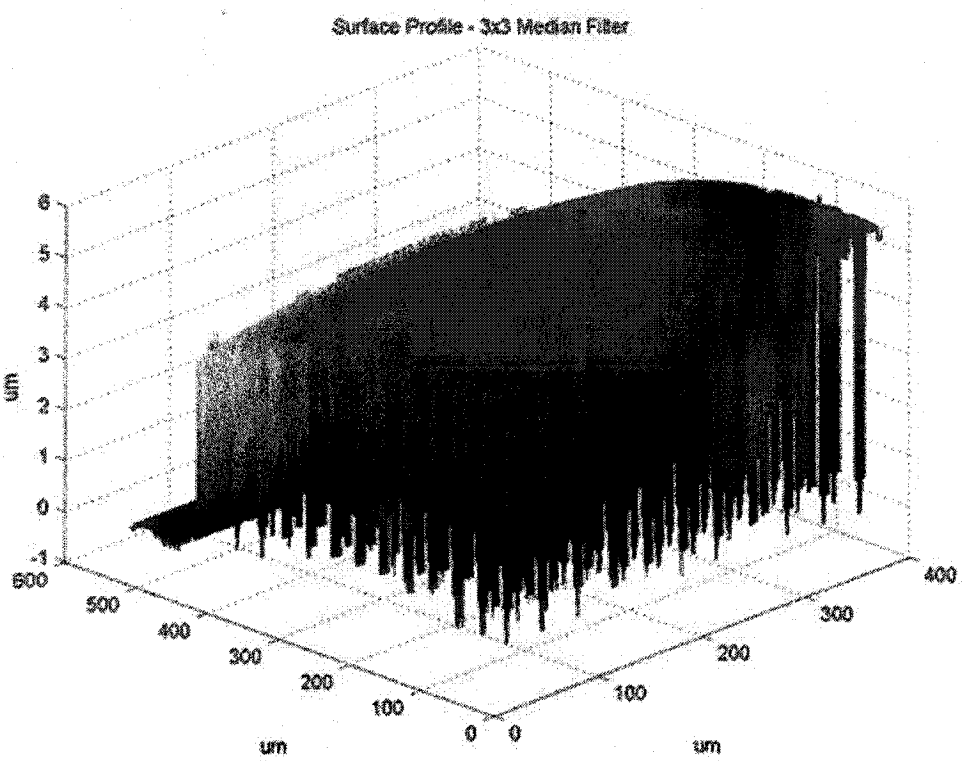

Figure 73 - Scan of Faulty Design II Micro-mirror

Consequently, the pull-ring structures shattered when removed, leaving the poly1 sacrificial layer underneath the mirror surface, causing the mirrors to be inoperable. A third design was implemented to correct for this flaw, however, due to time restrictions, did not fit into the scope of this thesis.

5.4 Analysis – Implemented Designs

Ultimately, the implemented designs failed to perform as anticipated. The mirror surfaces were found exhibit substantial curvature, and when operated, non-uniform deformation of the mirror surfaces was observed. Such results indicate that efficient integration of these designs into the Demo 1.5 FSOI is not possible.

The results of the characterization of implemented micro-mirrors can be explained considering three major factors.

First and foremost, the large size of the mirror relative to the thickness of the mirror surface and the height of the surface-substrate gap available from the MUMPs process, had an effect of increasing the surface sag, in addition to contributing towards the non-uniform change in curvature observed during mirror actuation. As flexure hinges were positioned only at the four corners of the mirror surface, the design suffered from a lack of support from at the center of the side edges of the mirror surface. Potential solutions to these problems therefore include an increased surface-substrate gap to reduce the non-desired vertical surface shift and surface curvature, the deposition of an additional layer on the mirror surface to increase rigidity without increasing surface sag, as well as strategic positioning of additional hinges around the edges of the mirror surface to allow for increased support, as well as improve uniform angular deflection of the mirror surface.

Secondly, the large size of the address electrodes had the effect of shifting the entire mirror surface down during actuation, instead of causing a smooth angular deflection in the surface. A possible solution to this problem, as was proposed in [18], could be to shrink the size of the electrodes and position them around the edges of the mirror surface, thereby reducing the electrostatic torque on the unsupported center portion of the micro-mirror. A second potential solution involves the use arrays of smaller address electrodes beneath the mirror surface. Applying the appropriate voltages to each electrode in the array would effectively create a voltage gradient across the mirror surface, resulting in a smoother, more distinct, angular deflection.

The third major detrimental design factor was the corner hinge design. In using such a design, the lack of vertical flexibility of the hinges induced a change in curvature at the corners of the mirror surface. One potential solution to this problem could be in the form of more flexible hinges, allowing increased vertical movement, thereby allowing the hinges to be pulled downwards with the mirror surface. However, because of the trade-off between surface sag and hinge strength, increasing the flexibility could contribute to increased surface sag and a weaker mirror structure. A second potential solution in this area combines the use of additional layers to create a more rigid mirror surface combined with the gimbal flexure hinge design documented in [18], [21] [Figure 15]. This would

allow for a more uniform mirror deflection in two axes. However, too heavy a mirror surface with such a hinge design could cause the mirror surface bend towards the substrate at the edges, making the mirror inoperable.

The validity of the proposed solutions, however, is ultimately dependent on the limitations of the MUMPs process. Restrictions imposed on the maximum layer thicknesses, the number of structural layers, as well as the materials used in multi-user MEMS processes may fundamentally make micro-mirrors such as those prototyped in this thesis, impractical given the current technology. Detailed finite element modeling of large MUMPS micro-mirrors could reveal the answer to this question. To this end, future work will involve investigating not only the solutions presented above using CAD finite element analysis, but also reviewing alternative MEMS processes for developing optimal micro-mirrors for such an application.

5.5 Summary

The test and characterization of the implemented MEMS micro-mirror designs has been presented. Both surface profiling and mechanical operating characteristics were examined using a Mirau interferometer and customized optical profiling simulations. Surface profiling of micro-mirror design I indicated a significant amount of print-through and substantial curvature in the mirror surface. Design I mirrors exhibited non-uniform deformation when actuated, causing the mirror surface to eventually be pulled flat against the chip substrate for applied voltages in excess of 6V. As a result of an error in the second implemented design, design II mirror surfaces failed to release from the underlying oxide layers, causing the design II mirrors to be inoperable. Given these results, the implemented micro-mirror designs were deemed unsuitable for integration with the existing Demo 1.5 FSOI. Future design work will involve optimizing various aspects of the micro-mirror designs including electrode designs, hinge configurations, and mirror surface materials using finite element CAD models, as well as investigating alternative MEMS processes for developing efficient micro-mirrors for such an application.

6.0 Conclusions

This thesis has examined the feasibility of using MEMS micro-mirrors for achieving adaptive alignment in a previously implemented free-space optical interconnect. In this scheme, dynamic beam steering is the mechanism through which component misalignment correction is achieved, allowing for the system to operate within minimum constraints.

Based on characteristics of the existing system, an optimized integrated design was developed, giving the system the required full functionality as it pertains to correcting for both lateral and angular tilt component misalignment. Two sets of MEMS micro-mirror devices were prototyped using the MUMPs surface micro-machining foundry service. Although identical in size and in dimensions, the second design sought to improve on the maximum obtainable mirror surface angular deflection. In both cases, issues such as beam clipping at the aperture of the mirrors and mirror surface sag were determined to be potential performance limiting factors.

With the goal of determining the impact of integrating the MEMS devices into the existing system, two sets of diffractive Gaussian beam propagation numerical simulations were performed on a test version of the existing system. In light of the aforementioned performance issues, an additional improved mirror design with larger mirror surface dimensions was considered for these simulations.

The first set of simulations examined the performance of the adaptive alignment scheme, in order to determine the corrective ability of the MEMS beam steering system. Results highlighted increases in lateral misalignment tolerances by scale factors as little as 1.65 and as great as 11, when compared to the static versions. Although in some cases the

MEMS beam steering system was unable to improve angular tilt tolerances, increases by as much as 0.785° were observed in others – all significant improvements.

The second set of simulations investigated the effects of micro-mirror surface curvature on the integrated system. Results indicated mirror curvature to have a dramatic effect on the overall performance of the system. For a maximum 5% drop in system throughput, minimum radii of curvature of 720mm and 64mm were determined for the implemented and improved mirror designs, respectively. The former case illustrated that mirrors must be relatively flat in order for the system to operate within minimum tolerances – a challenging requirement given the large mirror dimensions.

The two mirror prototypes were tested using a phase-shifting Mirau interferometer. Both the quality and curvature of the mirror surface, as well as the mechanical behavior of the micro-mirrors were investigated. At rest, design I mirror surfaces were found to suffer from a significant degree of print-through of the underlying address electrodes, as well as irregular surface curvature at different points on the mirror surface. Compared to those values obtained in numerical simulations, an approximation of the minimum radii of curvature was found to correspond to an overall throughput of 48% in the integrated system – an unacceptable level of losses. Control voltages in the range 2 to 6V were sufficient to operate the mirrors. Contrary to initial predictions, a non-uniform deformation of the mirror surface resulted from a lack of surface support and the size and position of the control electrodes. Pull-in condition occurred for voltages greater than 6V, and resulted in permanent deformation of the mirror surface. An error in design II caused improper releasing of the underlying oxide layers from the mirror surfaces, making the mirrors inoperable. A third design was implemented to correct for this problem, however, due to time restrictions did not fit into the scope of this thesis.

The prototyped MEMS designs failed to perform up to initial expectations. Nevertheless, the results of the numerical simulations presented in this thesis have indicated adaptive alignment in free-space optical interconnects to be a promising application for MEMS micro-mirror devices. Future work will focus on improving micro-mirror designs by

pursuing alternative supportive flexure hinge designs, control electrode positions and sizes, mirror surface materials, as well as addressing control issues pertaining to the adaptive beam steering alignment system. Additionally, finite element models will be used required to determine if mirrors as large as those implemented for the purpose of this thesis are practical, under current MUMPs design guidelines. To this end, alternative MEMS prototyping processes will be reviewed, with the aim of achieving adequate MEMS micro-mirror designs for integration into the existing interconnect design.

7.0 Appendices

7.1 Appendix I – Code V System Data Spreadsheets

Table 5 - Code V Lens Data Manager Spreadsheet

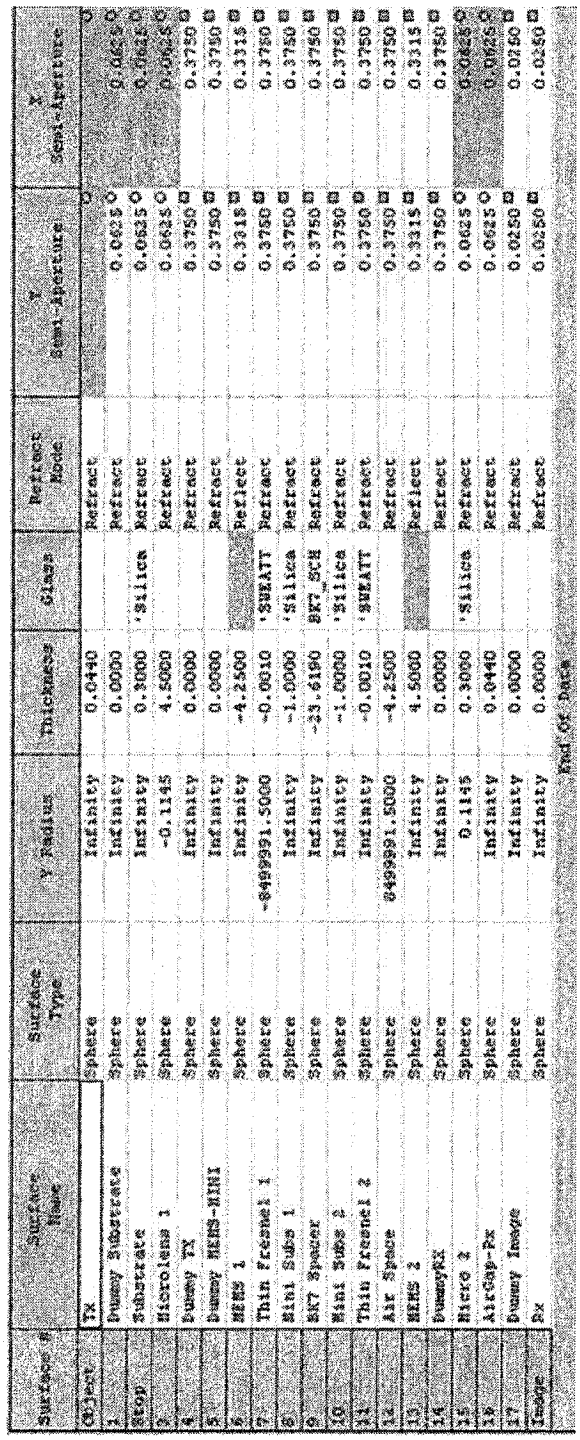

Surface #	Surface Name	Surface Type	Y Radius	Thickness	Glass	Refract Mode	Y Semi-Aperture	X Semi-Aperture
Object	Tx	Sphere	Infinity	0.0440		Refract	0	0
1	Dummy Substrate	Sphere	Infinity	0.0000		Refract	0.0625	0.0625
Stop	Substrate	Sphere	Infinity	0.3000	'Silica	Refract	0.0625	0.0625
3	Microlens 1	Sphere	-0.1145	4.5000		Refract	0.0625	0.0625
4	Dummy Tx	Sphere	Infinity	0.0000		Refract	0.3750	0.3750
5	Dummy MEMS-MINI	Sphere	Infinity	0.0000		Refract	0.3750	0.3750
6	MEMS 1	Sphere	Infinity	-4.2500		Reflect	0.3315	0.3315
7	Thin Fresnel 1	Sphere	-8499991.5000	-0.0010	'SUEATT	Refract	0.3750	0.3750
8	Mini Subs 1	Sphere	Infinity	-1.0000	'Silica	Refract	0.3750	0.3750
9	BK7 Spacer	Sphere	Infinity	-33.6190	BK7_SCH	Refract	0.3750	0.3750
10	Mini Subs 2	Sphere	Infinity	-1.0000	'Silica	Refract	0.3750	0.3750
11	Thin Fresnel 2	Sphere	Infinity	-0.0010	'SUEATT	Refract	0.3750	0.3750
12	Air Space	Sphere	8499991.5000	-4.2500		Refract	0.3750	0.3750
13	MEMS 2	Sphere	Infinity	4.5000		Reflect	0.3315	0.3315
14	DummyRX	Sphere	Infinity	0.0000		Refract	0.3750	0.3750
15	Micro 2	Sphere	0.1145	0.3000	'Silica	Refract	0.0625	0.0625
16	AirGap-Rx	Sphere	Infinity	0.0440		Refract	0.0625	0.0625
17	Dummy Image	Sphere	Infinity	0.0000		Refract	0.0250	0.0250
Image	Rx	Sphere	Infinity	0.0000		Refract	0.0250	0.0250
				End Of Data				

Table 6 - Code V Decentered Surface Data Spreadsheet

	Surface #	Decenter Type	Global Reference Surface	X Decenter	Y Decenter	Z Decenter	Alpha Tilt	Beta Tilt	Gamma Tilt
0	1 - Dummy Substrat	Global Coordinates	Object - Tx	0.0000	0.0000	0.0440	0.0000	0.0000	0.0000
1	Stop - Substrate	Global Coordinates	Object - Tx	0.0000	0.0000	0.0440	0.0000	0.0000	0.0000
2	3 - Microlens 1	Global Coordinates	Stop - Substrate	0.0000	0.0000	0.3000	0.0000	0.0000	0.0000
3	4 - Dummy TX	Global Coordinates	1 - Dummy Substrate	-0.1875	0.1875	4.8000	0.0000	0.0000	0.0000
4	5 - Dummy MEMS-MIN	Global Coordinates	1 - Dummy Substrate	-0.1875	0.1875	4.8000	0.0000	0.0000	0.0000
5	6 - MEMS 1	Global Coordinates	5 - Dummy MEMS-MINI	0.0000	0.0000	0.0000	-45.0000	0.0000	0.0000
6	7 - Thin Fresnel 1	Global Coordinates	5 - Dummy MEMS-MINI	0.0000	4.2500	0.0000	-90.0000	0.0000	0.0000
7	8 - Mini Subs 1	Global Coordinates	7 - Thin Fresnel 1	0.0000	0.0000	-0.0010	0.0000	0.0000	0.0000
8	9 - BK7 Spacer	Global Coordinates	7 - Thin Fresnel 1	0.0000	0.0000	-1.0010	0.0000	0.0000	0.0000
9	10 - Mini Subs 2	Global Coordinates	7 - Thin Fresnel 1	0.0000	0.0000	-24.6200	0.0000	0.0000	0.0000
10	11 - Thin Fresnel 2	Global Coordinates	7 - Thin Fresnel 1	0.0000	0.0000	-25.6200	0.0000	0.0000	0.0000
11	12 - Air Space	Global Coordinates	7 - Thin Fresnel 1	0.0000	0.0000	-25.6210	0.0000	0.0000	0.0000
12	13 - MEMS 2	Global Coordinates	5 - Dummy MEMS-MINI	0.0000	34.3085	0.0000	-135.0000	0.0000	0.0000
13	14 - DummyRX	Global Coordinates	4 - Dummy TX	-0.1875	34.1210	0.0000	0.0000	0.0000	0.0000
14	15 - Micro 2	Global Coordinates	14 - DummyRX	0.0000	0.0000	-4.5000	-180.0000	0.0000	0.0000
15	16 - AirGap-Rx	Global Coordinates	15 - Micro 2	0.0000	0.0000	0.3000	0.0000	0.0000	0.0000
16	17 - Dummy Image	Global Coordinates	15 - Micro 2	0.0000	0.0000	0.3440	0.0000	0.0000	0.0000
			End Of Data						

8.0 References

[1] D. V. Plant and A. G. Kirk, "Optical Interconnects at the Chip and Board Level: Challenges and Solutions." *Proceedings of the IEEE*, Vol. 88, 2000, pp. 806-818.

[2] C.V Cryan, "Two-dimensional multimode fiber array for optical interconnects." *Electronics Letters*, Vol. 34, 1998, pp. 586-587.

[3] T. Maj, A. G. Kirk, D. V. Plant, J. F. Ahadian, C. G. Fonstad, K. L. Lear, K. Tatah, M. S. Robinson, and J. A. Trezza. "Interconnection of a two-dimensional array of vertical cavity surface-emitting lasers to a receiver array by means of a fiber image guide." *Applied Optics*, Vol. 39, 2000, pp. 683-689.

[4] H. Kosaka, M. Kajita, Y. Li, and Y. Sugimoto, "A Two-dimensional Optical Parallel Transmission Using a Vertical-Cavity Surface-Emitting Laser Array Module and an Image Fiber." *IEEE Photonics Technology Letters*, Vol. 9, 1997, pp.253-255.

[5] M. Châteauneuf, A. G. Kirk, D. V. Plant, T. Yamamoto, and J. D. Ahearn, "512-channel vertical-cavity surface-emitting laser based free-space optical link." *Applied Optics*, Vol. 41, 2002, pp. 5552-5561.

[6] E. Bisaillon, D. F. Brosseau, T. Yamamoto, M. Mony, E. Bernier, D. Goodwill, D. V. Plant, and A. G. Kirk, "Free-Space Optical Link with Spatial Redundancy for Misalignment Tolerance." *IEEE Photonics Technology Letters*, Vol. 14, 2002, pp. 242-244.

[7] A. Tuantranont, V. M. Bright, J. Zhang, W. Zhang, J. A. Neff, and Y. C. Lee, "Optical beam steering using MEMS-controllable microlens array." *Sensors and Actuators A*, Vol. 91, 2001, pp. 363-372.

[8] F. Lacroix, M. Châteauneuf, X. Xue, and A. G. Kirk, "Experimental and numerical analyses of misalignment tolerances in free-space optical interconnects" *Applied Optics*, Vol. 39, 2000, pp. 704-713.

[9] G. C. Boisset, D. R. Rolston, B. Robertson, Y. S. Liu, R. Iyer, D. Kabal, and D. V. Plant, "In-situ Measurement of Misalignment Errors in Free-Space Optical Interconnects." *Journal of Lightwave Technology*, Vol. 16, 1998, pp. 847-858.

[10] G. C. Boisset, B. Robertson, and H. S. Hinton, "Design and Construction of an Active Alignment Demonstrator for a Free-Space Optical Interconnect." *IEEE Photonics Technology Letters*, Vol. 7, 1995, pp. 676-678.

[11] D. V. Plant, M. B. Venditti, E. Laprise, J. Faucher, K. Razavi, M. Châteauneuf, A. G. Kirk, and J. S. Ahearn, "256-channel bidirectional optical interconnect using VCSELs and photodiodes on CMOS." *Journal of Lightwave Technology*, Vol. 19, 2001, pp. 1093-1103.

[12] X. Zheng, P.J. Marchand, D. Huang, and S. C. Esener, "Free-space parallel multichip interconnection system." *Applied Optics*, Vol. 39, 2000, pp. 3516-3524.

[13] F. P. Tooley, "Challenges in Optically Interconnecting Electronics." *IEEE Journal of Selected Topics in Quantum Electronics*, Vol. 2, 1996, pp. 3-13.

[14] E. M. Strzelecka, D. A. Louderback, B. J. Thibeault, G. B. Thompson, K. Bertilsson, and L. A. Coldren, "Parallel free-space optical interconnect based on arrays of vertical-cavity lasers and detectors with monolithic microlenses." *Applied Optics*, Vol. 37, 1998, pp. 2811-2821.

[15] M. H. Ayliffe, D. R. Rolston, A. E. L. Chuah, E. Bernier, F. S. J. Michael, D. Kabal, A. G. Kirk, and D. V. Plant, "Design and Testing of a Kinematic Package Supporting a 32x32 Array of GaAs MQW Modulators Flip-Chip Bonded to a CMOS Chip." *Journal of Lightwave Technology*, Vol. 19, 2001, pp. 1543-1559.

[16] B. Robertson, Y. Liu, G. C. Boisset, M. R. Tagizadeh, and D. V. Plant, "In-situ interferometric alignment system for the assembly of microchannel relay systems." *Applied Optics*, Vol. 36, 1997, pp. 9253-9260.

[17] A. Tuantranont, V. M. Bright, J. Zhang, W. Zhang, J. Neff, and Y. C. Lee, "MEMS-Controllable Microlens Array for Beam Steering and Precision Alignment in Optical Interconnect System," *Proceedings of the 2000 Solid-State Sensor and Actuator Workshop*, Hilton Head Island, SC, pp. 101-104, June 4-8, 2000.

[18] J. E. Lin, F. S. J. Michael, and A. G. Kirk, "Design and characterization of two-axis rotational micro-mirrors using multi-user microelectromechanical system processes." *Journal of Microlithography, Microfabrication, and Microsystems*, Vol. 1, 2002, pp. 70-78.

[19] J. E. Lin, "Design and Characterization of MEMS Micromirror Devices." Master of Engineering Thesis, 2001, pp. 75.

[20] D. A. Koester, R. Mahadevan, B. Hardy, and K. W. Markus, "MUMPs Design Handbook." Revision 7.0, Cronos Integrated Microsystems, 3026 Cornwallis Rd., Research Triangle Park, NC 27709, 2001.

[21] L. Fan and M. C. Wu, "Two-dimensional optical scanner with large angular rotation realized by self-assembled micro-elevator." *1998 IEEE/LEOS Summer Topical Meetings on Broadband Optical Networks and Technologies: An Emerging Reality/Optical MEMS/Smart Pixels/Organic Optics and Optoelectronics*, 1998, pp II/106-II/108

[22] "Introduction to Gaussian Optics." *The Practical Application of Light – Melles Griot*, 1999, sec 2.2.

[23] H. Anton, *Calculus: 4th Edition*. John Wiley & Sons, Inc., 1992, pp.496-497.

[24] E. Hecht, *Optics: 3rd Edition.* Addison Wesley, 1998, pp. 185.

[25] W.C. Sweatt, "Describing holographic optical elements as lenses", JOSA, Vol. 67, 1977, pp. 803-808.

[26] "BPR – Diffraction-Based Beam Propagation", Code V Reference Manual, Version 9.2, pp. 5-199.

[27] V. Sharma, "Enhanced Vertical Scanning Interferometry", Honours Thesis I, McGill University, 2001.

[28] V. Sharma, "Enhanced Vertical Scanning Interferometry", Honours Thesis II, McGill University, 2002.